LAGRANGIAN ACCELERATION MEASUREMENTS IN TURBULENCE AT LARGE REYNOLDS NUMBERS

A Dissertation

Presented to the Faculty of the Graduate School

of Cornell University

in Partial Fulfillment of the Requirements for the Degree of

Doctor of Philosophy

by

Greg Anthony Voth

August 2000

LAGRANGIAN ACCELERATION MEASUREMENTS IN TURBULENCE AT LARGE REYNOLDS NUMBERS

Greg Anthony Voth, Ph.D.

Cornell University 2000

This thesis reports measurements of fluid particle acceleration in a large Reynolds number turbulent flow. The method for acceleration measurement is direct optical imaging of the positions of tracer particles and extraction of their accelerations from the position as a function of time. In order to meet the stringent imaging requirements for such measurements, we have implemented an ultra high speed imaging system based on silicon strip detectors. These detectors have been designed and optimized for vertex detectors in high energy physics collider experiments. With this system we are able to measure two coordinates of tracer particle positions with a dynamic range of better than 5000:1 and a frame rate of 70,000 frames per second.

Acceleration measurements are performed in a flow between counter-rotating disks from $R_\lambda = 140$ to $R_\lambda = 970$. The normalized acceleration variance is found to increase with Reynolds number at the lower Reynolds numbers and becomes nearly constant at the higher Reynolds numbers. This plateau is consistent with the Kolmogorov (1941) prediction. Different acceleration components are found to have about 15% different variance even at the highest Reynolds number. The acceleration probability distribution is found to have strong stretched exponential tails and flatness greater than 50.

An analysis of various sources of sample bias and other systematic errors is performed. Measurements of the acceleration variance as a function of the tracer particle size and fluid density demonstrate that the small tracer particles are acting as fluid particles to within the accuracy of the measurements. Measurements of the acceleration of larger particles provides direct measurement of the the forces on particles when they are large enough that they are averaging over the small scale structure of the turbulence.

Biographical Sketch

Greg Anthony Voth was born on February 9, 1972 in Mountain Lake, Minnesota to John and Carolyn Voth. With three brothers and one sister, the Voth household was always full of life. They lived 9 years in Minnesota before moving to Meno, Oklahoma. He attended high school at Oklahoma Bible Academy in Enid, Oklahoma. After undergraduate study in physics at Wheaton College in Illinois, he moved to Ithaca to begin graduate study at Cornell in the fall of 1994. The highlights of six years in graduate school were June 14, 1996 when Ellen Gilson accepted his proposal of marriage, and June 14, 1997 when they were married. Upon finishing, he will be moving to a post-doctoral position at Haverford College.

Soli Deo Gloria

Acknowledgements

I gratefully acknowledge the support of many who have made the completion of this thesis possible. First, I would like to thank Eberhard Bodenschatz, my thesis advisor. His enthusiasm and wide-ranging insights have been a great encouragement and support. The combination of direction and freedom that he has given me has provided an excellent training in how to do scientific research. I am also grateful for his investment in sending me to many conferences which has allowed me to develop contacts and learn to identify the important issues in the field.

Many thanks also to Jim Alexander, whose role has sometimes been that of a co-advisor. His commitment to this project has been absolutely essential to its success. Thanks for guidance through the delicate maze of detector fabrication and for many ideas for the data analysis. I am grateful to Zellman Warhaft for discussions during which I have learned some of the wisdom that has been gained during many years of experimental turbulence research. Thanks also to Eric Siggia for fruitful discussions, particularly for insightful comments and patience in the early years when I was working in turbulence research and taking my first fluid dynamics classes at the same time.

It has been a pleasure to work alongside Arthur La Porta for a large part of this research project. It is hard to imagine how all of the the data acquisition system and software would have been developed without him. Most of the results in this thesis have come from our combined efforts. I am particularly grateful for the insight from experience that he has brought to uncounted problems, and for his friendship. Thanks to Curt Ward for all his help in designing and building the strip detector readout system. Pablo Hopman has also provided extensive help and answers to questions in the process of fabricating the detectors. Thanks to Alice Crawford for her contributions to the project over the last year, particularly for her work last October and November helping a desperate graduate student replace our only fully functional detector which had died. I also thank K. Satyanarayan for the reliable flow between counter-rotating disks which he built.

I have benefited greatly from discussions with many other scientists in the field: Bob Ecke, Uriel Frish, Stephen Hall, Sidney Leibovich, John L. Lumley, Victor L'vov, Jacob Mann, Richard Miles, Laurent Mydlarski, Alain Pumir, Boris Shraiman, Katepalli Sreenivasan, Patrick Tabeling, and Prakash Vedula. Stephen Pope deserves special thanks for first showing me the importance of the Lagrangian perspective and for answers to so many questions along the way. I also thank P. K. Yeung for many discussions comparing DNS and experiment and for allowing us to use some of his data for analysis of systematic errors in the experiments.

Thanks to the other members of the Bodenschatz group with whom I have had the opportunity to work: Brendan Plapp, Rolf Ragnarsson, David Egolf, Ilarian Melnikov, Kwame Delandro, Brian Utter, Jon Karcz, Karen Daniels, Frederic Moisy, Will Bertsche, Jeff Fox, and Thomas Bourdel.

Friends in Grad Life Bible Studies have been a wonderful communtity encouraging spiritual growth and fun over the last six years. I will not even try to name all the special people. Thanks to my housemates at 303 Wyckoff: Ard Louis, Jarvis Sulcer, Keithanne Mochaitis, and Paul Pyenta.

Finally I thank my family for their unconditional support. Most of all I thank my wife, Ellen, whose love is a source of such great joy.

This research was financially supported by a Cottrell Scholar Award of Research Corporation and NSF Grant No. Phy 9722128. I gratefully acknowledge the NSF graduate fellowship program for support during my first three years of graduate study.

Table of Contents

List of Tables

List of Figures

Chapter 1

Introduction

The “problem of turbulence” can be stated so simply that it seems that there must be a simple and elegant solution. The dynamics of an incompressible Newtonian fluid are described by the Navier-Stokes equations

$$\frac{\partial \mathbf{u}}{\partial t} + \mathbf{u} \cdot \nabla \mathbf{u} = -\frac{1}{\rho} \nabla P + \nu \nabla^2 \mathbf{u} \tag{1.1}$$

$$\nabla \cdot \mathbf{u} = 0, \tag{1.2}$$

where $\mathbf{u}$ is the velocity field, P is the pressure field, ρ is the fluid density, and ν is the kinematic viscosity. The problem is to fully describe the velocity and pressure fields given the fluid density, viscosity and the boundary conditions. The boundary conditions require zero velocity at all solid walls and usually include a method of forcing the flow.

The problem has been given scientific study for over a century, and no solution has been found because the nonlinearity in the equations leads to instability and extremely complex spatio-temporal dynamics. This can be clarified by non-dimensionalizing the Navier-Stokes equations by typical length (L) and velocity (U) scales:

$$\frac{\partial \mathbf{u}}{\partial t} + \mathbf{u} \cdot \nabla \mathbf{u} = -\frac{1}{\rho} \nabla P + \frac{1}{Re} \nabla^2 \mathbf{u} \tag{1.3}$$

$$\nabla \cdot \mathbf{u} = 0, \tag{1.4}$$

where all variables are non-dimensional and $Re \equiv \frac{UL}{\nu}$ is the Reynolds number. At large Reynolds number, the viscous damping term is small relative to the non-linear terms and the flow is turbulent.

There is wide variety and deep complexity in the characteristics of flows as the Reynolds number is raised beyond the transition to turbulence, and one might give up on finding a solution to the problem. Many of the symmetries that make the Navier-Stokes equations simple to write down are spontaneously broken and simple descriptions become impossible. But there is still hope of a simple and elegant solution. This is because, as the Reynolds number becomes large enough, some of the symmetries originally satisfied by the Navier-Stokes equations are restored in a statistical sense. Even some of the symmetries that were originally broken by the boundary conditions are partially restored.

Fundamental turbulence research has long been guided by the goal of developing a statistical description of turbulence that can be applied to a broad class of flows and at all large Reynolds numbers. Tantalizing progress toward this goal has been made, particularly through the ideas of A. N. Kolmogorov, but a comprehensive theory remains elusive.

A powerful incentive for seeking a fundamental understanding of turbulence has come from the fact that the most common fluids on earth, water and air, are accurately described by the incompressible Navier-Stokes equations in most situations. As a result, there are many engineering and environmental applications that require an understanding of turbulence. Work in the field has been further motivated by the fact that as practical experience and scientific study have led to insights into the nature of turbulent flow, it has become a model problem for how to scientifically deal with highly nonlinear systems where a large range of length and time scales are excited simultaneously.

Instead of a single solution to turbulence, over the last century there have arisen a multitude of perspectives from which we can say something useful about turbulence. Certain quantities have been measured very accurately in experiments. Numerical simulations have revealed the details of low to moderate Reynolds number flows. Various modeling approaches have allowed accurate calculations of certain classes of flows. Atmospheric scientists have developed models that give useful predictions about atmospheric dispersion. Aerospace engineers have learned to predict turbulent drag on transportation vehicles. Chemical engineers have learned to understand many characteristics of turbulent mixers. And the list could be continued.

This thesis is about some new insights into the phenomenon of turbulence that have been made possible by the development of experimental techniques for high resolution particle tracking. There are a large number of fundamental and practical issues about turbulence that can be best studied from the perspective of the motion of individual fluid particles, called the Lagrangian perspective. On the fundamental side, most attempts to describe the scaling of the temporal evolution of a turbulent flow make use of a Lagrangian perspective. Traditional measurement approaches which probe a fixed spatial point as a function of time can not probe temporal scaling because the time evolution is dominated by sweeping of small structures past the probe by large structures. If we wish to study universal properties of the temporal evolution of a turbulent flow field, we must use a frame of reference following individual fluid particles (Tennekes, 1975; L'vov et al, 1997). A host of practical applications of an understanding of the Lagrangian properties of turbulence follow from the fact that turbulent transport is an essentially Lagrangian phenomenon. Thus models that attempt to accurately deal with mixing are often written in a Lagrangian framework. Lagrangian stochastic models are widely used for problems ranging from atmospheric pollution transport to turbulent reactive flows (Weil et al, 1992; Pope, 1985, 1994). High Reynolds number data is needed to determine model constants and check the accuracy of the models.

The importance of the Lagrangian perspective has long been recognized in the turbulence community. In fact, some of the first scientific studies of turbulence by Taylor (1921) and Richardson (1926) were focused on particle dispersion by turbulence. The reason that we know relatively little from this perspective is that the tools have not been available to obtain high Reynolds number Lagrangian data.

A few years ago at Cornell, we recognized a new experimental approach based on the silicon strip detectors commonly used in high energy physics experiments that allows particle tracking in turbulence at Reynolds numbers much larger than had been possible before. The system that has been developed is capable of imaging particles at 70,000 frames per second with very high light sensitivity and positioning dynamic range of better than 5000 to 1.

This thesis reports the first measurements with this system, which have focused on the Lagrangian acceleration distribution in turbulence. Measurements are made of trajectories of tracer particles in a water flow between counter-rotating disks with R_λ up to 1000. We find that the acceleration probability distribution has strong stretched exponential tails reflecting the intermittency of the acceleration. The flatness of the acceleration is found to be greater than other small scale quantities. Measurements of the normalized acceleration variance show an increase with Reynolds number up to about $R_\lambda = 400$ and nearly constant at higher Reynolds number. The variance of different acceleration components is found to be different by about 15% even at the highest Reynolds numbers, raising some interesting questions about the local isotropy of the flow. A study of the acceleration of different size tracer particles offers a new perspective on the motion of finite size particles in turbulence.

In many ways, experimental Lagrangian research is still in its infancy. Detection systems and flows amenable to high Reynolds number particle tracking are just beginning to be uncovered. There are a tremendous number of quantities that need to be studied. There are intricate issues of measurement accuracy and sample bias that must be wrestled with. As a result, this thesis is far from a complete story. The current data already points to some important results, but I see the deeper significance of this work in its place in the opening of a new perspective. In the coming years we may solidly established a Lagrangian phenomonolgy that describes the temporal evolution of turbulence in the same way that current phenomenology describes its spatial structure. My hope is that this research is seen as a demonstration that some of the measurements necessary to develop these ideas are already possible.

Chapter 2

Background to Turbulence

This chapter is an attempt to cover the main background material which has guided our work. Theoretical approaches will be discussed first followed by experimental and computational work with an emphasis placed on the Lagrangian perspective. I can not begin to do justice to all that has been done in the field, both because of the vast amount of work that has been done, and because we do not yet have a solid theoretical framework with which to unite our phenomenological insights. There are a wide variety of sources for a more complete presentation of what is known about turbulence. The standard reference book is Monin and Yaglom's *Statistical Fluid Mechanics,* particularly volume 2, "Mechanics of Turbulence." Other books that I have used extensively include *A First Course in Turbulence* by Tennekes and Lumley, *Turbulent Flows* by Pope, and *Turbulence* by Frisch. There are also a plethora of review articles. Recent ones include Warhaft (2000), Nelkin (2000), Sreenivasan (1999), Sreenivasan & Antonia (1997), and Nelkin (1994).

2.1 Kolmogorov's 1941 Theory

The underlying idea that affects almost all we know about turbulence is the cascade process. When a fluid is stirred and the Reynolds number is large, the flow structures which are created are unstable. They break up into smaller structures which are also unstable, and the process continues until the structures become small enough that viscosity turns their energy into heat. The concept of a cascade is credited to Richardson (1922), and the concept was formalized into a useful theory by A. N. Kolmogorov in 1941. A broad range of results that were obtained in roughly this time period using the approach that Kolmogorov pioneered are commonly labeled together as the Kolmogorov (1941) theory or K41 for short. I will present the familiar Eulerian Kolmogorov predictions first in order to provide a connection to the almost exactly analogous quantities in the Lagrangian perspective. There will be many details about precisely what is assumed and what the shortcomings are for which I refer the reader to the references in the previous paragraph. My goal is to give an overview of how the Kolmogorov theory has directed out thinking about the Lagrangian perspective.

An important step in formalizing the cascade idea is to recognize that since energy is conserved, the average energy input due to stirring will be equal to the average energy dissipated to heat by viscosity if the system is in a statistically steady state. The rate of energy input per unit mass is $\epsilon = u^3/L$ where u is the rms velocity and L is a length scale characterizing the stirring. The rate of energy dissipated per unit mass is

$$\epsilon = 2\nu \left\langle s_{ij} s_{ij} \right\rangle \tag{2.1}$$

where

$$s_{ij} = \frac{1}{2}\left(\frac{\partial u_i}{\partial x_j} + \frac{\partial u_j}{\partial x_i}\right) \tag{2.2}$$

is the rate of strain tensor. In a cascade, the energy input and dissipation happen at very different length scales; so a theory can be developed that relies on a separation of driving and dissipation length scales with scales in between only passing the energy along.

Kolmogorov 1941 theory is based on three hypotheses, all of which assume sufficiently large Reynolds numbers (Kolmogorov, 1941b).

- Hypothesis of Local Isotropy: Small scale motions in turbulence are statistically isotropic.
- First Similarity Hypothesis: Statistics of small scale motions have a universal form determined only by the average energy dissipation and the viscosity.
- Second Similarity Hypothesis: Statistics of intermediate scale motions have a universal form determined only by the viscosity.

2.1.1 Eulerian Kolmogorov predictions

Inertial Range

Consider the instantaneous velocity difference between two points in a turbulent flow separated by a distance r,

$$\Delta_r u_i = u_i(\vec{x} + r\hat{e}_i) - u_i(\vec{x}) \tag{2.3}$$

where only the longitudinal component is considered for simplicity. Local isotropy and the first similarity hypothesis imply that for $r << L$

$$\left\langle \Delta_r u_i \Delta_r u_j \right\rangle = (\epsilon\nu)^{1/2} \beta_E \left(r/\eta\right) \delta_{ij} \tag{2.4}$$

where $\eta = (\nu^3/\epsilon)$ and $\beta_E\left(r/\eta\right)$ is a universal function. If we further restrict attention to the intermediate or inertial range of scales, then this second order structure function must also be independent of viscosity and we have the prediction

$$\left\langle \Delta_r u_i \Delta_r u_j \right\rangle = C_2 (\epsilon r)^{2/3} \delta_{ij} \tag{2.5}$$

where C_2 is a universal constant. The same reasoning applied to arbitrary order moments of $\Delta_r u_i$, yields the prediction

$$\langle(\Delta_r u_i)^p\rangle \sim (\epsilon r)^{p/3}. \tag{2.6}$$

for r in the inertial range.

In addition to these predictions, Kolmogorov derived an exact relation for the third order structure function from the Navier-Stokes equations (Kolmogorov, 1941a). This is

$$\langle\Delta_r u_i^3\rangle = \frac{4}{5}\epsilon r, \tag{2.7}$$

when r is in the inertial range.

Dissipation Range

Kolmogorov's hypotheses also imply that the velocity gradient distribution should only depend on the average energy dissipation and the viscosity. The symmetric second order moment has already been used to define the energy dissipation in Eq. 2.1. The anti-symmetric second order moment is related to the squared vorticity, or enstrophy

$$\omega^2 = 4\Omega_{ij}\Omega_{ij} = (\nabla \times \mathbf{u}) \cdot (\nabla \times \mathbf{u}), \tag{2.8}$$

where

$$\Omega_{ij} = \frac{1}{2}\left(\frac{\partial u_i}{\partial x_j} - \frac{\partial u_j}{\partial x_i}\right). \tag{2.9}$$

The relation between the enstrophy and the average dissipation simply using their definitions is

$$\frac{\epsilon}{\nu} = \left\langle\omega^2\right\rangle + 2\left\langle\frac{\partial^2 u_i u_j}{\partial x_i \partial x_j}.\right\rangle \tag{2.10}$$

The term on the right is small (zero if the flow is homogeneous), and we find

$$\langle\epsilon\rangle = \nu\langle\omega^2\rangle. \tag{2.11}$$

So we see that the K41 theory is not needed to make predictions about the second order moments of the velocity gradients. K41 does make non-trivial predictions about the higher moments of the velocity gradient distribution. Since they all can depend only on ϵ and ν, the normalized moments should be universal constants:

$$\frac{\left\langle\left(\frac{\partial u_1}{\partial x_1}\right)^p\right\rangle}{\left\langle\left(\frac{\partial u_1}{\partial x_1}\right)^2\right\rangle^{p/2}} = M_p. \tag{2.12}$$

2.1.2 Lagrangian Kolmogorov predictions

Kolmogorov's hypotheses can also be used to make predictions for the temporal evolution of Lagrangian trajectories. This is less widely known partly as a result of an error in the original paper (Kolmogorov, 1941b), and partly because the predictions have been much more difficult to test with experiments. Kolmogorov originally proposed that his hypotheses be applied to the full four dimensional space time velocity difference distribution. The extension to Eulerian temporal velocity differences is an error (Tennekes, 1975). Since the largest scale motions sweep the small scale structure past a point in the flow, the temporal variations in the velocity at a point are dominated by the (non-universal) large scale motions even for the very fast time scales. The solution to this is to look instead at the temporal evolution of the flow along Lagrangian trajectories.

Inertial Range

Following the notation of Monin & Yaglom (1975) the second order Lagrangian velocity structure function is defined as

$$D_{ij}^{L(2)}(\tau) = \langle (u_i(t+\tau) - u_i(t))(u_j(t+\tau) - u_j(t)) \rangle, \tag{2.13}$$

where u_i and u_j are components of the velocity vector of a fluid particle and τ is a time difference. If the flow is statistically stationary and $\tau \ll T_L$, where T_L is the Lagrangian velocity correlation time scale, Kolmogorov's hypotheses predict that at sufficiently high Reynolds number

$$D_{ij}^{L(2)}(\tau) = (\epsilon\nu)^{1/2} \beta_L\left(\tau/\tau_\eta\right)\delta_{ij}, \tag{2.14}$$

where ϵ is the mean energy dissipation per unit mass, ν is the kinematic viscosity, $\tau_\eta \equiv (\nu/\epsilon)^{1/2}$ is the Kolmogorov time scale, and $\beta_L(\tau/\tau_\eta)$ is a universal function. Furthermore, in the inertial time range where $\tau \gg \tau_\eta$, this result must be independent of ν and one obtains

$$D_{ij}^{L(2)}(\tau) = C_0 \epsilon \tau \delta_{ij}, \tag{2.15}$$

where C_0 is a universal constant. Similarly, for the higher order structure functions in the inertial time range

$$D^{L(p)}(\tau) \sim (\epsilon\tau)^{p/2}. \tag{2.16}$$

(For odd orders, $D^{L(p)}$ is zero by symmetry unless the absolute value of the velocity difference is used.)

Dissipation Range

Predictions for the moments of the fluid particle acceleration probability density function (PDF) can be obtained by assuming that $u_i(t)$ is differentiable and taking the limit $\tau \to 0$ of the Lagrangian velocity structure functions. In particular, the second order structure function scales as τ^2 for small τ yielding the prediction for the acceleration variance

$$\langle a_i a_j \rangle = a_0 \epsilon^{3/2} \nu^{-1/2} \delta_{ij}, \tag{2.17}$$

where a_0 is another universal constant. The analysis that led to Eq. 2.17 can also be extended to the higher moments of the acceleration distribution, and it is found that Kolmogorov's 1941 hypotheses predict that the normalized acceleration moments should be constants

$$\frac{\langle a^p \rangle}{\langle a^2 \rangle^{p/2}} = a_p. \tag{2.18}$$

Note that the acceleration variance is the Lagrangian counterpart to the mean dissipation and enstrophy in the Eulerian perspective. Equation 2.17 can be viewed as predicting that the Lagrangian quantity, $\nu^{1/2} \langle a_i a_i \rangle$, is similar to the mean dissipation. It is characteristic of the small scales yet its magnitude is determined by the large scales, and hence it is independent of viscosity. We do not have any exact relations like Eq. 2.11 relating the acceleration to the energy dissipation, so the relation between acceleration and energy dissipation must be explored by experiment and simulations. Elucidating this relationship is one of the primary goals of this thesis.

2.2 Pressure Gradients

Fluid particle accelerations in turbulence are dominated by the pressure gradient. Batchelor (1951) estimates that the viscous contribution is 2% of the pressure gradient contribution to the acceleration variance. Numerical simulations by Vedula & Yeung (1999) find that at $R_\lambda = 235$ the viscous contribution to the acceleration variance is 1.6% of the pressure contribution. This means that the ratio of viscous force to pressure gradient force is 13%.

The pressure structure function, $\langle (\Delta_r p)^2 \rangle$ can be calculated from the fourth order velocity structure functions. Hill & Wilczak (1995) provide a general derivation of this relation which was originally derived using a joint gaussian approximation for the fourth order velocity structure functions (Obukhov, 1949; Batchelor, 1951). In the limit of small r, the pressure structure function contains the pressure gradient variance. Following the notation of Nelkin & Chen (1999), the Hill and Wilczak relation implies that the pressure gradient variance can be written

$$\left\langle \left(\frac{\nabla p}{\rho} \right)^2 \right\rangle = 4 \int_0^\infty r^{-3} \left(L(r) + T(r) - 6M(r) \right) dr, \tag{2.19}$$

where the independent fourth order velocity structure functions are longitudinal, $L(r) = \langle \Delta u^4(r) \rangle$; transverse, $T(r) = \langle \Delta v^4(r) \rangle$; and mixed, $M(r) = \langle \Delta u^2(r) \Delta v^2(r) \rangle$. Here Δu is the longitudinal velocity difference and Δv is the transverse.

The quasi-gaussian approximation used by Obukhov (1949) and Batchelor (1951) assumes that the fourth order velocity structure functions are related to the second order as they are for a joint gaussian distribution.

$$\begin{aligned} L(r) &= 3[D_{LL}(r)]^2 && (2.20) \\ T(r) &= 3[D_{NN}(r)]^2 && (2.21) \\ M(r) &= D_{LL}(r) D_{NN}(r) && (2.22) \end{aligned}$$

where D_{LL} and D_{NN} are the longitudinal and transverse second order structure functions. Using an interpolation formula for the longitudinal structure function, Nelkin & Chen (1999) obtain a value for a_0 in Eq. 2.17 of 1.16. (a_0 is 1/3 of β^{QG} that Nelkin & Chen (1999) report since they use the sum over all three coordinates.) Kaneda (1993) reviews some earlier results for the value or a_0 using similar approaches. The results from numerical simulations by Vedula & Yeung (1999) and Gotoh & Rogallo (1999) are much larger than this quasi-gaussian value. They find $a_0 = 3.4$ at $R_\lambda = 235$ and growing as $R_\lambda^{1/2}$. Nelkin & Chen (1999) interpret this as a combination of a low Reynolds number effect and an intermittency effect. The quasi-gaussian value of a_0 calculated from the second order structure functions of the numerical simulation data is growing with Reynolds number because the simulations have a limited scaling range. It has just reached the high Reynolds number limit at $R_\lambda = 235$. This is the low Reynolds number effect. The discrepancy of the actual value of a_0 with the quasi-gaussian approximation is called the intermittency correction. This is found to be growing at approximately ${R_\lambda}^{0.23}$.

Hill & Wilczak (1995) derive several expressions for the pressure gradient variance from Eq. 2.19. These generally require precision measurements of the inertial and dissipation range form of the fourth order velocity structure functions. I have not seen high Reynolds number measurements used to determine the Reynolds scaling of a_0 from these directly. An approximation by Hill & Wilczak (1995) suggests the high Reynolds scaling of $a_0 \sim R_\lambda^{0.22}$.

2.3 Refined Similarity Hypotheses

Soon after Kolmogorov proposed his 1941 hypotheses, it was observed that the K41 theory could not be exactly right. It treats the average energy dissipation as the only relevant quantity, but it is the fluctuating energy dissipation that is more relevant to the local turbulence. Kolmogorov (1962) proposed that the K41 similarity theory could be refined by assuming that the statistics of $\Delta_r u$ depend on the value of the energy dissipation averaged over a sphere of radius r, which will be labeled ϵ_r, rather than on its global average, ϵ. For values of r in the inertial range this yields

$$\langle (\Delta_r u)^p \, | \epsilon_r \rangle = C_n \, (\epsilon_r r)^{p/3} \tag{2.23}$$

The structure functions are then obtained by averaging this over the distribution of ϵ_r. Kolmogorov (1962) assumed

$$\frac{\langle \epsilon_r^q \rangle}{\epsilon^q} \sim \left(\frac{L}{r} \right)^{\mu_q} . \tag{2.24}$$

where L is the integral length scale in the flow. Experiments generally support this assumption and find that the intermittency exponent is in the range $\mu_2 = 0.25 \pm 0.05$ (Sreenivasan & Kailasnath, 1993). Kolmogorov used a log-normal model to determine μ_q for other q, but many other models have been developed. Corrections to the K41 scaling can be found from the r dependence of the moments of ϵ_r. For more details on this subject, see Sreenivasan & Antonia (1997) and references therein.

It is possible to apply the refined theory to calculation of intermittency corrections to the acceleration variance. The replacement of Eq. 2.17 in the refined theory is

$$\langle a_i a_j \rangle = a_0 \nu^{-1/2} \delta_{ij} \left\langle \epsilon_r^{3/2} \right\rangle \tag{2.25}$$

Using equation 2.24 with $r = \eta$, $q = 3/2$, and the log-normal result $\mu_q = \frac{1}{2} q(q-1)\mu_2$, it is found that

$$\langle a_i a_j \rangle = a_0 \nu^{-1/2} \delta_{ij} \epsilon^{3/2} \left(\frac{L}{\eta} \right)^{3\mu_2/8} . \tag{2.26}$$

Since $L/\eta \sim R_\lambda^{3/2}$, this implies that

$$\langle a_i a_j \rangle \sim a_0 \epsilon^{3/2} \nu^{-1/2} \delta_{ij} R_\lambda^{9\mu_2/16} \sim R_\lambda^{0.14}. \tag{2.27}$$

A similar calculation can be made for the acceleration flatness. Applying the refined theory to the fourth moment gives

$$\langle a^4 \rangle \sim \left(\frac{L}{\eta} \right)^{3\mu_2} \tag{2.28}$$

Again using the lognormal model, the prediction of the flatness scaling is

$$\frac{\langle a^4 \rangle}{\langle a^2 \rangle^2} \sim \left(\frac{L}{\eta} \right)^{3\mu_2 - 3\mu_2/4} \sim R_\lambda^{27\mu_2/8} \sim R_\lambda^{0.84}. \tag{2.29}$$

This can be compared to the scaling of the velocity gradient flatness which is found experimentally to agree with the log-normal prediction,

$$F_{\frac{\partial u}{\partial x}} \sim R_\lambda^{3\mu_2/2} \sim R_\lambda^{0.38}. \tag{2.30}$$

There have, of course, been many other intermittency models which improve on the log-normal model of the energy dissipation. The measurements of the acceleration distribution is not currently of high enough quality to distinguish between intermittency models.

The goal here is to point out that the intermittency models can make predictions of the Reynolds number scaling of the acceleration distribution, and that it is expected to be more intermittent than the velocity gradients.

Borgas (1993) has used a related approach to calculate intermittency corrections to the acceleration variance. Instead of using the energy dissipation averaged over a sphere of radius r as the conditional variable, he uses the energy dissipation averaged over a time t, along a Lagrangian trajectory, which will be designated ϵ_t. He then uses the multifractal p-model (Meneveau & Sreenivasan, 1987) to determine the scaling of the moments of ϵ_t, and obtains

$$\langle a_i a_j \rangle \sim a_0 \epsilon^{3/2} \nu^{-1/2} \delta_{ij} R_\lambda^{0.13} \tag{2.31}$$

The predictions in equations 2.27 and 2.31 are identical for all practical purposes. Both of these calculations use the assumption that the appropriate quantities to use in determining scaling of small scale statistics are the standard Kolmogorov scales. In reality, the small scale cutoff is fluctuating in an intermittent cascade (Nelkin, 1990) and so these are only first order approximations.

I believe that Borgas has an important insight. Traditional work on intermittency has focused heavily on the instantaneous spatial intermittency of the velocity and energy dissipation. However, we expect that a turbulent cascade is both spatially and temporally intermittent. The study of temporal intermittency requires Lagrangian measurements in order to avoid sweeping effects. One way to develop a temporal phenomenology is to analyze the energy dissipation averaged over a time t along Lagrangian trajectories as Borgas has suggested. Temporal intermittency of other quantities such as the enstrophy and the scalar gradient could be analyzed in the same way. Spatial intermittency of both of these have have been found to be different from the dissipation and have been used for refined similarity hypotheses (Chen et al, 1997; Stolovitzky et al, 1995). Another possibility is to study the spatial and temporal intermittency of the squared acceleration.

2.4 Experiments

2.4.1 Eulerian Measurements

Most turbulence measurements have been made with hot film and hot wire anemometers. These measure the velocity of the fluid by measuring the heat transported away from a small heated film or wire. If the mean velocity is much larger than the fluctuating velocity, the time series of the velocity is equal to the velocity along a spatial cut through the flow at a single point in time. In this way, Eulerian spatial velocity differences can be measured with great accuracy.

The first tests of the Kolmogorov theory were measurements of the Eulerian inertial range predictions. The study by Grant et al (1962) using a hot film probe of turbulence in a tidal channel found several decades inertial range where the second order statistics were in excellent agreement with K41. A recent compilation (Sreenivasan, 1995) found over 50 measurements of Eulerian velocity structure functions measured with hot wire probes.

Hot wire measurements in the last two decades have made it clear that there are deviations from the Kolmogorov predictions for the inertial range scaling of the Eulerian velocity structure functions (Anselmet et al, 1984; Sreenivasan & Antonia, 1997). The structure functions are found to have inertial range power laws,

$$\langle (\Delta_r u_i)^p \rangle \sim (\epsilon r)^{\zeta_p}, \tag{2.32}$$

but for p greater than three, ζ_p is less than the K41 prediction of $p/3$. This deviation is a result of intermittency in the energy dissipation. K41 assumed that the energy dissipation is everywhere equal to its average. In reality it is a fluctuating quantity and experimentally it is found to have very large fluctuations at large Reynolds numbers (Meneveau & Sreenivasan, 1991).

Intermittency also causes deviations from the K41 predictions for the higher order moments of the velocity gradient distributions. Van Atta & Antonia (1980) find that the derivative flatness scales as $R_\lambda^{0.41}$, contradicting Eq. 2.12.

2.4.2 Lagrangian Measurements

Experimental Lagrangian measurements have been of three distinct types. The first measurements used the theory of turbulent dispersion by Taylor (1921) to determine the Lagrangian velocity correlation function from the scalar dispersion. Shlien & Corrsin (1974) provide a summary of measurements using this technique before themselves offering a set of measurements.

The second technique was optically tracking tracer particles that approximated Lagrangian motion. Snyder & Lumley (1971) made the first systematic set of particle tracking velocity measurements from wind tunnel grid turbulence. Sato & Yamamoto (1987) have reported similar measurements in water tunnel grid turbulence. Dracos (1996) describes a technique for stereoscopic imaging to record many particle tracks at once in three dimensions. A preliminary study using this technique in a turbulent boundary layer is reported in Virant & Dracos (1997). Mann et al (1999) have taken the technique developed by Dracos (1996) and have made extensive measurements in a flow between two oscillating grids up to $R_\lambda = 100$. Although some of the results are difficult to reconcile with the numerical simulations of Yeung (1994), this work contains some important steps toward reliable three-dimensional particle tracking. Each of these studies has been helpful in illuminating the large scale Lagrangian properties of turbulence. All of these measurements were for $R_\lambda < 250$, and none have observed an inertial range scaling of the Lagrangian velocity structure function. Spatial and temporal measurement resolution precluded precise acceleration measurements.

The third technique has been to use the relations between the fourth order velocity structure functions and pressure structure functions described in section 2.2 to calculate pressure gradient statistics from hot wire velocity measurements. This allows measurement of particle accelerations since the acceleration of fluid particles is dominated by the pressure gradient contribution for all but the smallest Reynolds numbers. Hill & Thoroddsen (1997) have used this technique to study spatial acceleration correlations at

$R_\lambda = 208$. Spatial resolution limitations kept them from reporting one point acceleration statistics.

The only available high Reynolds number data came from balloon tracking in the atmospheric boundary layer (Hanna, 1981). This data roughly supports the linear scaling of the Lagrangian velocity structure function in the inertial range (Eq. 2.15) and the value of C_0 is 4.0 ± 2.0. Unfortunately, the small sample size and variable flow conditions limited the conclusions that could be drawn.

Most of what we have learned about small scale Lagrangian properties of turbulence has come from direct numerical simulations (DNS). DNS has provided unparalleled accuracy for $R_\lambda < 250$, and this upper limit is slowly increasing as computers become more powerful. The fast (R_λ^6) increase in computational cost with Reynolds number means that the Reynolds numbers attainable in simulations will likely remain modest for many years. The combination of the precision and well controlled flows available from simulations with the high Reynolds number and complex flow conditions available from experiments will likely continue to be essential.

Yeung & Pope (1989) provided a comprehensive numerical study of Lagrangian statistics in artificially forced isotropic homogeneous turbulence. Squires & Eaton (1991) calculated Lagrangian statistics of homogeneous shear flows. Yeung (1994, 1997) studied two particle Lagrangian statistics in isotropic simulations and Vedula & Yeung (1999) have extended the one-particle results to $R_\lambda = 235$. Gotoh & Rogallo (1999) have conducted homogeneous isotropic simulations up to $R_\lambda = 172$ and report small scale pressure statistics. There is a wealth of information that has been extracted from these simulations, but I will only highlight three points. First, no inertial range is observed in the Lagrangian velocity structure functions. This suggests that Lagrangian statistics, like pressure statistics, require much higher Reynolds numbers before inertial range scaling is observed. Second, the acceleration variance is not scaling as predicted in Eq. 2.17 for $R_\lambda < 235$. Instead it is found that rather than being constant, a_0 scales as $R_\lambda^{1/2}$ across this range of Reynolds numbers. Third, the acceleration flatness is 39 at $R_\lambda = 235$, which is much larger than other small scale statistics.

In section 2.1.2 the fluid particle acceleration was discussed as a small scale quantity analogous to the velocity gradients. There are some major differences in their statistical properties though. An important difference is in the flatness of their probability distributions. The longitudinal velocity derivative, which has recieved the most careful study using hot wire anemometry, has a flatness of 6.0 at $R_\lambda = 200$ (Van Atta & Antonia, 1980). The transverse velocity derivative flatness is 8.5 at this Reynolds number (Chen et al, 1997). The passive scalar gradient, another small scale quantity, has a flatness of 17 at the same Reynolds number (Warhaft, 2000). The acceleration is more intermittent than any of the others, having a flatness of 34 at $R_\lambda = 200$ (Vedula & Yeung, 1999).

2.4.3 Anisotropy of high Reynolds number flows

An important avenue of current research concerns the effects of the largest scale motions on inertial and dissipation range quantities. Many studies reviewed in Sreenivasan (1991) and Warhaft (2000) find that passive scalar gradient statistics are not even approximately isotropic up to $R_\lambda = 1000$. Sreenivasan & Dhruva (1998) find that even at $R_\lambda = 20,000$ there are significant effects on inertial range scaling of velocities from large scale shear. Arad et al (1998) proposes a method of decomposing inertial range quantities using spherical tensors that allows separation of the isotropic sector from the anisotropy introduced at the large scales. Shen & Warhaft (2000) finds that in a homogeneous shear flow up to $R_\lambda = 1000$, statistics of the velocity gradient of order greater than three have anisotropy that is constant or growing with Reynolds number. These and other studies suggest that the idealized model of infinite Reynolds number is not sufficient to fully describe the small scale properties of turbulence at Reynolds numbers which exist on earth.

2.5 Motion of Spherical Particles in Turbulence

In order to understand the effect of finite size tracer particles in our measurements, we made some measurements of the acceleration variance as a function of particle size and fluid density. The results are presented in section 4.8. We find that the regime we are operating in is very far from the one that has been traditionally studied, and so there is little directly relevant background information to review. Nevertheless, I will briefly review some of the work that has been done in this area as a context for our measurments.

The problem of the motion of rigid spherical particles in a turbulent flow has been a topic of research for over 100 years. Basset (1888), Boussinesq (1903), and Oseen (1927) all considered the settling of a sphere due to gravity in a fluid at rest. Tchen (1947) developed an equation for a rigid sphere moving in an inhomogeneous flow. Corrsin & Lumley (1956) identified some errors and made improvements to Tchen's equation. (As I received my first formal introduction to turbulence in a class taught by John L. Lumley, I find it noteworthy that this was the problem on which he wrote his Ph.D. thesis under Stanley Corrsin).

The equation which is generally accepted today was obtained by Maxey & Riley (1983).

$$\begin{aligned} m_p \frac{d\mathbf{V}}{dt} = (m_p - m_f)\,\mathbf{g} + m_f \frac{D\mathbf{u}}{Dt} - \frac{1}{2} m_f \frac{d}{dt}\left(\mathbf{V} - \mathbf{u}(\mathbf{X}(t),t) - \frac{1}{10}a^2\nabla^2\mathbf{u}\right) \\ -6\pi a\mu\mathbf{Q}(t) - 6\pi a^2\mu \int_0^t d\tau \frac{d\mathbf{Q}/d\tau}{(\pi\nu(t-\tau))^{1/2}}, \end{aligned} \tag{2.33}$$

where $\mathbf{u}(x,t)$ is the undisturbed fluid velocity field, $\mathbf{V}(t)$ is the particle velocity, $\mathbf{X}$ is the position of the particle center, m_p is the mass of the sphere, m_f is the mass of the displaced fluid, a is the particle radius, $\mathbf{g}$ is the acceleration of gravity, μ is the viscosity, and

$$\mathbf{Q} = \mathbf{V} - \mathbf{u}(\mathbf{X}(t),t) - \frac{1}{6}a^2\nabla^2\mathbf{u}. \tag{2.34}$$

The terms in Eq. 2.33 are called gravitational, force from the undisturbed flow field, added mass, Stokes drag, and Basset history term.

This equation is valid for small particle Reynolds number, $Re_p = |\mathbf{u} - \mathbf{V}|a/\nu \ll 1$, small shear Reynolds number, $Re_s = a^2/\nu\tau_\eta \ll 1$, and for small particles so that, $a/\eta \ll 1$, where η and τ_η are the Kolmogorov length and times scales characterizing the smallest scales of the undisturbed flow. A different way of writing the shear Reynolds number condition is to require that the Stokes time $(\tau_s = a^2\rho_p/\nu\rho_f)$ be much less than the Kolmogorov time. Determining the effects of small deviations from the limits listed above (Mei et al, 1991), and finding methods of solution of Eq. 2.33 (Coimbra & Rangel, 1998) are still topics of current research interest.

We find that nearly neutrally buoyant tracer particles accurately reproduce the acceleration of the fluid even when the conditions on shear Reynolds number and pariticle size are far from satisfied. For example, the acceleration variance of $46\ \mu\mathrm{m}$ diameter polystyrene spheres in water is within 10% of the small particle limit even when $\eta = 18\ \mu\mathrm{m}$. In this case the Stokes time is $550\ \mu\mathrm{s}$ compared to a Kolmogorov time of $330\ \mu\mathrm{s}$. Prediction of the motion of particles of this size range requires a much more involved theory including the structure of the dissipation scales in the turbulent flow and the modification of the flow by the particles.

Chapter 3

Techniques for High Resolution Measurement of Particle Trajectories in Turbulence

The techniques that we use for particle tracking in intense turbulence are conceptually quite straight forward. We optically track tracer particles, using the same technique that the eye uses to measure wind velocities during a snow storm. The reason that these measurements have not been made previously is that there are several major technological barriers to high resolution particle tracking at large Reynolds numbers.

This chapter describes the experimental apparatus and protocols. During my graduate studies, we have built and made measurements with two generations of detection systems for particle tracking. The first system was based on a position sensitive photodiode. This is described briefly in section 3.1.2, with most of the details contained in Appendix A. The second generation system, which was used to acquire most of the data for this thesis, is based on silicon strip detectors. Sections 3.1.3 through 3.1.5 describe the silicon strip detectors, readout electronics, and data acquisition codes. Section 3.2 describes the components of the optical system. Section 3.3 describes the turbulent water flow between counter-rotating disks.

3.1 Detectors

3.1.1 Imaging frame rate requirements

The best available method for measuring particle trajectories in turbulence is optically measuring particle positions and determining velocities and accelerations from position versus time information. The primary barrier which has limited Lagrangian measurements using this technique is the difficulty of accurately measuring positions of tracer particles with sufficient time resolution. A simple calculation illustrates why this is the case.

We wish to generate intense turbulence (in our flow we reach $R_\lambda \approx 1000$) in a laboratory flow. The natural choice of fluid is water since it has a low viscosity ($1 \times 10^{-6} \quad \mathrm{m}^2/\mathrm{s}$)

and tracer particles are available near water's density. (It also is cheap, non-toxic and works well at room temperature.) The integral length scale is limited since the experiments must fit in a Cornell laboratory. In our flow we find $L = 7$ cm. From the relation

$$R_\lambda = \sqrt{15uL/\nu}, \tag{3.1}$$

it can be seen that this implies an rms velocity of 0.95 m/s. Now using $\epsilon = u^3/L$, the Kolmogorov scales of time and length are

$$\tau_\eta = 287 \quad \mu\mathrm{s} \tag{3.2}$$

$$\eta = 17 \quad \mu\mathrm{m}. \tag{3.3}$$

To fully resolve particle trajectories, the detector must capture motion which occurs on time scales at least as short as the Kolmogorov time. We find that we need more than 15 position measurements per characteristic time to resolve particle accelerations, and this implies that a frame rate of more than 50 kHz is required. A resolution of about 500 pixels is necessary to measure trajectories with sufficient spatial resolution.

Comparison of this requirement with current CCD detector systems leads to the conclusion that these measurements cannot be made. Standard CCD cameras operate at 30 Hz, and special high speed CCD imagers are available that run at up to a few thousand frames per second; but 50 kHz readout for thousands of sequential frames is not going to be available in the near future. [1]

3.1.2 Position sensitive photodiode

The first fluid particle acceleration measurements we made were with a position sensitive photodiode. The detector was part number DLS10 from United Detector Technologies. It is essentially a large square photodiode (1.0 cm on a side) which allows an analog two-dimensional measurement of the position of a single light spot. It works by measuring the fraction of the photo-current that migrates to the top vs. bottom of the front plane, and to the right vs. left of the back plane. The response time of this detector (500 kHz) is more than adequate. The measurements made with this system were published in *Physics of Fluids*, **10**:9, 1998, p. 2268–2280. This paper along with some reinterpretations of the data in it are contained in Appendix A. Although the low light sensitivity and relatively

---

[1] There have recently been several interesting approaches to high speed CCD imaging that might question this conclusion. One is the Princeton Scientific Instruments Ultra Fast Framing CCD Camera. This camera can read out images at up to 1 MHz, but is limited to 32 consecutive frames followed by seconds of readout time, so extended particle tracking is not feasible. People sometimes notice advertisements of cameras with "up to 40 kHz frame rate." For example, see the Kodak EKTAPRO HS Motion Analyzer Model 4540. This camera can read 256×256 images at up to 4500 frames per second, but reaches 40,500 frames per second only by reading out a small part of the frame. The one way around the huge amounts of data produced by high speed pixel imaging is to have parallel front end compression of the data. Someday we may have cameras that output only the positions of light spots rather than full images. This would allow pixel based cameras to reach the speeds necessary for Lagrangian measurements.

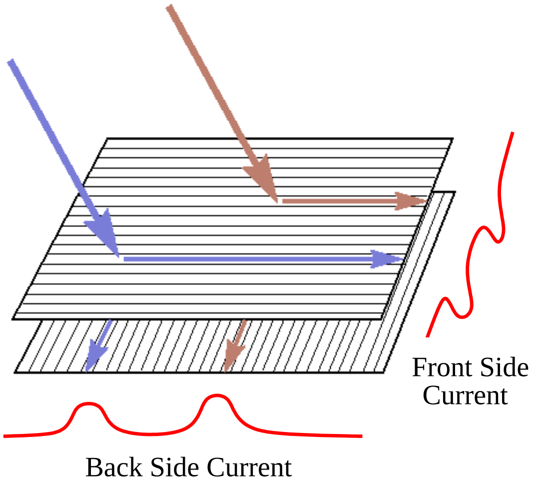

Figure 3.1: Diagram of charge collection in a double sided strip detector.

poor position measurement accuracy of this detector were major limitations, this first round of experiments provided insights that have been essential in guiding the design of the new particle tracking system.

3.1.3 Silicon strip detectors

A tremendous improvement in the light sensitivity and position measurement accuracy has been made possible by the new silicon strip detector imaging system. Strip detectors have been developed and optimized through many years of effort by the high energy physics community. The detectors we use were designed as charged particle detectors for the CLEO electron positron collider experiment here at Cornell (Fast et al, 1999). Strip detectors are essentially large (5.12 cm by 2.56 cm) planar photodiodes, made of 300 μm thick high resistivity n-doped silicon. The front, junction side is subdivided by p-type implants into 511 sense strips, allowing measurement of the one dimensional projection of the light striking the detector.

Strip detectors have a large speed advantage over a conventional CCD camera, since only $511 + 511$ strips must be read to localize the particle in 2D, compared with 511×511 pixels for a CCD camera of equivalent resolution. The current system can read out the detector at rates up to 70,000 frames per second.

The original plan was to use double sided strip detectors which allow the measurement of both a horizontal and vertical projection of the same image. These detectors have the ohmic (back) side of the detector also divided by p-type barriers into 511 n-type sense strips orthogonal to the front p-type strips. A simple diagram showing the geometry of charge collection in a double sided detector is in Fig. 3.1. When a charged particle or photon strikes the detector, electron-hole pairs are created. Holes are collected by the nearest p-type strip on the front side, and electrons are collected by the nearest n-type strip on the back side, and so the two coordinates of the position of the particle are measured.

When we tested detectors of this type, we found that the signal read from the back

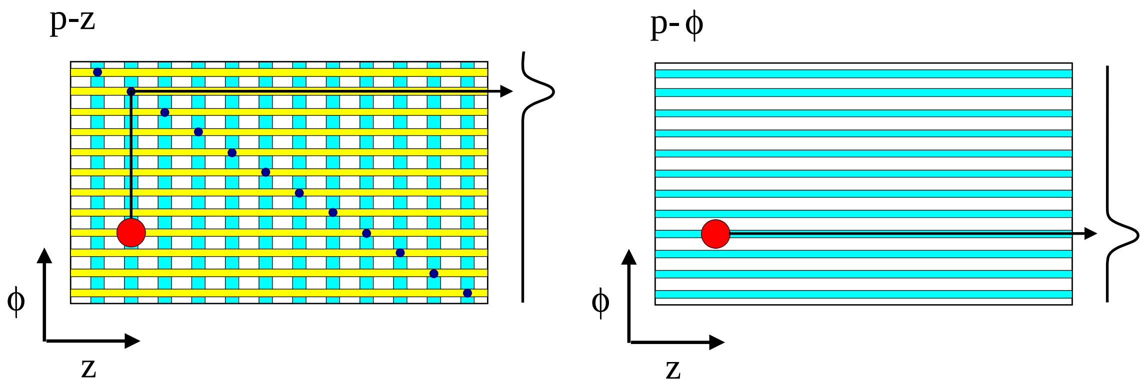

Figure 3.2: Diagram of p-z and p-ϕ detectors. The arrow shows the path the holes take from the light spot to the readout electronics.

of the detector was more than a factor of 5 weaker than the front side signal. We believe that this results from the fact that the multimode argon ion laser photons we use for illumination have a very small penetration depth in silicon when compared with the infrared photons or high energy charged particles that had been used previously. Since the electrons and holes are created near the front surface, the holes migrate to the p-type strips as expected, but the electrons appear to be trapped in surface states and do not migrate to the back plane immediately.

This has led us to use single sided detectors. These are only segmented on the front side and only read out one projection of the image. We have continued to use the double sided detectors that existed, but only read out the front side. It is not a great loss to use only single sided detectors since it is generally simpler to make two single sided detectors than one double sided one. Reading out two single sided detectors requires the same acquisition electronics as one double sided. One loss is that a beam splitter must be used to image onto the two detectors and so half the light is lost. It also creates some additional problems in aligning the two detectors.

The detectors we have used also come in two strip layouts. Most of them have the front p-type strips running along the short side of the detector, and are called p-z detectors. The other kind has p-type strips running along the long side of the detector, and are called p-ϕ detectors. This nomenclature results from the cylindrical geometry of the silicon in a high energy vertex detector in which the detectors can measure either z or ϕ. A diagram of each of these detectors is shown if Fig. 3.2. Because of the layout of the vertex detection systems, all the detectors are read out from a short side, so the p-z detectors have readout traces orthogonal to the strips that are connected to the p-type strips along a diagonal as shown. In the diagrams, The p-z detector measures the horizontal position of the light spot and the p-ϕ measures the vertical.

While testing the detectors we noticed a strange property of the p-z detectors that that has turned out to have some benefits. A weak negative signal marking the vertical position of the light spot is visible in addition to the expected positive signal marking the horizontal position. Our explanation of this is related to the reason the double sided detectors did not perform well, and is shown in Fig. 3.3. Since charge separation takes place in a

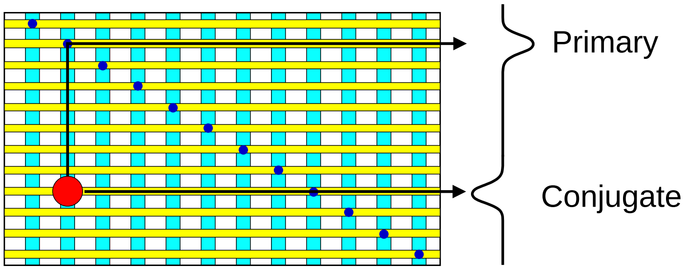

Figure 3.3: Diagram showing charge collection of the conjugate signal.

shallow layer near the surface of the detector, holes are quickly collected by the p-type strips and a positive signal marks the horizontal position of the light spot. However, the electrons are apparently trapped in surface states, and as a result they capacitively couple to the readout traces above them. This creates a negative conjugate signal that marks the vertical position of the light spot. The conjugate signal is not as reliable as the primary one, but it is often very useful to be able to read two coordinates from a single detector.

A listing of all the detectors used up to this point is in Table 3.1. All of the p-z detectors manufactured by Hamamatsu have worked quite well for the required imaging, although they have significant differences in conjugate peak characteristics. The one p-ϕ detector we tested was manufactured by CSEM and it performed much more poorly. It had about a factor of four lower light sensitivity. Tests are continuing to determine whether this is a geometry or manufacturer issue.

It is quite possible that significant improvement in the sensitivity of these detectors could be obtained if they were optimized for visible photon detection. The ones we have been using were designed for detecting high energy particles which deposit their energy through the bulk of the detector rather in a shallow surface layer as visible photons do. The current detectors have a major advantage though in that we have extra detectors freely available from the CLEO III prototype runs. We also have all the components and equipment for assembling them here at Cornell.

3.1.4 Readout electronics

A photograph of a completed detector with its front end readout electronics is shown in Fig. 3.4. The circuit board on which it is mounted is called a hybrid board. A schematic diagram of the hybrid board showing two channels of the detector and front end readout electronics is shown in Fig. 3.5. In the photograph, the detector is the grey rectangle at the left. The detector is reverse biased with a bias voltage ranging from 50 V to 160 V depending on the detector. 512 wirebonds connect the strips of the detector to the RC chips which contain a resistor and capacitor to AC couple each channel. The RC chips are the 4 large lighter chips at the center of the image. 512 more wirebonds connect the RC chips to VA1 (Viking) chips which contain individual preamplifiers, shapers, and sample and hold amplifiers. The Vikings also contain the multiplexers to create the analog output stream. We obtain the Viking chips from IDE AS, a company in Norway. There are 4 Viking and 4 RC chips with 128 channels on each. A major challenge in assembling

Table 3.1: List of detectors and their characteristics. DS stands for double sided. SS stands for single sided. p-z and p-ϕ label the orientation of the strips.

Label	Type	Manufacturer	Notes
H0	DS p-z	Hamamatsu	First detector. We began testing it in the summer of 1998. In spring 1999, Viking # 1 died–apparently because of a drop of epoxy on it. It has average conjugate signals that appear at 50 V bias.
H1	DS p-z	Hamamatsu	Identical to H0 except that this was used in radiation damage tests, and so has a much larger dark current. It also has stronger conjugate signals, which we believe is a result of the radiation. In fall 1999, 2 of its Vikings died.
MH1	SS p-z	Hamamatsu	First detector on a modified hybrid, Oct. 1999. Conjugate signals are weaker and appear around 100 V. Also has a strange coupling of channels 16 and 48 on each Viking chip.
MH2	SS p-z	Hamamatsu	Similiar to MH1. Built Nov. 1999. Has a wirebonding problem so that every other channel is shifted by two channels.
MH4	SS p-ϕ	CSEM	Built Dec. 1999. Has a wirebonding problem so that every other channel is shifted by four channels. Light sensitivity is about a factor of 4 lower than the others.

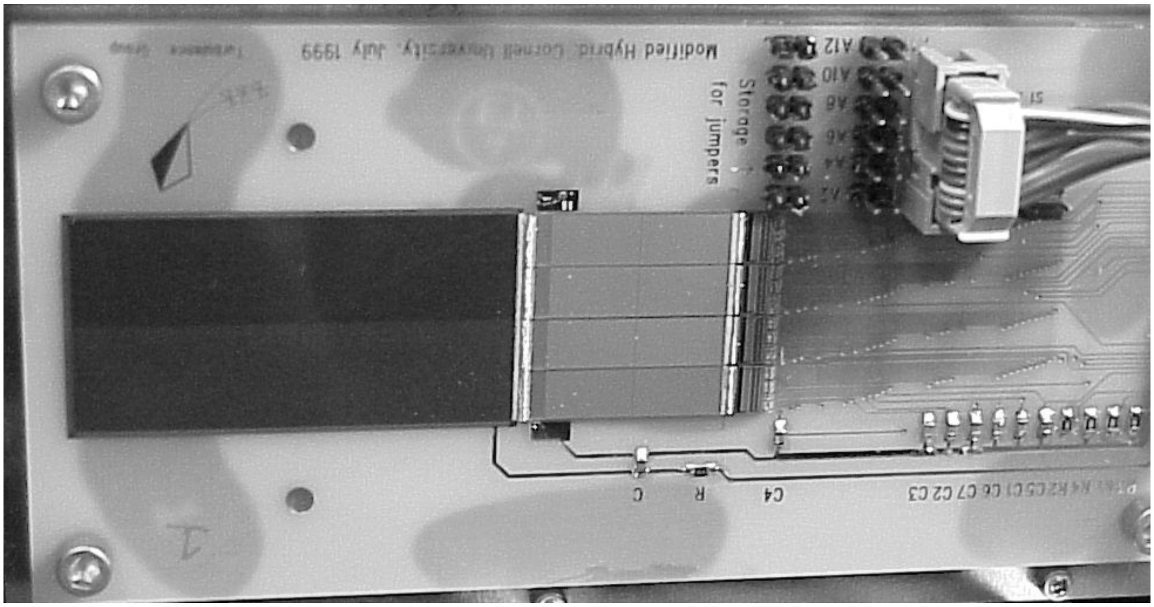

Figure 3.4: Photograph of a hybrid board containing a detector, RC chips, and Viking chips.

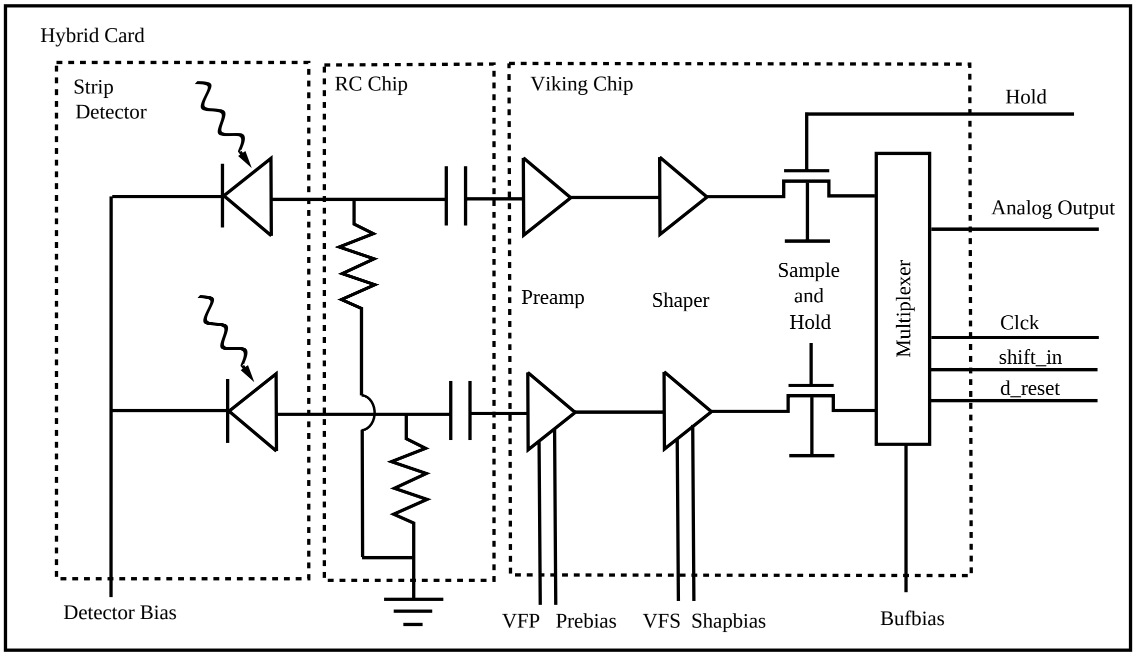

Figure 3.5: Schematic of the hybrid board

the detectors is make the $1024+$ wirebonds without producing too many dead channels. The 4% to 10% dead channels which we have achieved so far cause some difficulties in interpreting the data.

A major part of our work has been implementing a fast readout system for the strip detectors. In the CLEO detector system, 600 detectors are read out simultaneously at rates on the order of 50 Hz. For our application we want to read out a single detector as fast as possible, and thus needed to redesign the readout electronics. The solution we have developed can read out a sequence of 4000 frames at rates up to 70,000 frames per second on each of two detectors. Every frame contains of the intensity on each of 512 strips. It then takes about a second to process the data before being ready to acquire another sequence.

A block diagram of the system is shown in Fig. 3.6. The overall control of the system resides with the detector controller and the master computer.

The detector controller is a custom built digital card which contains the master clock. It produces the timing signals that sequence the readout of the Viking chips. It sends the clock and trigger signals that control the analog to digital converters in the slave computers. It drives the acousto-optic modulator (AOM) which modulates the illumination laser beam. The controller also manages the flow of data by exchanging digital signals with the master computer, sending a `trigger_done` signal when a sequence of frames has been acquired and waiting for a `computer_busy` signal to clear before re-enabling acquisition. At the beginning of a run, the master computer downloads parameters to the detector controller which determine the frame rate, number of frames per sequence and AOM illumination profile for acquisition. Details of the design and operation of the detector controller are in Appendix B.

The master computer's role is to mediate the data acquisition process, arming the slaves for acquisition, initiating data download and sparsification when the controller indicates that an acquisition is completed, and signaling the controller when the data has been downloaded and the slaves are rearmed. It also provides a user interface, allowing the configuration of all parts of the system to be specified in a single control program. The master and slave computers are all Pentium Pro 180 MHz machines.

TTL signals from the detector controller are passed to repeater cards which were designed for the CLEO detector. These convert the TTL signals to low voltage differential signals that are sent to the Vikings. The repeater cards also have potentiometers which control the currents and voltages needed to set Viking preamp and shaper parameters. (V_{FP}, V_{FS}, prebias, shapbias, bufbias). See the repeater card and hybrid card documentation books for more details. The values which were used for the repeater card potentiometers were: $V_{FP} = -0.013\mathrm{V}$, $V_{FS} = 0.164\mathrm{V}$, $\mathrm{prebias} = -0.5\mathrm{V}$, $\mathrm{shapbias} = -0.029\mathrm{V}$, and $\mathrm{bufbias} = -0.024\mathrm{V}$. These were chosen by putting a light spot on a detector and adjusting the potentiometers to maximize signal and minimize ringing on subsequent frames. This can be done by gating the AOM signal with a square wave generator and an AND gate. When the repeater potentiometer settings were rechecked recently they seemed to have changed significantly. It would likely be useful to monitor these settings more closely in the future.

The analog outputs from the Vikings are passed through differential amplifiers before

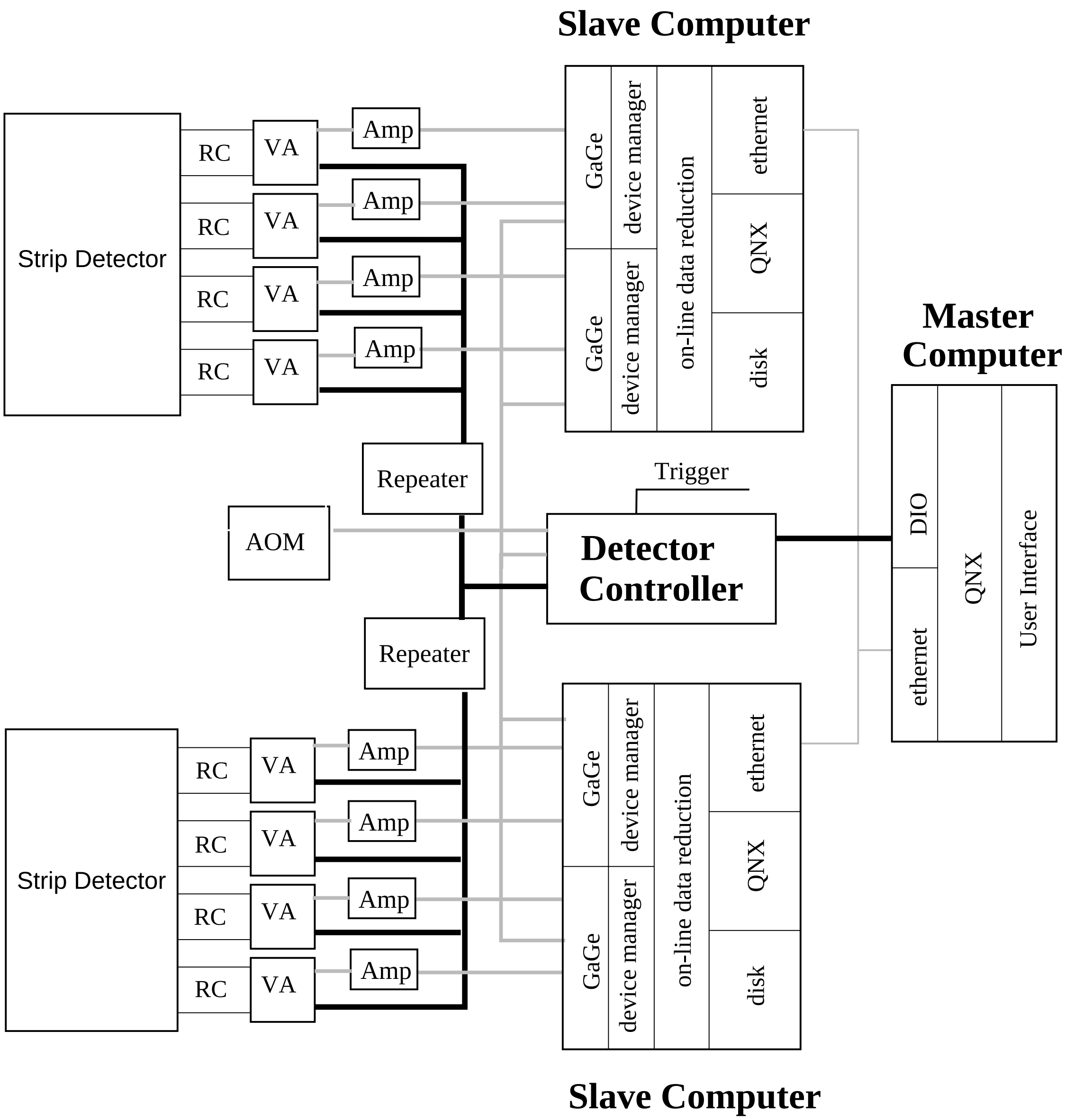

Figure 3.6: Block diagram of the readout electronics.

being converted to digital. These are high speed differential amplifiers with voltage gain of 41.6.

The actual analog-to-digital conversion of the strip detector output is done in the slave computers. Each slave acquires, processes, and stores the data from one detector (512 strips). Each of these computers is equipped with two high speed GaGe 12-bit signal acquisition cards, giving each slave four input channels that can each operate at rates up to 30 MHz. Each input channel digitizes the analog signal from one Viking chip. We normally operate with a 10 MHz readout clock. These cards have enough on-board memory to acquire 4,000 frames of data. Each card is controlled by a device manager process which allows the cards to be remotely configured, armed for acquisition and read out in response to messages sent by the master computer. Each of the slave computers also runs an on-line analyzer process which, when prompted by the master program, copies the data from the device manager process, sparsifies the data by applying configurable threshold conditions, and writes the data to a local disk file in a compressed format. The software is designed so that on-line processing can be performed concurrently with acquisition of the next sequence of frames.

3.1.5 User interface software

There are two programs that can be run on the master computer to control the acquisition process. The X-windows application `grab_seq` allows interactive data acquisition for testing and debugging. The command line program `master` is a noninteractive data acquisition program, which repeatedly signals the slaves to acquire data, measures propeller speed and temperature and maintains a small data file containing this data and an index to the data recorded by the slave computers. Arthur La Porta wrote these programs and has provided complete documentation in the group web pages.

The procedure for acquiring data is as follows:

- Run `slave_setup` on each of the slaves from the directory the data will be written to. This starts `g_server` processes for each of the GaGe boards, and starts a `chopper` process.
- Write a master configuration file for the run that has the right parameters for reading the Viking pedestals, and load it into `grab_seq`. (This requires that the zero files contain all zeros and that `chopper_align` is set to 1.)
- Grab a sequence and save the channel means to a zero file.
- Write another master configuration file with the same parameters as before but `chopper_align = 2` and the new zero files.
- Load the new master configuration file into `grab_seq` and acquire data interactively or run: `master <cfg file>`.

Failure modes to be aware of include:

- If the detector controller is not powered up when the master configuration is loaded, the slave computers will hang since the GaGe cards never get a clock signal.
- Changing the frame rate, AOM settings, bias voltage or repeater card settings will change the pedestals. Be sure to make new zero files when these are changed.

3.1.6 Data analysis software

Track identification

The raw data from the strip detectors are stored on hard disks on each of the slave computers. A master file which indexes these files is stored on the master computer. The first step in analysis is to extract the particle trajectories from raw data. The code `seq_track` performs this task. It was written by Arthur La Porta and is documented on the group web pages.

The task is divided into four stages, peak detection, tagging, track building and splicing. Below, we give a grossly simplified description of the algorithms.

peak detection Each frame is scanned for peaks. Peaks are found by marking all groups of pixels that go above a threshold. For each frame, a list is compiled of all peaks found and their properties, such as position, area, peak amplitude, moments, etc.

tagger The tagger assigns a tag (an integer) to each peak in the first frame. It then advances to the next frame and determines whether each peak in that frame corresponds to a peak in the previous frame, applying the condition that they must be mutual nearest neighbors. When a peak is recognized as the continuation of a peak in the previous frame, the tag is copied to the new peak. Peaks not identified are assigned new unique tags. The process is repeated for all of the frames in the sequence. The result is that all the peaks that make up continuous tracks are given a common tag number.

track builder The track builder simply scans through the list of peaks and groups all peaks having identical tags into tracks.

splicer The tracks obtained from the track builder are generally short segments which must be spliced into larger tracks. This is because the tagger only looks one frame ahead to assign tags. A track becomes broken if a peak is missing (because it hit a weak pixel, or because an amplitude fluctuation brought it below threshold) or if an ambiguity occurred, such as two tracks crossing. The splicer inspects the tracks and determines if two segments should be joined into one track. This is done by an iterative algorithm which scans all of the tracks and joins the pair that have the highest figure of merit, repeating until no splicable pair remains.

The track identification program is actually more complicated than is described above, having approximately 50 tunable parameters which are adjusted to effectively analyze data taken under different conditions. Particular care is used in resolving ambiguities caused by non-ideal circumstances, such as dead pixels, crossing of tracks, and multiple reflections from particles.

Matching different coordinates

The next step in the analysis procedure is to match the tracks that were measured on different detectors into full trajectories. A working version of a general purpose code to do this has been written. For the results reported in this thesis though, I have used a simple version that matches two sets of tracks when the particle density is low. The idea behind the matching is that even though the strip detector does not give the information to match the coordinates from different detectors, intensity correlations and position correlations can be used to make the proper matches.

When two detectors view particles through the same light collection optics, the intensity of the signal recorded by the detectors are highly correlated. When the detectors use different optics, the correlation is not nearly as good. There are several ways that the intensity can be different when different optics are used. One is that the detectors are not viewing the exactly the same illumination volume. Another is that the scattered intensity from the particles has some fast time scale fluctuations that are caused by either surface inhomogeneities of the particles or by other particles interfering with the beam. These fast time scales are not well correlated across different optical axes. Eventually we plan to match two coordinates from the same optics, and then use a shared coordinate to match this to two detectors on different optics. Since the data reported in this thesis generally only concerns single coordinate statistics, matching was unnecessary. In the few instances where matching was used, tracks were matched when they were in view at the same time and had a higher intensity correlation than any other particle in view. This has problems when tracks are broken up and many particles are in view. It was more than sufficient for the current data, even for detectors on different optical axes, because the data rarely had more than one particle in view at once.

Statistical Analysis

The final data analysis program takes track files and calculates statistics of velocities, accelerations. This code is called `ant` for “ANalyze Tracks”. Details are discussed along with the results in Chapter 5.

3.2 Optical System

3.2.1 Requirements for the optical system

The process of illumination and imaging tracer particles onto the detectors seems quite straight forward, but it turns out that it contains some significant challenges as well. The fundamental issue is that tracking particles over significantly long times requires illumination of a somewhat large volume in the flow. In order to achieve reasonably well focused imaging of the full volume (large depth of field), the numerical aperture of the optical imaging system must be quite small. Further, the tracer particles must be kept small enough that they resolve the smallest scales in the flow. The result of these constraints is that it is difficult to collect enough light. The illumination sources that can be

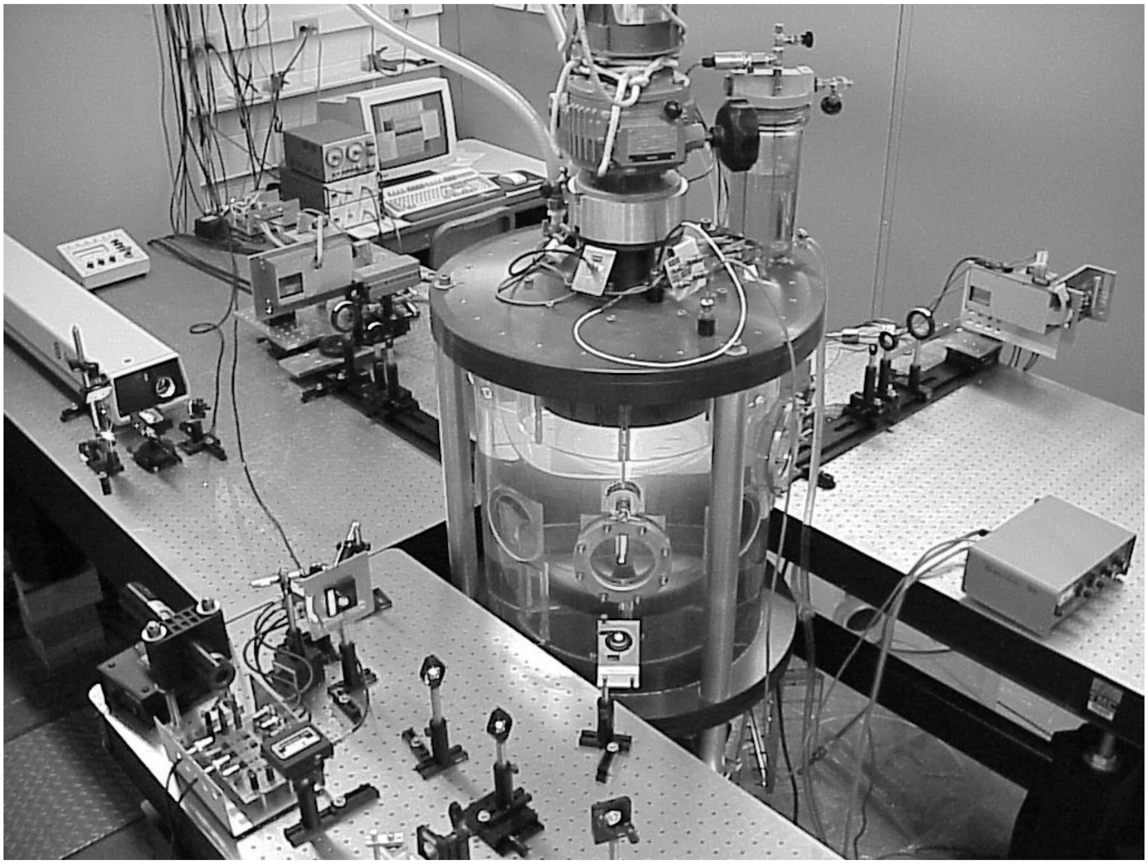

Figure 3.7: Photograph of the flow, optics, and detectors.

used are limited by the fact that the strip detectors are AC coupled and so the illumination must be flashed at the frame rate.

This limit on illumination intensity is one of the reasons why the first measurements we have pursued with the strip detector system are acceleration measurements. Since the tracking time necessary to make acceleration measurements is small, the illumination beam can be small and intense. Acceleration measurements require extremely high spatial resolution which places stringent requirements on the imaging system and the tracer particles. This section describes the optical system that we have built to meet these requirements. Figure 3.7 is a photograph of the flow and optical system. A diagram of the illumination and imaging is in Fig. 3.8

3.2.2 Illumination

A 5 Watt Spectra Physics Stabilite 2016-05RS Argon ion laser is used for the illumination beam. It is operated multiline, and produces most of its power at 514.5 nm and 488.0 nm. Laser illumination is necessary because the AC coupled detectors require that the illumination be flashed at the frame rate. Our frame rates range from 10 kHz to 70 kHz. Pulsed illumination in this frequency range is difficult to obtain. Frequencies of strobe lamps are

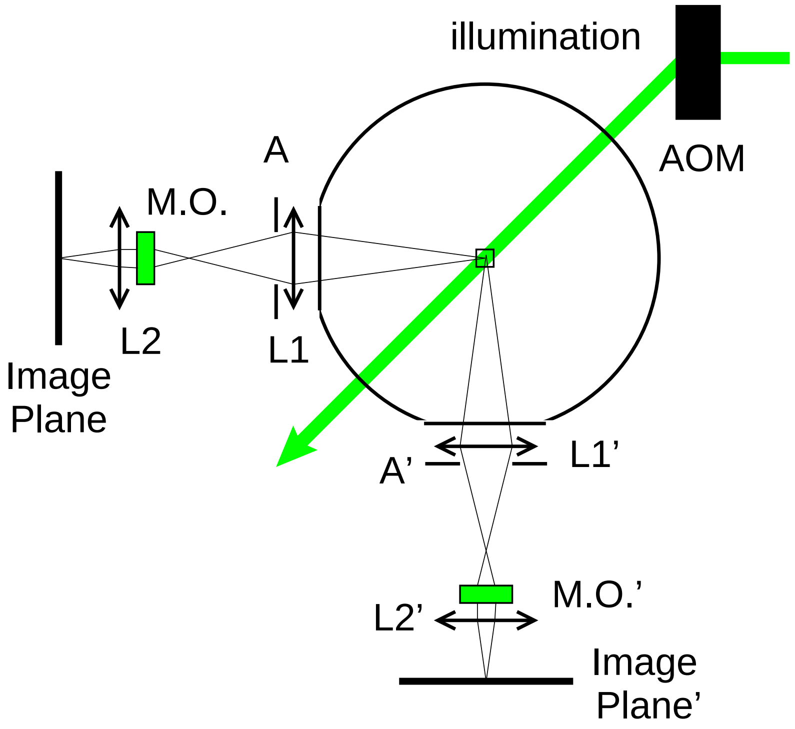

Figure 3.8: Optical configuration used for acceleration measurements. Abbreviations are: AOM–acousto-optic modulator, L1 and L2–lenses, A–Aperture, MO–microscope objective

too low. Q–switched lasers are also too slow. Mode locked laser beams are too fast. The solution we have found is to use a CW laser beam and modulate it with an acousto-optic modulator. The argon ion laser also has advantages of good pointing stability and low beam divergence.

The acousto-optic modulator is model AOM-40 from IntraAction. The detector controller creates a TTL square wave that determines when the illumination is on. This is run through an op-amp circuit to shift the zero level and amplitude of the square wave before sending it into the AOM signal processor. The signal processor creates the modulated 40 MHz signal that drives the acoustic wave in the AOM. When carefully tuned, the AOM can diffract 90% of the photons into the first order beam. Tuning is accomplished by measuring the diffracted beam with a photodiode and adjusting the angle of the AOM and the amplitude and offset of the control signal.

The first order diffracted beam is passed through a telescope to adjust its diameter and then directed into the turbulence chamber. One issue is that the AOM produces slightly different diffraction angles for different optical wavelengths. The difference between the 488 nm and 514.6 nm is 0.000268 radians, which results in 0.54 mm distance between the beams at 2 meters. I calculated that this can be almost totally corrected by using a weak prism (8.6° for BK 7 glass). Since our illumination volume is about 2 mm in diameter, we have simply used a slightly elongated beam rather than order and install a custom prism.

For the acceleration measurements, a cylindrical beam typically 2 mm in diameter is used. For the measurements of the energy dissipation described in section 4.7, a light sheet 0.2 mm by 2.0 cm was used.

3.2.3 Tracer Particles

The tracer particles are a crucial part of the optical system. They not only must adequately follow the flow, but they must be spherical and highly uniform because we measure their position with accuracy of a small fraction of their diameter.

The only particles we have found that are near the density of water and meet these requirement are polystyrene DVB spheres. These are available from several companies in diameters from 20 nm to 1 mm because of their wide use in biochemistry. We have found Duke Scientific to be the most reliable supplier. Spheres with diameter less than 50 $\mu\mathrm{m}$ must be purchased with the desired size distribution, since it is difficult to sieve particles of this size. Spheres larger than 50 $\mu\mathrm{m}$ can be sieved from batches with wider size distributions.

Transparent particles such as these have much stronger forward scattering than at 90° We originally used illumination orthogonal to the imaging axis since this makes the simplest illuminated volume. Since we are illumining a volume though, we can use a forward scattering geometry where there is much more light with only a modest increase in the depth of the illumination volume. We have settled on 45° forward scattering as shown if Fig. 3.8 because it allows two orthogonal imaging systems to be used.

Another major advantage of 45° forward scattering is that the multiple reflections from transparent particles are suppressed. Figure 3.9 shows light scattering from a polystyrene sphere. A 700 $\mu\mathrm{m}$ sphere was glued onto a small wire and illumined with a large beam

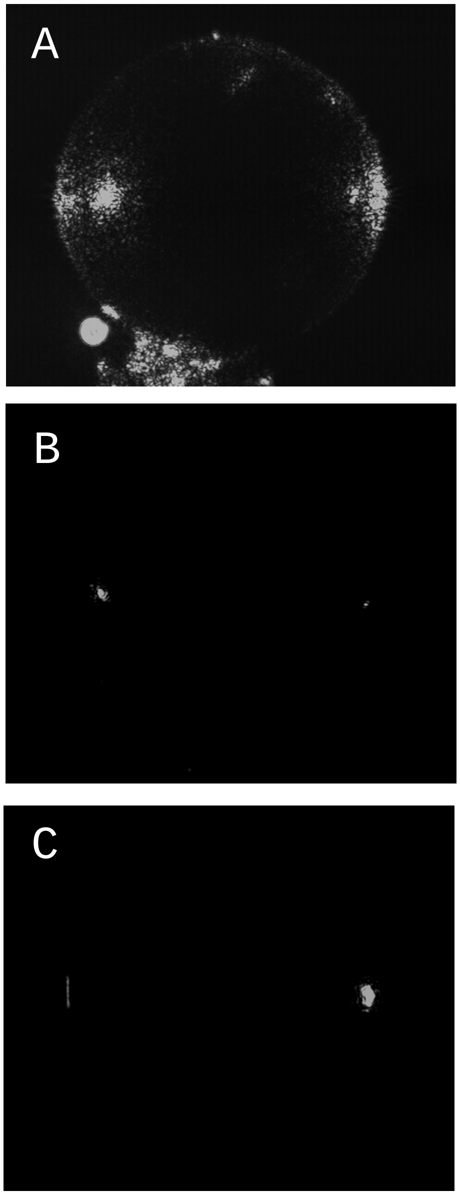

Figure 3.9: Images of light scattered from polystyrene spheres. A) Overexposed image from 90° showing the outline of the approximately 700 $\mu\mathrm{m}$ sphere. The wire with which the sphere is supported is visible at the bottom. B) Image taken from 90°. C) Image taken from 45° forward scattering.

from a laser. For tracer particles, we typically use particles in the 25–500μm size range. These are large enough that the distribution of scattered light should not depend on the particle size, so the 700 μm sphere should be representative. These images are of the particle in air, although qualitatively similar effects are observed when the sphere is in water. Figure 3.9A was overexposed to show the outline of the particle. The support wire can be seen at the bottom of the image. The light beam is incident horizontally from the left. Note the position of the primary external reflection on the left and the internal reflection on the right. Figure 3.9B shows that at 90° both reflections are visible although the external one on the left is brighter. Figure 3.9C shows that at 45° forward scattering the internal reflection on the right is much brighter. It had to be overexposed in order to even see the reflection on the left. The camera shutter speed was adjusted so that both images B and C were not saturated, but the 45° actually has much higher intensity. In our first measurements taken at 90°, the secondary reflection was a major problem because sometimes when the primary reflection was blocked, the secondary position would be chosen as the position of the particle.

Another important factor is that the reflections are different for different polarizations of the illumination. Figure 3.9 shows the vertical polarization. When horizontal polarization is used, the external reflection on the left is suppressed even more. The result is that using horizontally polarized light at 45° forward scattering produces only one bright spot which is ideal for particle tracking.

Note that the size of the spot is a very small fraction of the particle diameter. This is necessary since we measure particle positions with accuracy of better than 0.5μm which for 50μm particles is 1% of the particle diameter. It is essential that the particles have very good surface quality to allow positioning with this accuracy. The evidence suggests that polystyrene particles are sufficiently optically smooth for this purpose. As will be discussed in Chapter 6, when we increase the particle diameter, the measured acceleration variance decreases. This suggests that surface inhomogeneity is not a major contribution to the acceleration, although it might just be smaller than the effect due to the particles not following the flow. The most convincing evidence is that when a component of the acceleration of individual trajectories is measured from two orthogonal optical axes, the measurements agree very well. This data is shown in Section 4.9.1. Any motion due to surface inhomogeneity should not be correlated between different angles of view.

3.2.4 Imaging Optics

A two stage imaging system shown in Fig. 3.8 is used to obtain the high magnification imaging needed for acceleration measurements. First, a 15 cm positive doublet (L1) images the central part of the flow out of the turbulence chamber at roughly 1 to 1 magnification. An aperture with diameter 1.3 cm is placed directly behind this lens. A 3.81 cm acromat placed 36 cm behind the first lens magnifies this image onto the detector. Two additional lenses follow. A 30 cm positive lens 5.4 cm after the short focal length lens allows the short focal length lens to be operated at nearly infinite conjugate ratio. This minimizes aberrations when an optional beamsplitter is placed between these lenses. A 50 cm negative lens is placed 18.6 cm behind the 3.81 cm lens to allow easy adjustment

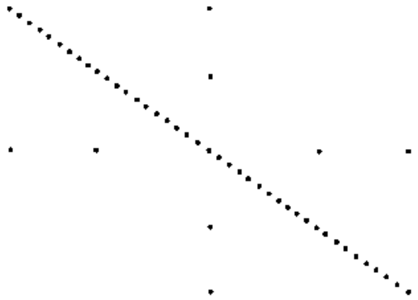

Figure 3.10: Pattern on the calibration masks.

of the magnification. The magnification of the system is 13.2. All of these components and the detectors are mounted on an optical rail.

3.2.5 Calibration

The calibration procedure involves imaging some known calibration rule onto the detector. The strip detector requires a one dimensional pattern that is illumined with synchronized AC light. An effective way to achieve this is to place a mask containing a line of holes in the flow and illumine it with the laser beam.

The nanofabrication center at Cornell was very helpful in making masks suitable for this purpose. The standard mask making techniques they use for lithographic masks produced excellent results. With the GCA PG3600F Optical Pattern Generator we made four masks of the pattern shown in Fig. 3.10, each with a different magnification. They were all made on one 5 inch blank and sawed into four plates on the diamond saw in the materials services shop. Each has 41 dots placed along a diagonal line with 8 additional alignment dots. Each dot is an octagon, made by 4 flashes of the pattern generator. The positioning accuracy of the pattern generator is 0.6 $\mu\mathrm{m}$, much higher than is necessary. The dimensions of the entire pattern is $a \times a\sqrt{2}$, which allows the mask to appear square when viewed from a 45 degree angle. This means that the angle of the diagonal is 35.2644 degrees. The orientation marks are on the horizontal and vertical centerlines with spacing $a/4$ between vertical dots and $a\sqrt{2}/4$ between horizontal dots. The dimensions of the four masks are

- 3 cm: 3cm x 4.24264cm, dot diameter 150 microns, spacing 0.12990 cm
- 1 cm: 1cm x 1.41421cm, dot diameter 50 microns, spacing 0.04330 cm
- 0.5 cm: 0.5cm x 0.70711cm, dot diameter 25 microns, spacing 0.02165 cm
- 0.2 cm: 0.2cm x 0.28284cm, dot diameter 10 microns, spacing 0.008660 cm

where spacing is the distance between dots along the diagonal line.

For calibration of the high magnification setup, we placed the mask perpendicular to the laser beam in the detection volume defined by the beam and the field of view of the two optical systems. A piece of opal glass was placed behind the mask in order to scatter light to the detectors. The optical rails were on orthogonal axes and each had a detector that could measure both the primary and conjugate signal, and so we measured four projections of the image. The relative magnification of the two optical systems could be found from the two vertical coordinates, but we have a better measurement from data in which particle tracks are recorded with two detectors measuring the vertical coordinate. This gives $M' = 1.0106M$. Then the combination of the spacing of the light spots on the three orthogonal projections yields: $M' = 13.266$ and $M = 13.127$. To obtain the calibration of strip number to position in the flow, divide the strip pitch, $50\mu\mathrm{m}$ or $100\mu\mathrm{m}$, by the magnification. Estimate of the magnification uncertainty based on the uncertainty in the calibration position measurements yields 0.4%. The deviation between the independent vertical measurements suggest that systematic effects may raise this to about 1%.

This procedure assumes that the magnification does not change across the depth of the illumination volume. A geometric optics simulation of the system using the gaussian package written by Arthur La Porta shows that the magnification of our high resolution setup varies only by $\pm 0.3\%$ when the depth of the particle is moved by $\pm 1\mathrm{mm}$. A more complete calibration of the optical system would involve moving the calibration mask to measure the full mapping of actual position in the flow to measured coordinates as in Dracos (1996). This will require a full 3D imaging system. With this kind of an approach, much greater precision is possible since parameters such as the viewing angle and optical distortions can be measured directly from the images.

3.2.6 Focusing

The optimal focus for the optical setup is found by taking data and measuring the width of the light spots that are recorded. Because the illumination beam is at 45° with respect to the optical axis, the center of the beam is changing its distance from the optics as it moves horizontally across the cell. In the measured data, the average width of the light spot will be smallest at the horizontal position where the beam centerline passes through the focal plane. By measuring the average width of the light spots as a function of position, the direction and amount of the necessary focus adjustment can be determined.

After a rough focusing by eye, the focus is fine tuned as described above. It usually takes two iterations of 30 minutes of data each to focus a detector. This procedure does not work if the detector is measuring the vertical coordinate. In this case, a horizontal detector was used for focusing and then a vertical detector was mounted in the same place.

3.3 Large Reynolds number flow

The turbulent flow used in these measurements is a flow between counter-rotating disks. This flow has been used by several other groups, particularly in France (Douady et al, 1991; Fauve et al, 1993; Maurer et al, 1994). Details of the geometry of the system were

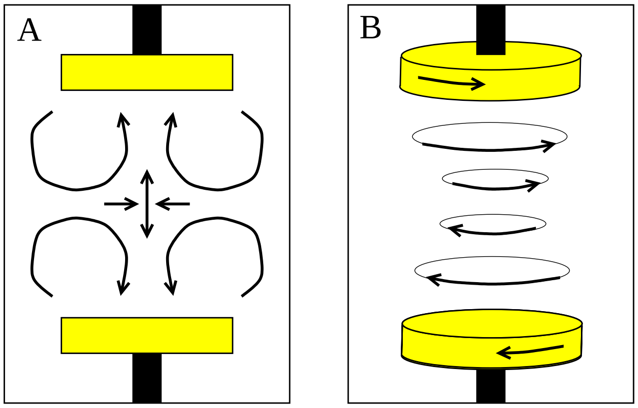

Figure 3.11: Primary modes of the mean velocity in the flow between counter-rotating disks.

published in our first paper (Voth et al, 1998), and are reprinted here in Appendix A, section A.1.3.

The one modification to the apparatus itself since the description in Appendix A is that there are now 8 circular 4 inch diameter windows placed symmetrically around the centerline of the flow. This allows imaging from two ports both at 45° forward scattering and entry and exit of the laser beam all through glass windows. Two removable windows allow access to the interior of the cell for mounting calibration equipment.

The structure of the mean velocity field in the flow can be thought of as the sum of two components, a toroidal pumping mode and a cylindrical shearing mode. Figure 3.11 gives a schematic representation of these two modes. The resulting flow is quite complex, but has two major advantages for Lagrangian measurements. First, the central region of the flow has zero mean velocity which is ideal for particle tracking. Second, it can produce large Reynolds numbers in a confined environment which allows it to meet constraints for optical access and available laboratory space. The inhomogeneity of the flow is a major concern. This is another reason why we have focused on acceleration measurements, since measurements involving longer tracking times would have larger effects from the structure of the forcing. At large Reynolds numbers, small scale quantities like the acceleration should become at least partially decoupled from the large scale structure of the flow. We do find a small dependence of the acceleration statistics on the large scale anisotropy of the flow. In the future it will be very interesting to see similar measurements made in other flows to study this in more detail.

The disks are driven by 2 DC electric motors each rated at 1 horsepower. Variable speed reducers connect the motors to the disks. The rotation frequency of the motors is feedback controlled. There is a hole in the shaft driving each disk and an infrared LED and photodetector mounted on the housing at the same height. As the shaft turns a pulse of light is measured on the photodetector every half turn. The frequency of this signal is sampled with a Keithle 2001 multimeter. The master computer reads this over GPIB and feedback controls the frequency by adjusting the the power supplies driving the motors. When the disks are run at frequencies below 1.25 Hz, a Tektronix oscilloscope is used to measure the frequency since the Keithley is limited to frequencies greater than 1 Hz. The power supplies are controlled with a voltage from an analog I/0 card in the computer. There are four Kepco model ATE 55-10M power supplies with two in series powering each motor. The computer code for the frequency control is `turb_readout`.

The temperature of the system is controlled by a Tronac model PTC-36 temperature controller. This is an analog PID controller which adjusts the power output to a heating element to minimize deviations between the measurements from its thermistor probe in the flow and a set point. The heating element is in a water loop that circulates through the top and bottom plates of the flow chamber. This recirculating loop also has a heat exchanger through which building cooling water flows. Since we need a very wide dynamic range in heating and cooling power, we manually adjust the flow rate of the building cooling water and the power to a constant heater so that only small heat input from the temperature controller is needed.

The turbulence chamber has a filtration loop connected to it which allows removal of any particulate matter from the flow. A rough filter is followed by a $0.45\mu\mathrm{m}$ filter. Running the filter system and the disks for about one day is necessary to clean the flow. There is a steady release of very small particles into the flow from the walls, *etc.* These can be seen moving through the laser beam and increase in number over a period of weeks. They are small enough and increase slowly enough that there is a negligible contribution to measured trajectories of $50\mu\mathrm{m}$ particles over a data run of several weeks. If particles smaller that $15\mu\mathrm{m}$ are going to be used, this may become a significant issue. It is also very useful to de-gas the fluid to be certain that there are no air bubbles in the flow. For a while, this was done by raising the temperature of the system to about $40°C$ and then lowering it. More recently, a mild vacuum has been used.

Chapter 4

Particle Acceleration Measurements with Silicon Strip Detectors

4.1 Introduction

This chapter presents the acceleration measurements we have made with the strip detector system. After discussing the experimental procedure in section 4.2, I will discuss measurements of the shape, variance, and flatness of the acceleration probability distribution in sections 4.3 to 4.5. Measurements of the velocity and dissipation which are necessary for normalization and comparison with previous work are described in sections 4.6 and 4.7. In the process of checking whether our tracer particles were small enough, we recorded measurements of the effect of particle size on the acceleration variance which are reported in section 4.8. Finally I address some of the sources of measurement error and sample bias in section 4.9.

4.2 Experimental Procedure

Most of the data reported in this chapter was taken with two silicon strip detectors on perpendicular optical systems as shown in Fig. 3.8. For most of the runs, detector MH1 was oriented to measure the horizontal position which will be labeled x, and detector MH4 was oriented to measure the vertical position, y.

Since MH1 is a p-z detector and MH4 is a p-ϕ detector, this combination of coordinates is measured when both detectors have their long axis horizontal. This takes advantage of shape of the laser beam and should allow the two detectors to have the same shape and dimensions of their detection volumes. Unfortunately, detector MH4 produces a signal that is weaker than MH1 by almost a factor of 4. As a result, the detection volume for MH4 is significantly smaller, since a smaller part of the gaussian beam has enough illumination intensity to pass the intensity cutoff.

Two runs were taken with the detectors in different orientations to check for systematic errors. One had both detectors measuring y. The other had both detectors measuring a horizontal coordinate which means MH1 measured x and MH4 measured z.

Table 4.1: Parameters for data runs measuring accelerations with the silicon strip detectors.

f (Hz)	$\tilde{u}$ (m/s)	R_λ	ϵ $\mathrm{m}^2/\mathrm{sec}^3$	τ_η ms	η $\mu\mathrm{m}$
0.15	0.0179	140	8.13×10^{-5}	110	330
0.20	0.0241	160	1.97×10^{-4}	70.7	264
0.30	0.0364	200	6.90×10^{-4}	37.8	194
0.60	0.0742	280	5.76×10^{-3}	13.1	114
1.75	0.220	490	1.50×10^{-1}	2.57	89
3.50	0.440	690	1.12	0.940	30
7.00	0.869	970	9.24	0.327	18

A list of the parameters at which data was acquired is in Table 4.1. f is the rotation frequency of the disks. The typical velocity used for scaling is $\tilde{u} = (\langle u_i u_i \rangle / 3)^{1/2}$, where summation is implied. (When u_z was measured it had the same variance as u_x, so u_x was used in place of u_z in the cases where u_z was not measured.) ϵ is the energy dissipation per unit mass, and is determined by $\epsilon = u^3/L$ where $L = 0.071$ m is measured in section 4.7. $\tau_\eta = (\nu/\epsilon)^{1/2}$ is the Kolmogorov time scale, and $\eta = (\nu^3/\epsilon)^{1/4}$ is the Kolmogorov length scale. The water temperature for all the runs was $20.60 \pm 0.03° \ C$, where the uncertainty reflects measured temperature fluctuations. The absolute temperature calibration uncertainty is about $0.4° \ C$. The kinematic viscosity was $0.989 \pm 0.010 \times 10^{-6} \ \mathrm{m}^2/\mathrm{s}$. This viscosity is from an interpolation of the data in the CRC Handbook of Chemistry and Physics (Robert C. Weast, 1997), and agrees with the value measured with a viscometer to 1%.

The tracer particles were polystyrene DVB spheres from Duke Scientific with 46.6 $\mu\mathrm{m}$ mean diameter and 6.6 $\mu\mathrm{m}$ standard deviation in diameter. Their density is 1.05 g/cm^3. It is shown in section 4.8 that these particles are sufficiently small that the particle acceleration variance is equal to the Lagrangian acceleration variance within the experimental errors.

Figure 4.1 shows an example of a particle trajectory recorded with a strip detector. The top grey scale plot shows the raw data recorded by the data acquisition system. Background grey areas were not stored by the sparsification algorithm. Other areas show the signal voltage on that strip in grey scale. In addition to the primary track, there is a very faint conjugate track and a few random pixels were bright enough to pass the sparsification threshold. The track crosses a few dead pixels which are marked by no intensity when they should be bright.

When this sequence is processed with `seq_track`, the positions shown in the middle plot are obtained. A list of dead pixels is used to ignore positions that are within 1 pixel of a dead pixel, resulting in the breaks in the data. Velocities calculated from linear fits to 15 time steps ($0.23\tau_\eta$) are shown in the lower plot in Fig. 4.1. The slope of this curve appears to be sufficiently well defined to allow accurate acceleration measurements. There is some ambiguity though about whether some of the very fast changes in acceleration are caused

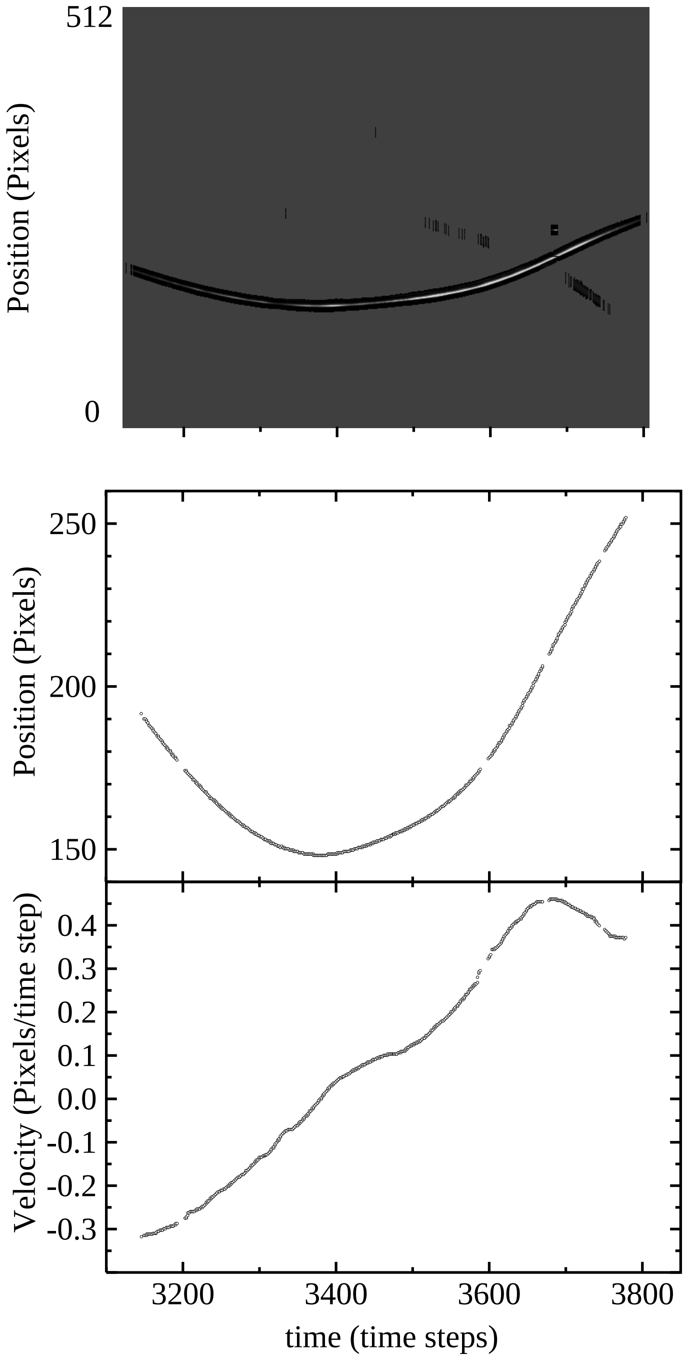

Figure 4.1: Example of a trajectory measured by the strip detector used to obtain accelerations. The disk rotation frequency is 3.5 Hz which corresponds to $R_\lambda = 690$. 512 pixels corresponds to $3.88\mathrm{mm}$ in the flow. The readout period is $14.3\mu\mathrm{s}$, which is a frequency of 69,930 Hz, or 66 time steps per Kolmogorov time.

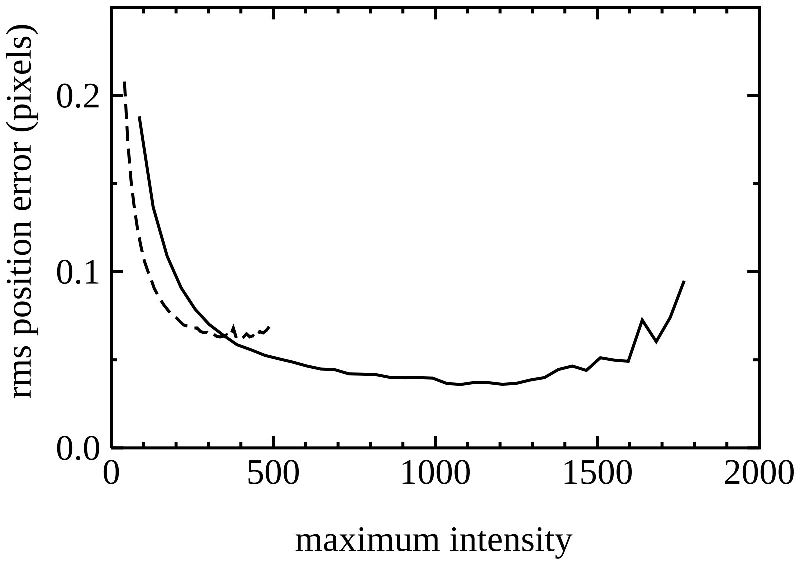

Figure 4.2: RMS position measurement error as a function of the maximum intensity of the trajectory in that frame. Solid line is for detector MH1. Dashed line is for detector MH4.

by position measurement errors or by the turbulence.

For the acceleration measurements, the seed particle density was typically adjusted so that 10% to 25% of the frames had a pixel above threshold. This was chosen as a balance between maintaining a reasonable data rate and minimizing ambiguities caused by multiple particles in view at once. This data set had at least one pixel above threshold in 16.9% of the frames which resulted in 0.6% of the total data being stored.

The position measurement error can be estimated by deviations of the measured position from a fit to the trajectory. Figure 4.2 shows the rms position measurement error as a function of the maximum intensity of the trajectory in that frame. In this case, the fit used to determine the error was a quadratic polynomial fit to 33 time steps, or $0.5\tau_\eta$. For the brightest trajectories, the position error is less than 0.05 pixels which corresponds to $0.4\mu\mathrm{m}$ in the flow. Position measurement errors in this range are common for CCD imaging systems, for example Mann et al (1999) report measurement errors in the range 0.02 to 0.1 pixels.

Figure 4.3 shows a distribution of the measured maximum intensity. The total rms position measurement error can be calculated by summing over the data in Fig. 4.2 weighted by the probability from Fig. 4.3. It clearly has a strong dependence on the intensity threshold that is chosen. For high threshold, the measurement error is smaller, but many fewer tracks are found and there is more likelihood of breaking up tracks. For the x data set from MH1 with a threshold of 80 counts, the rms error is 0.083 pixels.

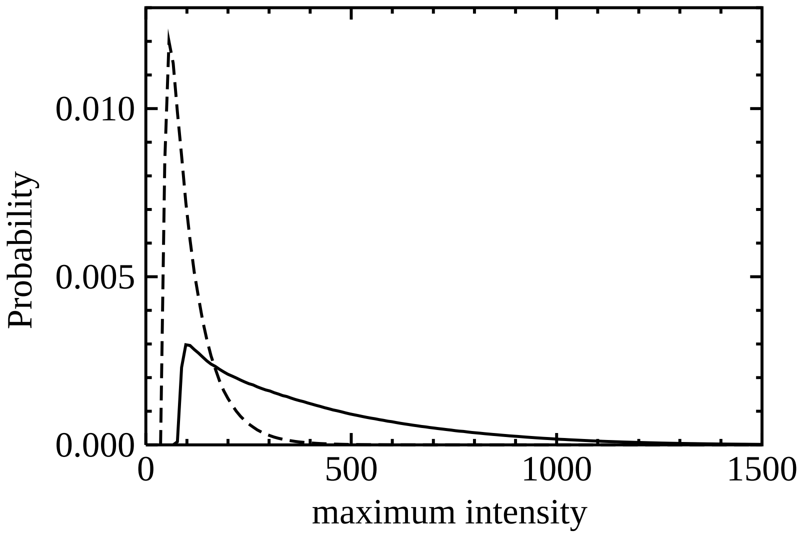

Figure 4.3: Probability distribution of maximum intensity. Solid line is for detector MH1. Dashed line is for detector MH4.

4.3 Acceleration Probability Density Function

Particle accelerations are measured by parabolic fits to the position versus time data. The parabolic fits use the error as a function of intensity as shown in Fig. 4.2 for the measurement errors. A triangle windowing function is used to weight the points at the center of the fit more heavily. This does not seem to be essential though since a rectangle windowing function with half the width produces results that are not significantly different.

The trajectories are sampled at equally spaced points along their length, typically with spacing between samples of 0.1 times the total fit length. This results in a weighting of the tracks by their residence time. Very small spacing between samples can make the probability distributions look smooth, but has very little effect on the convergence of moments since the samples are highly correlated.

4.3.1 Probability distribution of an acceleration component

Probability distributions of an acceleration component measured at three different Reynolds numbers are shown in the log-linear plot in Fig. 4.4. The acceleration is normalized by the measured rms acceleration which is discussed in detail in section 4.4. The first thing that stands out is the long stretched exponential tails. The distributions for the three Reynolds numbers are quite similar, although the $R_\lambda = 200$ data has somewhat weaker tails. The accelerations of the two higher Reynolds numbers are measured by quadratic fits to 1 Kolmogorov time. The $R_\lambda = 200$ data is from fits to 0.5 Kolmogorov times. This data set uses $0.5\tau_\eta$ for the fit time because very few particles are tracked for $1\tau_\eta$ time at this low Reynolds number. The effect of the shorter fit time should be to increase the strength of the tails, so the tails are definitely weaker than at higher Reynolds number. As shown in section 4.5, caution must be used in making conclusions that depend on small changes in

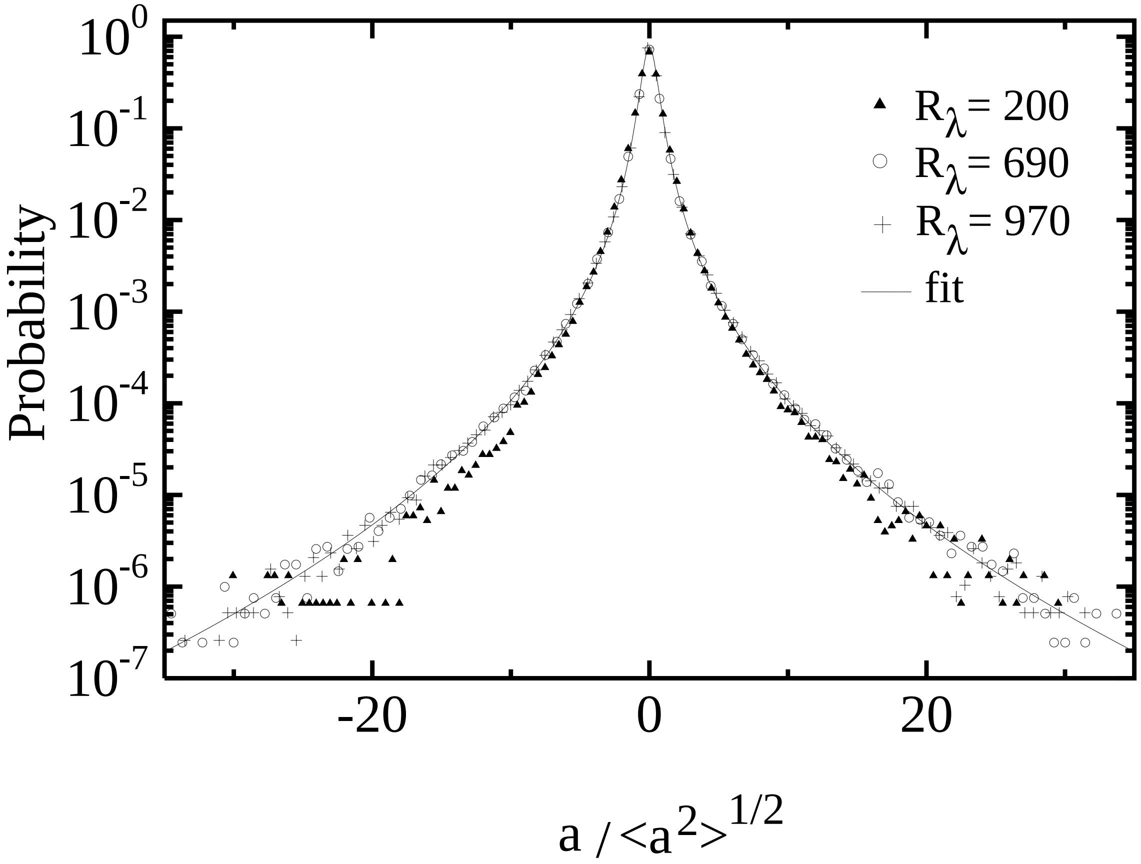

Figure 4.4: Probability distribution of a measured acceleration component. Data is for the x component from detector MH1. The solid line is a fit of Eq. 4.1 to the $R_\lambda = 690$ data.

the tails of the distributions since the fits used to sample the accelerations do not always fully resolve the rare events.

The solid line in Fig. 4.4 is a fit to the $R_\lambda = 690$ data of the function

$$P(a) = C \exp\left(\frac{-a^2}{\left(1 + |a\beta/\sigma|^\gamma\right)\sigma^2}\right), \tag{4.1}$$

with $C = 0.788$, $\beta = 0.539$, $\gamma = 1.588$, $\sigma = 0.508$. There are really only 2 free parameters in the fit since the pdf must be normalized and have unity variance. The fit was made by using a nonlinear least squares routine with 4 free parameters and then manually adjusting the fit to satisfy the constraints, while maintaining the quality of the fit. The flatness of the fitted probability distribution is 54.3.

Holzer & Siggia (1993) show that the acceleration (pressure gradient) distribution should be of the form

$$P(a) \sim \exp\left(-\left|\frac{a}{\sigma}\right|^{1/2}\right) \tag{4.2}$$

if the velocity difference distributions are exponential. The tails of the fitted distribution scale as $\exp(-|a|^{0.41})$ which is not far from this prediction. Beyond $a/\left\langle a^2\right\rangle^{1/2} = 3$ the acceleration distribution can be fit just as well by a power law times an exponential as by the stretched exponential. The fit

$$P(a) = C|a|^{-\gamma} \exp\left(-\left|\frac{a}{\sigma}\right|\right), \tag{4.3}$$

with $C = 0.221$, $\gamma = 2.80$, and $\sigma = 8.74$ is indistinguishable from the stretched exponential fit above in the range $3 < a/\left\langle a^2\right\rangle^{1/2} < 40$. We conclude that while the data does not uniquely determine the functional form of the pdf, Eq. 4.1 is a useful parameterization that reproduces the experimental results well.

Figure 4.5 shows a comparison of the experimental acceleration distributions with the results of numerical simulations by Vedula & Yeung (1999). The comparison shows good agreement in the shape of the distribution and the trend with Reynolds number. The tails of the distribution are becoming stronger as the Reynolds number increases reflecting increasing intermittency.

4.3.2 Joint distribution of different acceleration components

The different acceleration coordinates measured with different detectors are not independent. Even a visual survey of the raw data reveals that large accelerations on one detector are correlated with large accelerations on the other. One might think that this correlation would contain some interesting information about the structure of the rare events. It turns out though that this correlation is primarily a result of the shape of the probability distribution for a single component. In an isotropic distribution, it can be proven that the only way that different components can be independent is for the distribution to be an isotropic joint gaussian. For the stretched exponential observed here, the different components are highly dependent on each other.

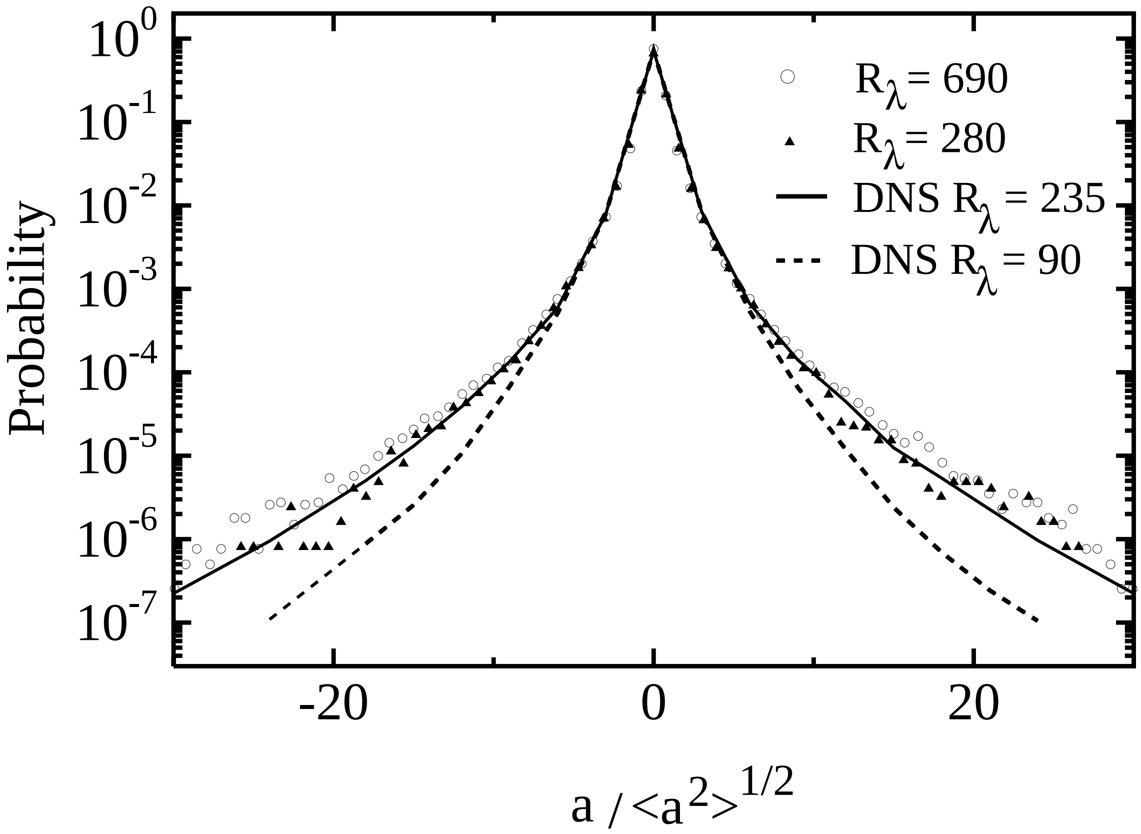

Figure 4.5: Comparison of the measured pdf with those from numerical simulations by Vedula & Yeung (1999).

If the three dimensional acceleration is isotropic, the probability distribution for an acceleration component, $f(a_1)$, and the distribution for the magnitude of the acceleration, $g(a)$, are related by the following relations (Pope, 1999):

$$f(a_1) = \frac{1}{2}\int_{|a_1|}^{\infty} \frac{g(a)}{a} da, \tag{4.4}$$

$$g(a) = -2a\,\frac{d}{da}f(a). \tag{4.5}$$

This confirms the intuitive notion that the joint distribution can be calculated directly from a single component and so there is no need for measurements of the joint distribution. The only information in the joint distribution would be anisotropic corrections. As the moments of different components are easier to measure and contain most of the anisotropy information, measurements of the joint acceleration distribution have not been pursued.

4.3.3 Three-dimensional reconstruction of large acceleration events.

A manual survey of the raw data of the large acceleration events gives a strong impression that the acceleration is quasi-periodic, as it would be for particles caught in vortex structures. To study this in more detail, we took several data sets with two detectors each measuring two coordinates. This allows all three coordinates of the trajectory to be measured, but because it uses the conjugate peaks it requires manual intervention to correctly splice and match the tracks.

Examples of the three dimensional trajectories are shown in Figs. 4.6-4.8 These events show a helical structure that is quite intriguing. It is worth noting that the largest acceleration along the track in Fig. 4.6 is 16,000 m/s^2. Color plots of these three dimensional trajectories are available on the turbulence group web pages: http://milou.msc.cornell.edu/turbulence.html.

Measurements such as those shown in Fig. 4.6 offer new possibilities for addressing questions about the structure of violent rare events and their contribution to small scale intermittency. Modeling of the detection process will be necessary to make precise statements about the fraction of the large acceleration events that have this helical structure since helical events are likely to stay in the detection volume longer than events with more linear acceleration.

4.4 Acceleration Variance Measurements

A primary concern in measuring accelerations is to determine whether the time span used in the quadratic fits is long enough to eliminate contributions from measurement error and still short enough not to average over the structure of the true trajectory. To examine this, the acceleration variance is calculated as a function of fit length. A plot of this function is shown in Fig. 4.9. Both axes have been normalized by Kolmogorov variables. The fit

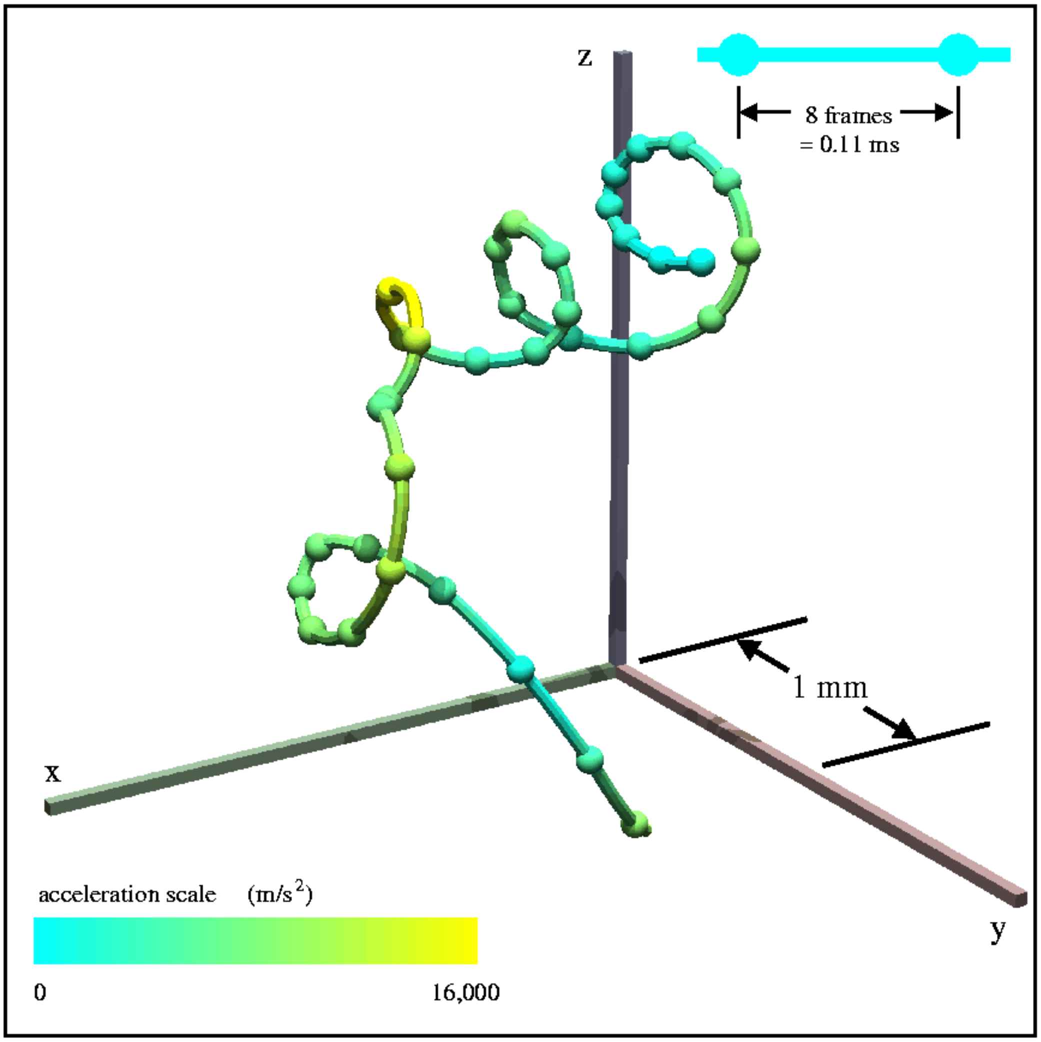

Figure 4.6: Three-dimensional time resolved trajectory showing very large acceleration. This data was taken at a disk frequency of 8 Hz which is $R_\lambda = 1030$. The Kolmogorov scales are $\eta = 16\mu\mathrm{m}$ and $\tau_\eta = 0.268$ ms. The spherical markers are equally spaced in time with 8 frames between them.

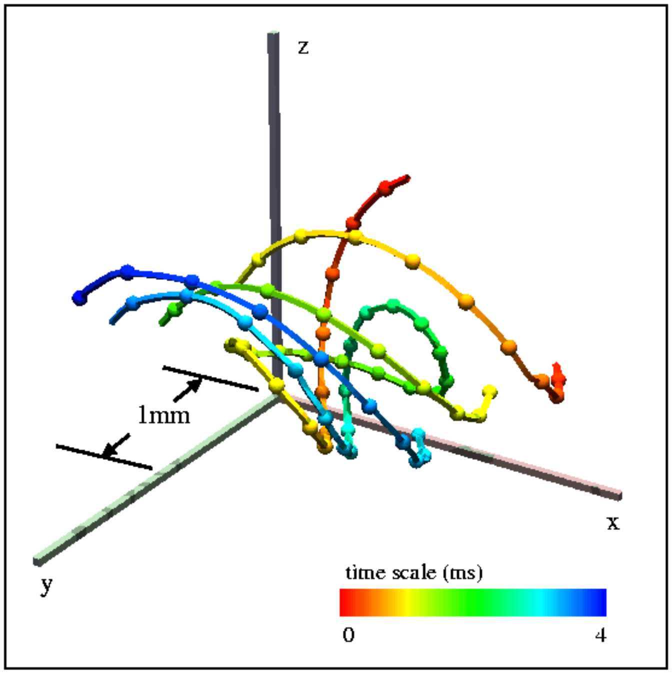

Figure 4.7: Another large acceleration event showing four particles. The grey scale labels time along the trajectory. Parameters are the same as in Fig. 4.6.

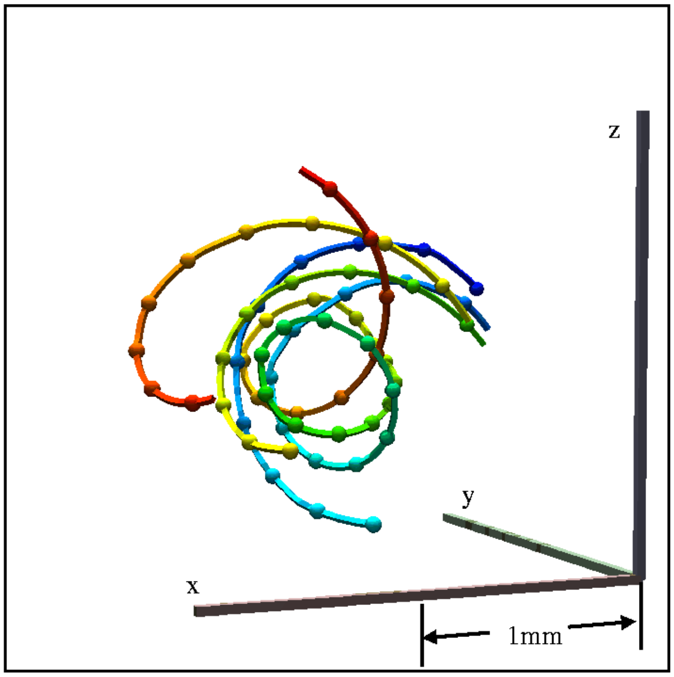

Figure 4.8: Same event as Fig 4.7 from a different angle.

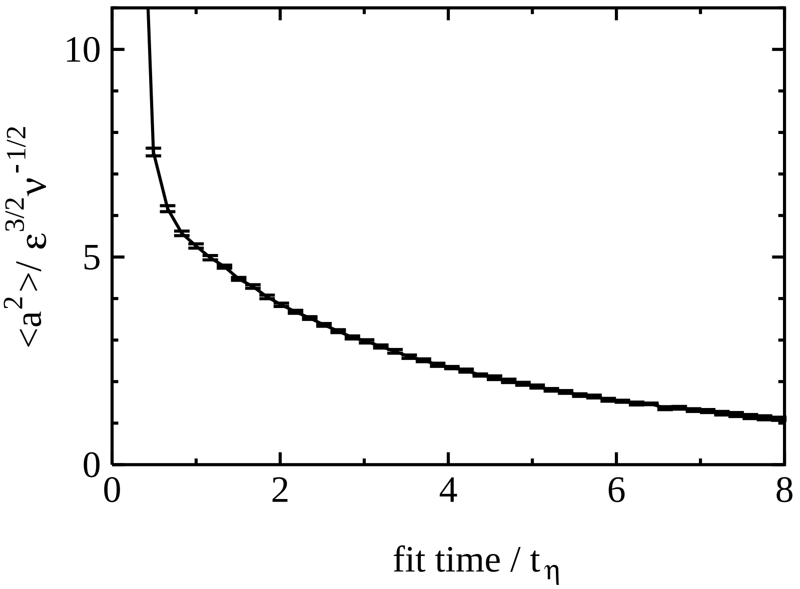

Figure 4.9: Measured acceleration variance as a function of fit time. $R_\lambda = 690$, frequency=3.5 Hz, x coordinate with MH1.

time is in units of the Kolmogorov time scale, and the acceleration variance is normalized to give the Kolmogorov constant a_0 defined by

$$a_0 = \frac{\langle a_\alpha^2 \rangle}{\epsilon^{3/2}\nu^{-1/2}}, \tag{4.6}$$

where a_α is an acceleration component and no summation over indices is implied. The measurement errors in this plot were determined by dividing the data set into six subsets and taking the standard deviation of the results from different subsets divided by the square root of six.

The sharp turn up for times less than 1 τ_η is a result of position measurement error. The slow fall off at longer times is at least partly a result of the fits averaging over the true trajectories. This identification of where position measurement error becomes important is confirmed in section 4.9.1 using two detectors measuring the same coordinate. It can be seen that there is no plateau in the fit time during which the measurement error is negligible and yet the trajectories are fully resolved.

Figures 4.10 shows log-linear plots of the acceleration variance as a function of the number of points used in the fit for several different data sets ranging from $R_\lambda = 140$ to $R_\lambda = 970$. This data is for the x acceleration measured with detector MH1. Similar plots for the y accelerations taken with detector MH4 are shown in Fig. 4.11. Naive application of the Kolmogorov hypothesis implies that these curves should all have a universal form when the Reynolds number is high enough and position measurement error is not important. This follows if the acceleration, a small scale quantity, only depends on the fit time which is on the order of the Kolmogorov time. For the higher Reynolds numbers the curves are quite similar, but the low Reynolds numbers are very different. This is partly a result of the Reynolds number not being high enough. However, an additional reason

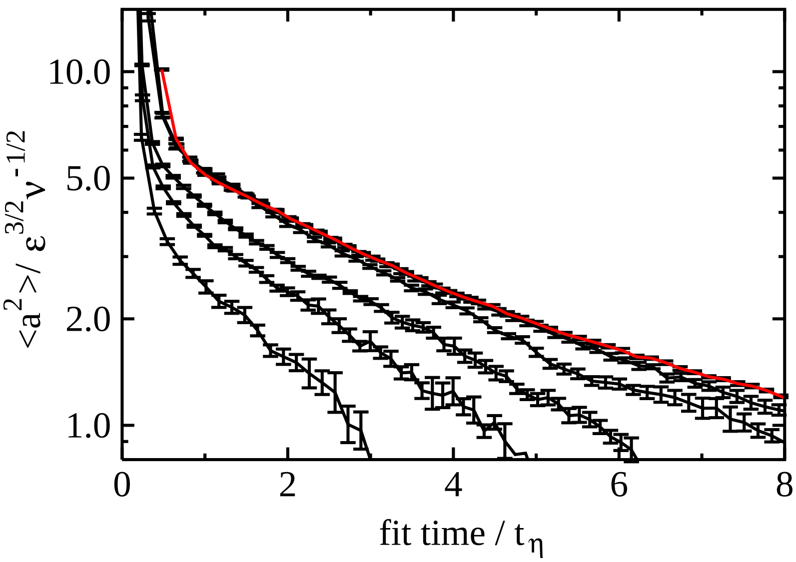

Figure 4.10: Log-linear plot of the horizontal acceleration variance as a function of fit time. The lowest Reynolds number is at the lower left. Curves move up and to the right as the Reynolds number increases. Shown are R_λ = 140, 200, 280, 490, 690, and 970. This data was taken with detector MH1.

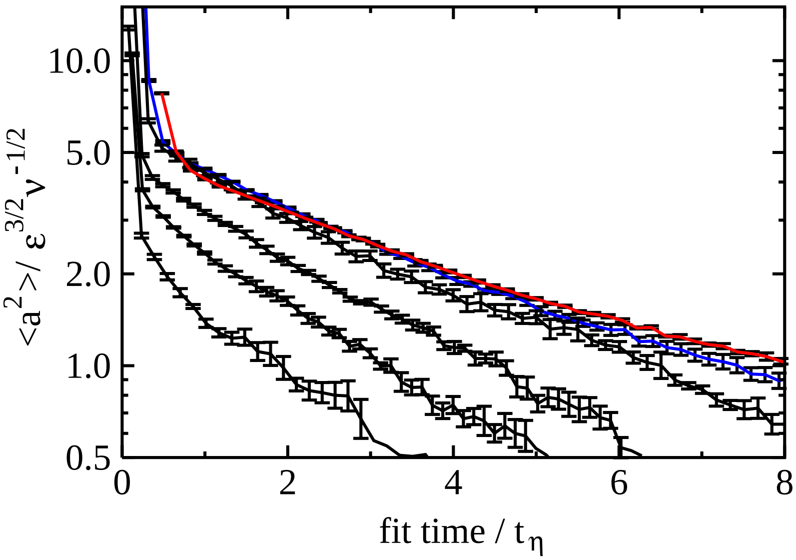

Figure 4.11: Log-linear plot of the vertical acceleration variance as a function of fit time. The lowest Reynolds number is at the lower left. Curves move up and to the right as the Reynolds number increases. Shown are R_λ = 140, 200, 280, 490, 690, and 970. This data was taken with detector MH4.

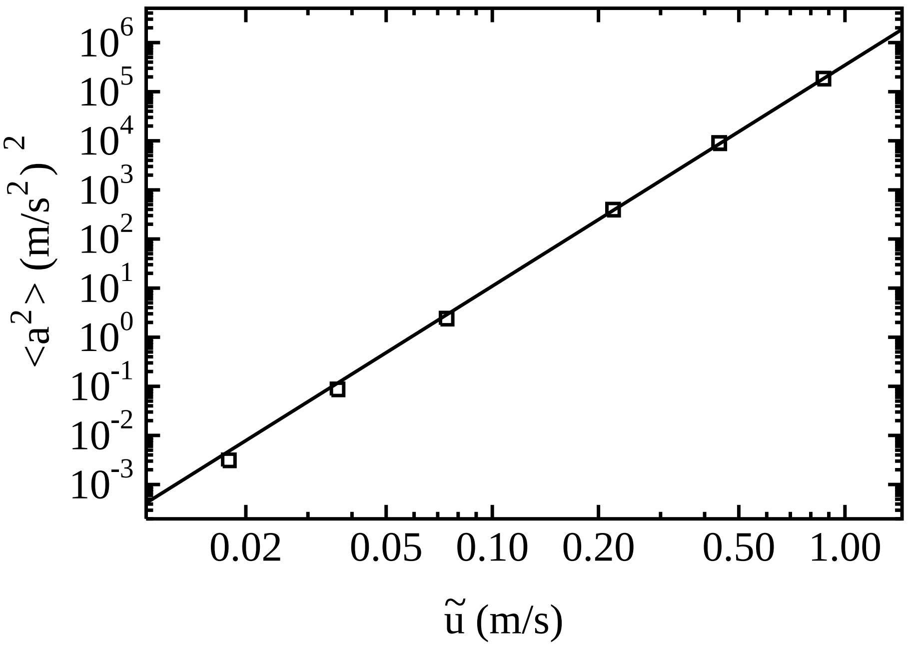

Figure 4.12: Acceleration variance for all data sets versus rms velocity, $\tilde{u}$. This is the x data from detector MH1. The solid line is the K41 prediction $\langle a^2 \rangle \sim \tilde{u}^{9/2}$.

that the Kolmogorov hypotheses do not fully apply is that this data shows a significant correlation between the time a particle is tracked and its acceleration. This is discussed in more detail in section 4.9.3, but the simple picture is that large acceleration causes large enough change in velocity to change the tracking time. This means that the ratio of the detection volume to η^3 enters as another parameter and the curves should not be universal. As discussed in section 4.9.3, this effect should go away in the limit of short fit times.

Since the curves in Figs. 4.10 and 4.11 are approximately exponential over much of the range that they are measured, we decided to use an exponential extrapolation back to zero fit time as the value of the acceleration variance. The range of fit time from 1 to 4 τ_η was used for the exponential fit. This almost certainly overestimates the true acceleration variance since this curve must have zero slope at the origin if the trajectories have a continuous third derivative. However, the amount of the extrapolation is in all cases less than 30%, and is usually 10% to 20%, so the overestimate must be less than this.

Figure 4.12 shows the extrapolated value of the acceleration variance versus the rms velocity for the x data from detector MH1. Using $\epsilon = \tilde{u}^3/L$, K41 predicts that the acceleration variance will be

$$\langle a_\alpha^2 \rangle = \frac{a_0 u^{9/2}}{L^{3/2} \nu^{1/2}} \tag{4.7}$$

Over the upper range of disk frequency, the data shows very good agreement with the K41 $u^{9/2}$ scaling over several orders of magnitude in the acceleration variance. At the lower velocities there is a small but significant deviation.

Figure 4.13 contains some of the primary results of this study. It shows the measured value of a_0, which is the acceleration variance normalized by Kolmogorov variables. Data

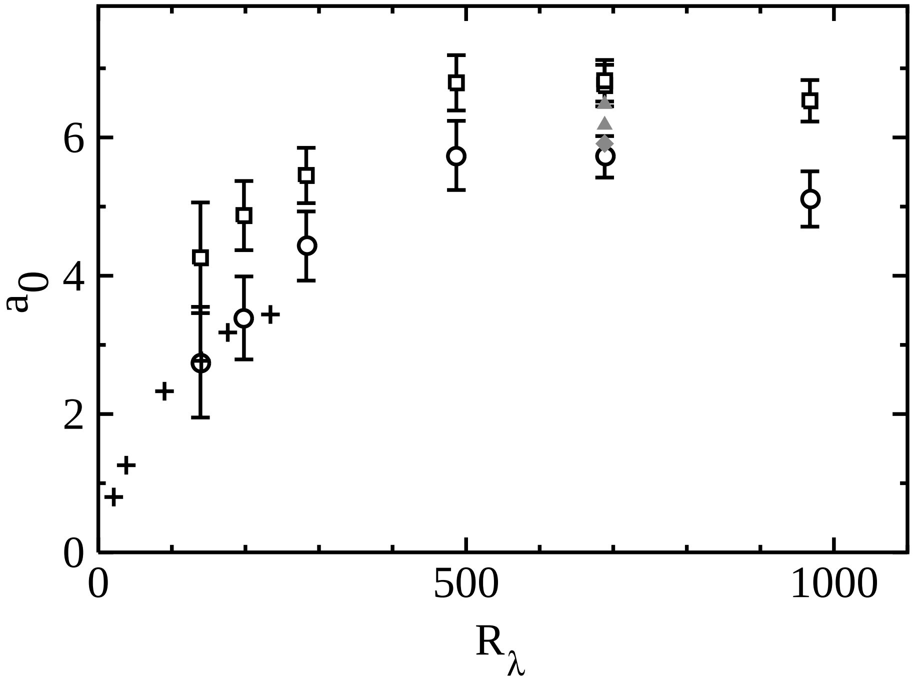

Figure 4.13: a_0 for all data sets as a function of R_λ. Squares are x data from MH1. Circles are y data from MH4. Error bars represent uncertainty in the extrapolation to zero fit time. Grey triangles are z data from MH4. Grey diamond is y data from MH1. Crosses are DNS data from Vedula & Yeung (1999).

for both the x and y acceleration are shown. At the larger Reynolds numbers, a_0 is nearly constant. At lower Reynolds numbers, it is significantly smaller. The value of a_0 where it is constant is in the range of 5 to 7. The data for the x and y accelerations show a similar trend, but the y acceleration variance is smaller by 15% to 20%.

A central question is whether this difference is caused by an anisotropy of the acceleration or whether it is affected by systematic errors. To study this, three data sets were taken at $R_\lambda = 690$ with the detectors rotated to measure different coordinates. The results for the z acceleration with detector MH4 (grey triangles) and the y acceleration with MH1 (grey diamond) are shown in Fig 4.13. (Because of the cylindrical symmetry of the flow, the x and z statistics should be identical, and we find this to be very nearly the case for velocity statistics.) The data from the rotated detectors suggests that the difference between coordinates may be smaller than the first data shows. The y data from detector MH1 is slightly although not significantly larger that the data from MH4. The z data sets from MH4 are both smaller than the x data from MH1. The z data is probably the most questionable, since the detection volume for MH4 is extremely small when it is rotated. Although some of the discrepancy is due to the detector and detection geometry, there is still a systematic difference between the two coordinates.

Figure 4.14 shows the x data from Fig. 4.13 along with estimates of the systematic errors. This displays statistical errors and the estimated limits of the important systematic errors. Statistical errors are clearly negligible. Systematic errors due to the uncertainty in the energy dissipation cause a 15% uncertainty in the high Reynolds number value of a_0. Lower limits of possible systematic errors due to extrapolation are shown. Judging from the curvature of the data in Fig. 4.10, the actual acceleration variance is likely closer to the extrapolated value than to the lower limit.

The primary conclusion we draw from this data is that while a_0 is increasing at lower Reynolds numbers, it has flattened out above $R_\lambda = 400$. This measurement of the turn over from a_0 increasing with R_λ at small R_λ number to nearly constant at large R_λ is fairly convincing evidence that at large Reynolds numbers a_0 scales more like the K41 prediction than the $R_\lambda^{1/2}$ seen in the simulations (Vedula & Yeung, 1999). More modest intermittency corrections may still exist.

Another conclusion is that the anisotropic structure of our flow between counter-rotating disks seems to have significant effect on the acceleration variance out to $R_\lambda = 970$. Even where the value of a_0 is not changing with Reynolds number, the different coordinates are significantly different. This could draw into question the previous conclusion since it is possible that a peculiarity of the large scale structure of this flow results in the constant value of a_0 that we see, and different flows would be different. As noted by Nelkin & Chen (1999), the longitudinal velocity derivative flatness in a flow between counter-rotating disks has been observed to have a plateau in this same range of Reynolds numbers (Belin et al, 1997; Sreenivasan & Antonia, 1997). The deviation between the two coordinates is small enough compared to the deviation from the $R_\lambda^{1/2}$ scaling that it seems unlikely that the existence of the plateau is caused by the large scale structure of the flow, but only measurements in other flows can confirm this. It is quite possible that smaller intermittency corrections such as those described in sections 2.2 and 2.3 could be affected by the flow structure.

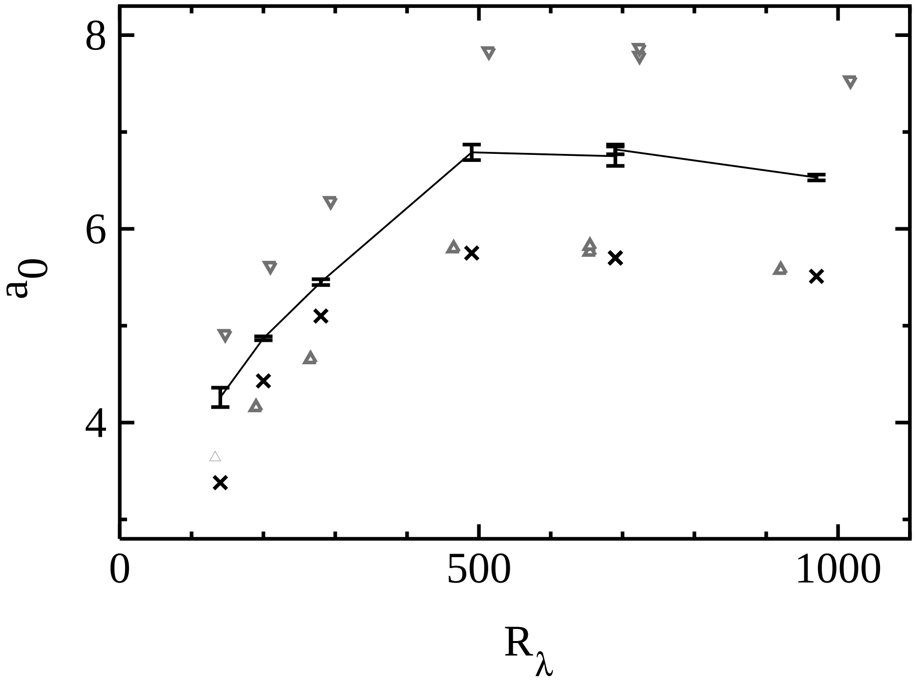

Figure 4.14: Systematic and statistical errors in a_0 for for the x data from MH1 as a function of R_λ. Points connected by the solid line are the same data as Fig. 4.13. The error bars on these points are the measured statistical error in the acceleration variance at $1\tau_\eta$. These are the uncertainties shown in Fig. 4.10 at a fit time of $1\tau_\eta$. $\times$ labels the value of the acceleration variance at the shortest fit time which had negligible contribution from position measurement errors. This gives the lower limit on the possible systematic error due to extrapolation. Grey triangles represent the values of a_0 and R_λ that result from using values of ϵ at either end of its 10% uncertainty.

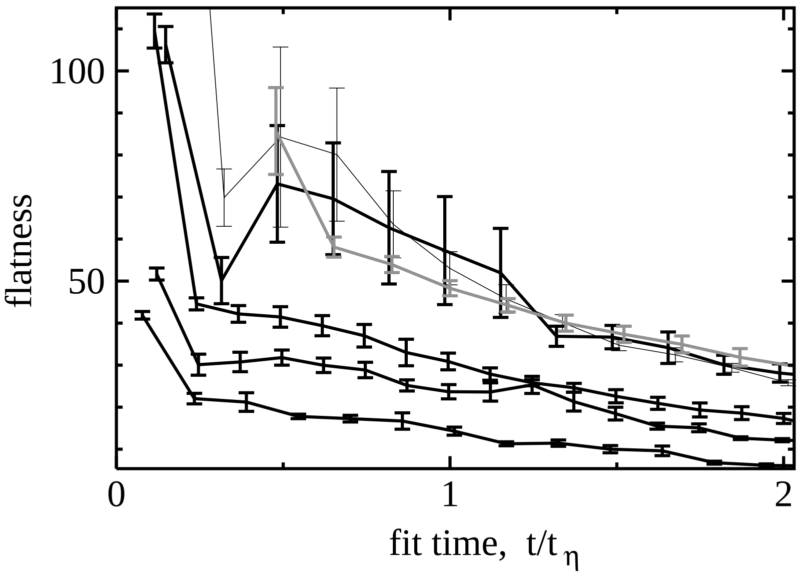

Figure 4.15: Acceleration flatness as a function of the fit time. All sets are x acceleration from MH1. Lower three curves are R_λ = 140, 200, and 280, and increase with increasing Reynolds number. Solid thick upper curve is R_λ = 490. Solid thin curve is R_λ = 690. Grey thick curve is R_λ = 970.

4.5 Acceleration Flatness Measurements

The probability distributions of acceleration shown in Fig. 4.4 suggest that studying the change in flatness with Reynolds number would be an effective way to characterize the intermittency in the flow. The measured flatness for several Reynolds numbers is shown as a function of the fit time in Fig. 4.15. In the low Reynolds number range, there is a trend toward higher flatness as the Reynolds number increases. Here the problem of no plateau as a function of fit length is even more severe than for the variance, so no attempt is made to extrapolate to identify the true value of the flatness. Fig. 4.16 shows the flatness for all data sets measured with fits over 1 τ_η. The flatness increases with R_λ at low R_λ, but the measurements at larger R_λ are not reliable enough for conclusions to be drawn. In addition to the fit time problem, the particle size has not been shown to be sufficiently small to accurately measure the rare violent events that dominate the flatness.

The main conclusion we draw here is that the flatness factors are very large. For the larger R_λ the true flatness must be greater than 50, which is considerably larger than the flatness of any other small scale statistics at these Reynolds numbers. This may partially explain the anisotropy of the acceleration variance observed in the previous section. The small scale quantity with the next largest flatness is the passive scalar, which is found to be anisotropic even at very large Reynolds numbers Warhaft (2000).

Statistical convergence is a major problem for distributions with flatness of order 50. An exploration I made to clarify some of the issues of convergence is described in Appendix B. Figure 4.17 shows the probability distribution multiplied by a^4 for the $R_\lambda = 690$ data set and for the stretched exponential fit. The area under these curves gives

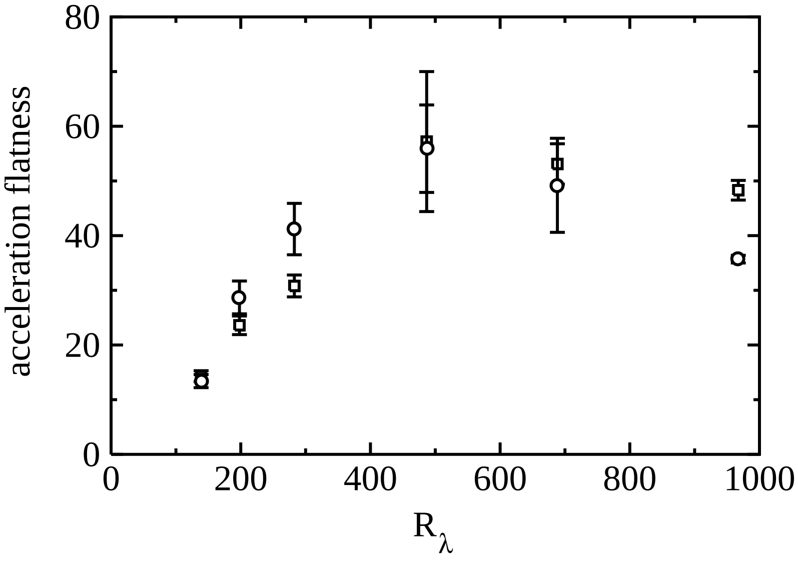

Figure 4.16: Acceleration flatness as a function of Reynolds number. Squares are x data from MH1, circles are y data from MH4. Error bars show the statistical errors determined from deviation between subsets. Since all data sets are sampled at a fit time of $1\tau_\eta$, this data must be interpreted with caution.

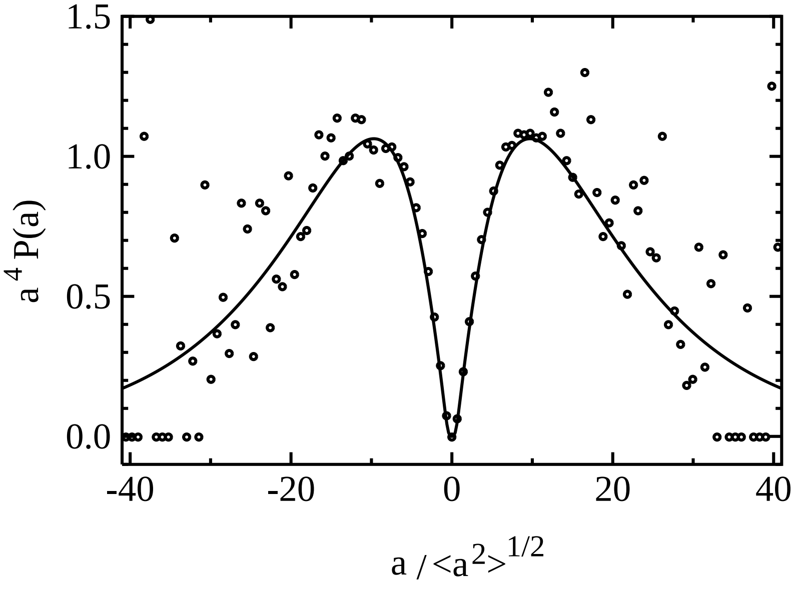

Figure 4.17: Acceleration probability distribution multiplied by a^4 to show which events are contributing to the acceleration flatness. The circles are the $R_\lambda = 690$ data shown in Fig. 4.4. The solid line is the fit in Eq. 4.1.

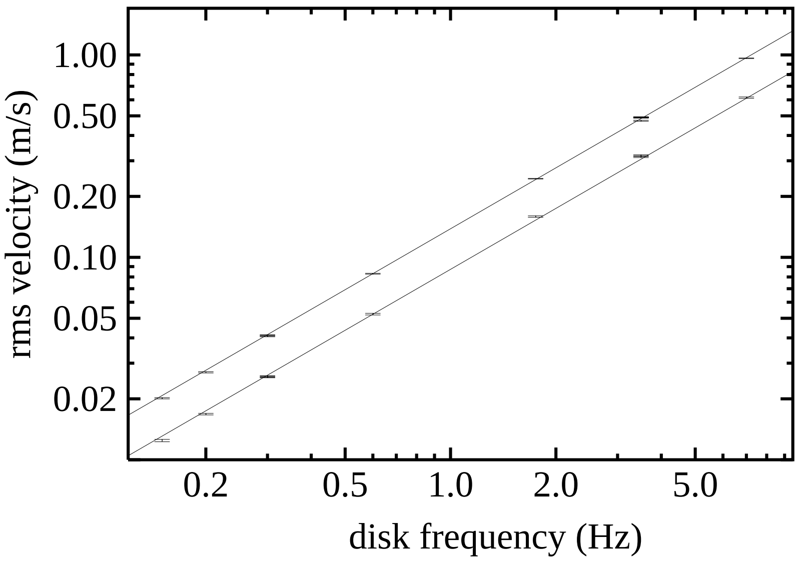

Figure 4.18: RMS velocity vs disk frequency. Each point has error bars representing the random error. The upper data is the horizontal, x, coordinate and the lower data is the vertical y, coordinate. Linear fits to each data set are shown.

the fourth moment, and the scatter is often used to determine the level of convergence of the moment. I find though that the only way to accurately estimate convergence is to divide the sample into subsets and look at the deviations between subsets, which is how the errors in Fig. 4.15 were determined. I can greatly increase the smoothness of the pdf and hence improve the appearance of Fig. 4.17 by decreasing the spacing between samples along the tracks. The error bars in Fig. 4.15 show no significant change though because the new samples are highly correlated.

4.6 Velocity Measurements

Accurate measurements of the velocity distribution in the flow are important for determining the Reynolds number and normalizing various quantities. They also allow insights into the level of anisotropy of the large scales. Measurements of the rms velocity as a function of disk frequency are shown in the log-log plot in Fig. 4.18. Linear fits are shown with $\langle u_x^2\rangle^{1/2} = 0.1386f$ and $\langle u_y^2\rangle^{1/2} = 0.0872f$ which match the data very well. These fits imply $\tilde{u} = (\langle u_i u_i\rangle/3)^{1/2} = 0.1238f$. This scaling was seen in the earlier measurements with the position sensitive photodiode, but the constants measured then were $\langle u_x^2\rangle^{1/2} = 0.1233f$ and $\langle u_y^2\rangle^{1/2} = 0.0829f$, and $\tilde{u} = 0.1115f$. This discrepancy is not fully explained. The most natural explanation would be that the larger particles in the earlier experiments gave smaller velocities, but the data for large tracer particles taken with the strip detector do not show this effect.

Figure 4.19 shows the RMS velocity divided by the linear fit in order to clearly show deviations from the fit. Deviations of up to 5% are visible. These may be real deviations

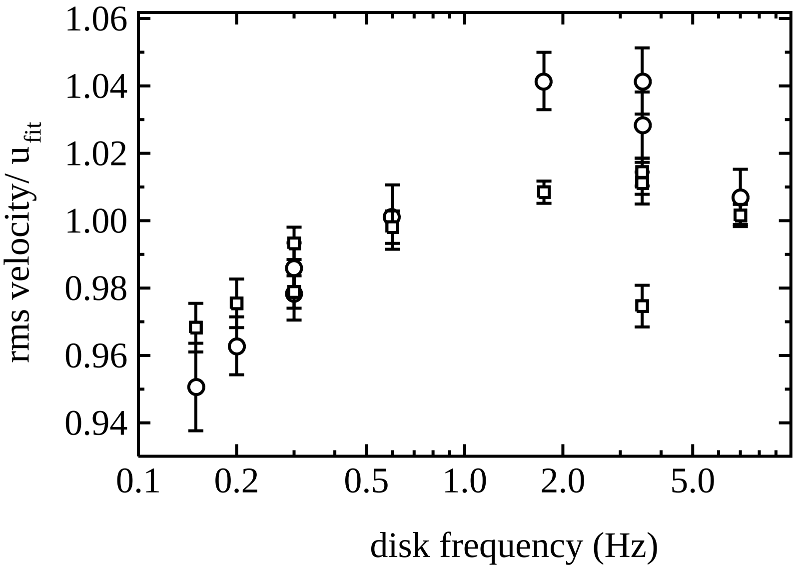

Figure 4.19: RMS velocity divided by the linear fit as a function of disk frequency. Squares are u_x, circles are u_y.

from the linear model, but as discussed in section 4.9.2 there are probably systematic errors in the velocity measurements that are of this order.

Linear and logarithmic plots of the velocity probability distribution are shown in Fig. 4.20. The dip in the center of the velocity distribution is concerning. It is most pronounced on detector MH4 and at large disk frequencies. As will be discussed in more detail in section 4.9.2, it appears to be caused by sample biases from the ac coupling of the detectors and from tracks disappearing behind dead pixels.

The logarithmic plot of the probability distribution in Fig. 4.20, and measurements of the flatness of the velocity distribution shown in Fig. 4.21 reveal an interesting effect. The flatness of both the x and y components are independent of disk frequency and significantly different than the gaussian value of 3, with flatness of u_x equal to 2.75 and flatness of u_y equal to 3.35. The results are unchanged when the detectors are rotated as shown by the multiple points at frequency of 3.5. Velocity distributions far from the walls of turbulent flows are usually nearly gaussian. Slightly subgaussian tails on velocity distributions have been observed by Noullez et al (1997) in a jet flow and Jimenez et al (1993) in a homogeneous numerical simulation. Both groups report velocity flatness of 2.80. One would expect that the velocity flatness depends on the details of the large scales of the flow. In our flow, the flatness of the component with the smaller rms is larger than gaussian and the flatness of the component with the larger rms is subgaussian. The orientation of the mean strain could also be a factor.

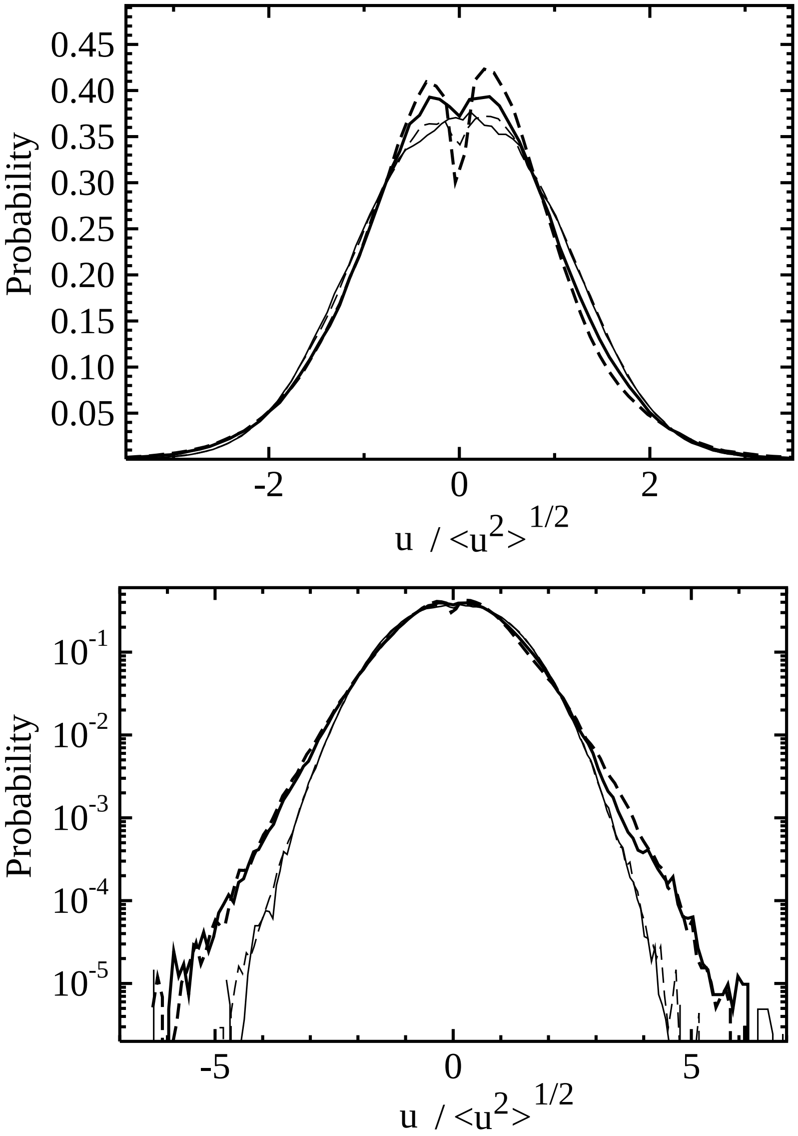

Figure 4.20: PDF of velocity. Thick dashed line is u_y from 7 Hz MH4 data, thin dashed line is u_x from 0.6 Hz MH4 data. Thick solid line is u_y from 7 Hz MH1 data. Thin solid line is u_x from 0.6 Hz MH1 data.

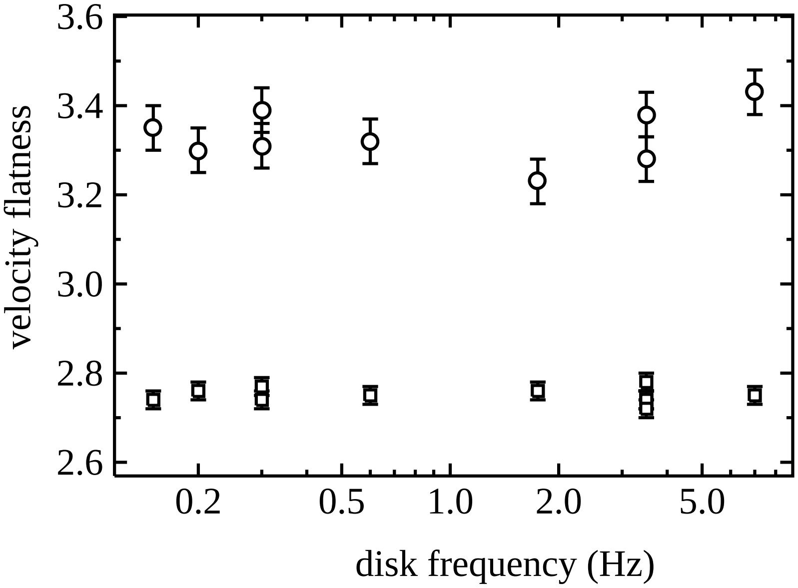

Figure 4.21: Velocity flatness vs disk frequency.

4.7 Dissipation Measurements

The energy dissipation was determined by measurement of the transverse second order velocity structure function, defined by

$$D_{NN}(r) = \langle (u_{\perp 1} - u_{\perp 2})^2 \rangle, \tag{4.8}$$

where r is the separation distance of two particles and $u_{\perp 1}$ and $u_{\perp 2}$ are the velocity components perpendicular to the separation vector. In the inertial subrange, K41 theory predicts $D_{NN}(r) = \frac{4}{3} C_2 (\epsilon r)^{2/3}$, where C_2 is a universal constant. Many measurements have found this to be an accurate description and the constant C_2 to be equal to 2.13 (Sreenivasan, 1995). Measurement of $D_{NN}(r)$ requires transverse velocity differences to be measured for pairs of particles as a function of 3D particle separation distance.

In order to measure particle separations in the inertial subrange the detector was reconfigured to have a field of view of 30 mm × 15 mm. The flow was illuminated by a thin light sheet 15 mm high and 0.1 mm deep, incident on the detection volume at $45°$ with respect to the optical axis of the detector. The flow was seeded with a high density of 46 μm particles. These measurements were performed when only one detector was available, and so x positions were determined from positive primary peaks and y positions were determined from negative conjugate peaks of a p-z detector. An example of a sequence of the raw data is in Fig. 4.22. Once x and y coordinate trajectories were identified, the coordinate matching was performed by searching for x–y trajectory pairs with maximum temporal correlation of the intensity. Correlation thresholds were imposed to exclude ambiguous trajectories.

Using the constraint that particles must lie in the light sheet to be visible, the 3D particle coordinates were determined from the 2D position measurements, allowing particle separations to be measured over the range 1–30 mm. The particle trajectories were

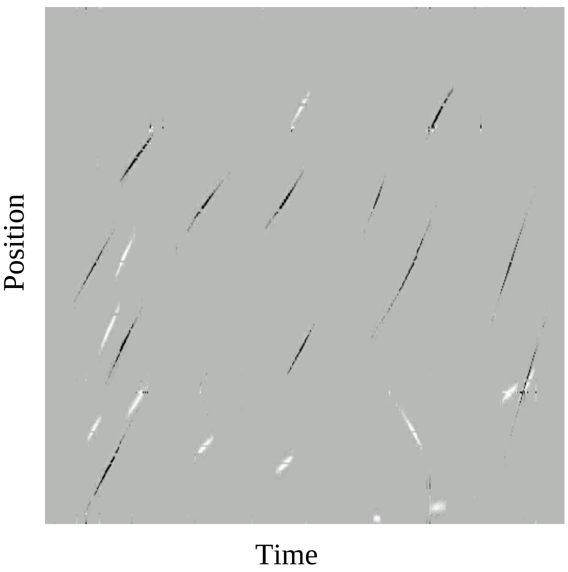

Figure 4.22: Raw data used for the dissipation measurements.

also used to measure the projection of the velocity vectors on the detector image plane. Despite the fact that the velocity differences and particle separations are measured in different planes, a transverse velocity component can be measured for any visible particle separation. Because of the shape of the detection volume, this measurement is statistically weighted towards vertical velocity differences for horizontally displaced particles.

The structure functions which were measured for disk frequency of 5 Hz and 2.5 Hz are shown in Fig. 4.23. They exhibit an $r^{2/3}$ scaling region of about 1–10 mm for the 5 Hz data and 2–10 mm for the 2.5 Hz data. The scaling region is limited at large r by the integral length scale, and at small r by velocity uncertainty and particle localization in the light sheet. When the structure functions were fit to the function αr^{β} it was found that $\beta = 0.66 \pm 0.04$. However, the energy dissipation was determined using fixed $\beta = 2/3$. The dependence of ϵ on the rms velocity is found to be consistent with relation $\epsilon = \tilde{u}^3/L$, and gives an effective integral scale of $L = 71 \pm 7$ mm.

4.8 Acceleration of finite size spheres in turbulence

To measure how accurately the tracer particles represent the accelerations of fluid particles, we performed a series of runs with different sphere sizes and different fluid densities.

As discussed in Chapter 2, a large amount of work has been done on the motion of particles in turbulence when the particle diameter is much smaller than the smallest scales of the flow. In this limit, there can be no difference between the fluid velocity and the particle velocity unless their densities are different. When the densities are different, a rich variety of effects are observed which are the subject of ongoing research (Kim et al, 1998). However, we find that we are operating in a regime very far from the small particle limit which is traditionally studied. Our measurements show that the small density

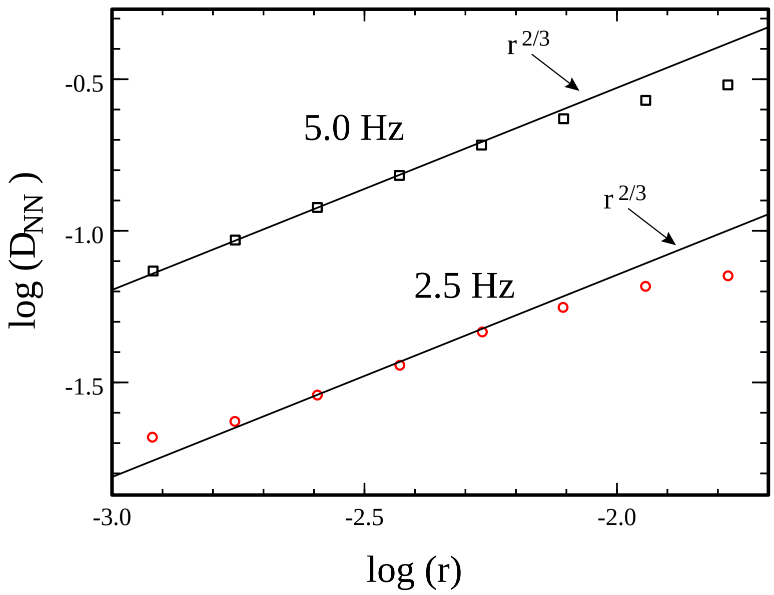

Figure 4.23: Transverse structure functions and the fits used to determine the energy dissipation.

difference between the polystyrene particles and the water produces a negligible effect on particle accelerations relative to the effect of particle size. Roughly, this can be thought of as a regime where the particle averages over the spatial structure of the acceleration field rather than the regime where a particle responds to a uniform acceleration field with different acceleration than the fluid. Theoretically, this is a much more difficult regime to analyze. Developing a phenomenological understanding of particle motion in this regime is important both as an interesting problem in its own right and as a step toward optimizing Lagrangian particle tracking experiments.

The measurements presented throughout this chapter so far have been from $46 \pm 7\ \mu\mathrm{m}$ polystyrene spheres of density 1.05 $\mathrm{g/cm^3}$. To study the particle size effects, we also made measurements of accelerations of polystyrene spheres with diameter $24 \pm 3\ \mu\mathrm{m}$, $136 \pm 14\ \mu\mathrm{m}$, and $467 \pm 18\ \mu\mathrm{m}$. All spheres were purchased from Duke Scientific. The smaller spheres were purchased with the given diameter and standard deviation. The $467\ \mu\mathrm{m}$ spheres were from a 425 to 500 $\mu\mathrm{m}$ sieve cut from a batch with wider size distribution. The 25 $\mu\mathrm{m}$ diameter measurements required decreasing the illumination volume in order to obtain sufficient light. All the data for the particle size studies were acquired at disk frequency of 7.0 Hz, which has $R_\lambda = 970$ and $\eta = 18\mu\mathrm{m}$.

The acceleration variance from these measurements is shown in Fig 4.24. A 70% change in the measured acceleration variance is observed between the small particles and the 467 $\mu\mathrm{m}$ particles. However, the trend shows that the 46 $\mu\mathrm{m}$ particles have an acceleration variance that is within the measurement error of the zero size limit. If a simple straight line fit is made, the value of the acceleration variance for 46 $\mu\mathrm{m}$ particles is within 10% of the zero size limit.

It should be noted that there are different ways to define the sample over which to

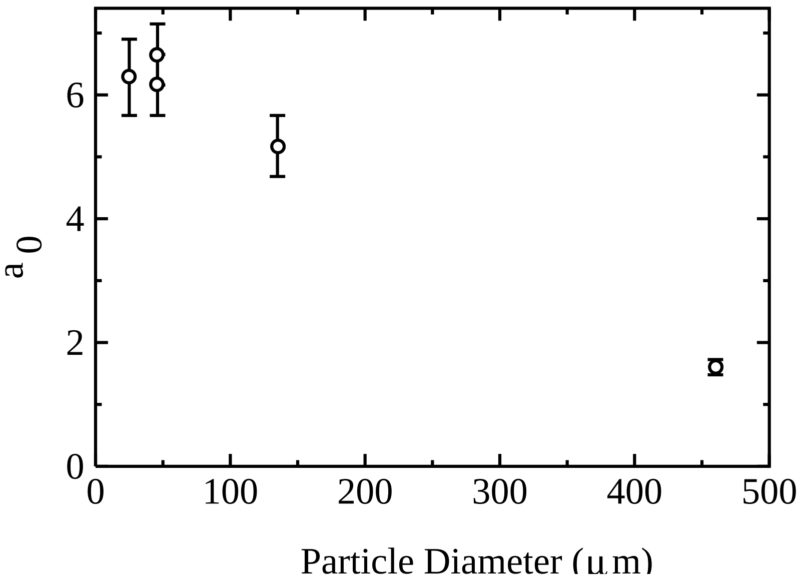

Figure 4.24: Normalized acceleration variance as a function of tracer particle diameter.

measure the acceleration variance when the particles are not fully following the flow. Our measurements are taken over all particles that enter the detection volume. This provides the actual acceleration distribution of the particles in the flow, but it is different from the distribution of accelerations of particles uniformly distributed in the flow. This is because their relative motion with the fluid can cause particles to collect or be repelled from certain structures in the flow.

The effect of density difference was explored by changing the density of the water by adding sodium chloride. These measurements were made with 467 $\mu\mathrm{m}$ particles. The procedure was to take a set of acceleration measurements, then drain 200 mL of fluid into a volumetric flask which was weighted to measure the density. The viscosity of each solution was also measured with a Cannon-Fenske viscometer. The density was then increased by adding high purity NaCl to the flow and the process repeated. The range of density was 0.997 $\mathrm{g/cm^3}$ to 1.102 $\mathrm{g/cm^3}$ which corresponds to the NaCl concentration ranging from 0% to 14% by weight. Higher concentrations were not used since this already required about 14 kg of pure salt and visible corrosion was beginning at weak places in the anodized aluminum of the apparatus. At each different salt concentration, the optical system was adjusted slightly to maintain focusing when the index of refraction of the water changed. The magnification changes this caused were calculated and corrected even though they were small (1.2%). Because of the viscosity change, the Reynolds number changes slightly as salt is added. The viscosity increased by 20% over the range studied, which results in a 10% change in R_λ.

Figure 4.25 shows the normalized acceleration variance of 467 $\mu\mathrm{m}$ polystyrene spheres as the fluid density was varied so that the tracer particles went from 5% below neutrally buoyant to 5% above neutrally buoyant. As expected, there is a trend toward higher acceleration variance when the particles are less dense than the fluid. However, the primary information in this data is that the total change in normalized acceleration across this

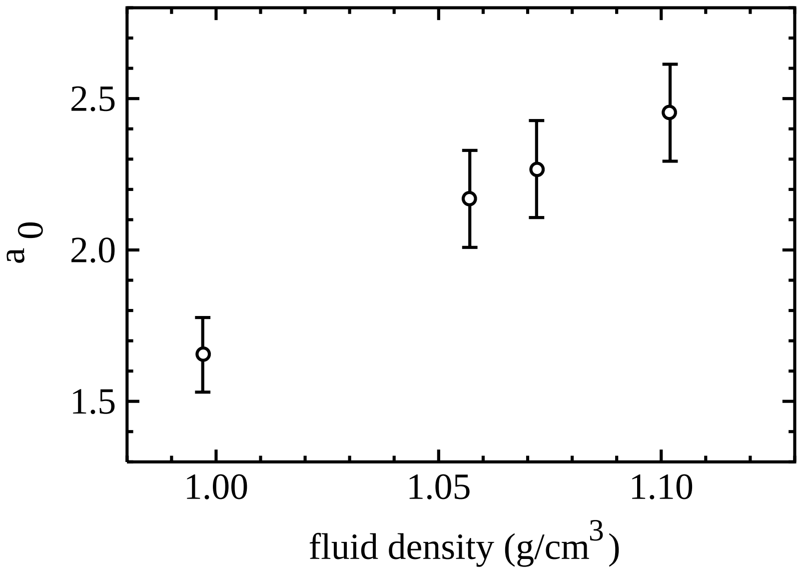

Figure 4.25: Normalized acceleration variance for 467 $\mu\mathrm{m}$ polystyrene spheres as a function of fluid density. The density of the particles is $1.05 \pm 0.01 \mathrm{g/cm}^3$.

range of density is 0.8 which is only 12% of the value of 6.5 which is measured for small particles. If smaller particles were used, the change in acceleration due to this density change should be even smaller.

We conclude that the density difference between the fluid and the particles does not have a large effect on the data in Fig. 4.24. Thus we expect that in this density range, the only important parameter in determining how small particles need to be to accurately reproduce the acceleration of fluid particles is the ratio of the particle size to the Kolmogorov length. Fig. 4.24 shows that the 46 $\mu\mathrm{m}$ particles are small enough for acceleration variance measurements.

Fig. 4.26 shows the probability distribution of the acceleration for different particle sizes and fluid densities. Fig. 4.26A is the raw distributions, and Fig. 4.26B has the horizontal axis normalized by the measured standard deviation. Figure 4.26A shows the differences in the variance which were seen earlier in Fig. 4.24. Fig. 4.26B reveals the somewhat surprising result that the shape of the probability distribution is not strongly affected by particle size. There is a slight tendency for the distributions for larger particles to have weaker tails but it is not a large effect. The distributions for the larger particles are only resolved out to about 10 standard deviations, compared with the more than 20 standard deviations resolved in Fig. 4.4. It would be interesting to take much more data with the larger particles to determine whether particle size affects the shape of the distribution far out in the tails.

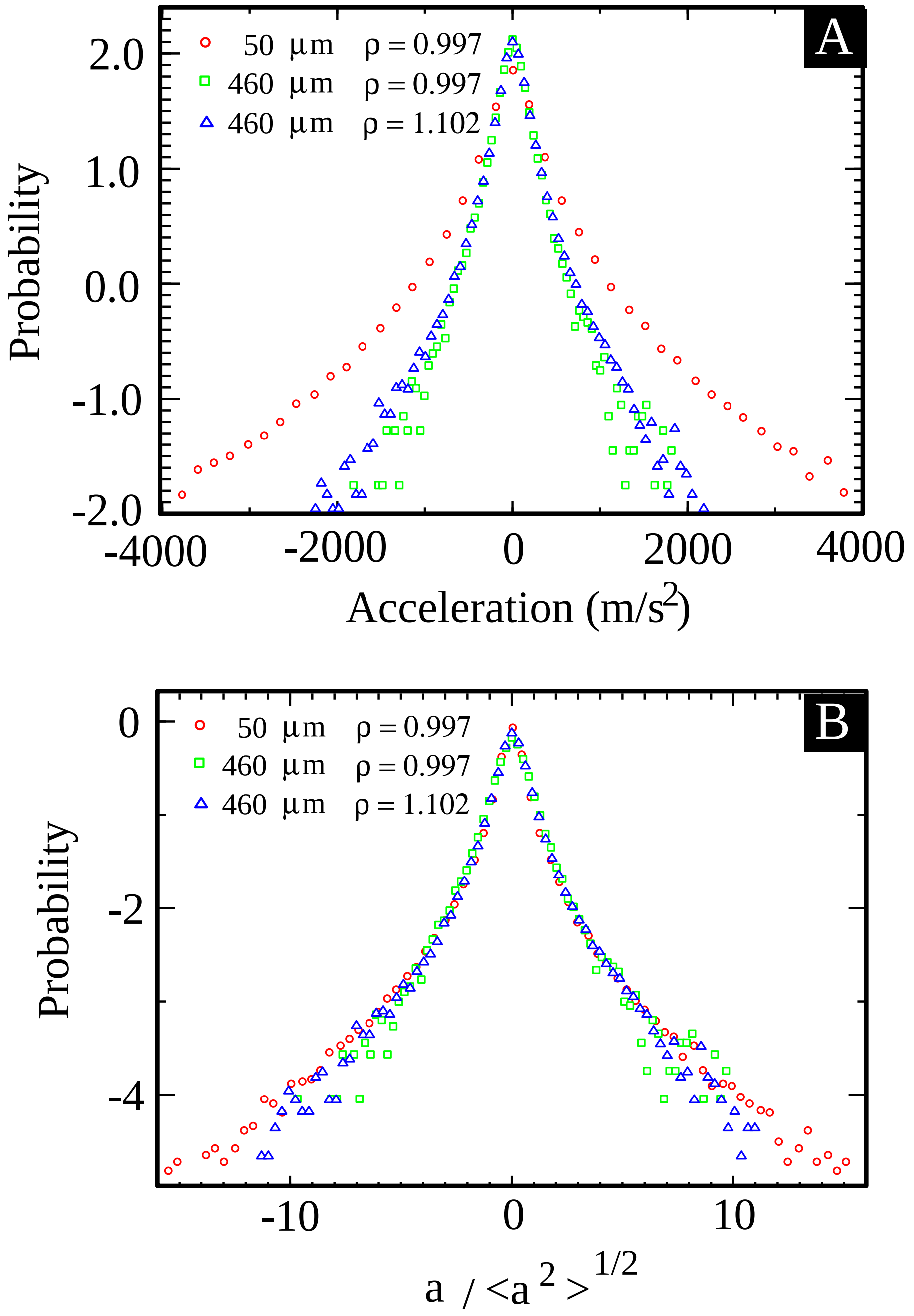

Figure 4.26: Probability distribution of the acceleration for different particle size and fluid density. A) Raw probability distributions, B) same distributions with acceration normalized by the measured rms acceleration. All data sets are taken at disk frequency of 7.0 Hz, which is $R_\lambda = 970$.

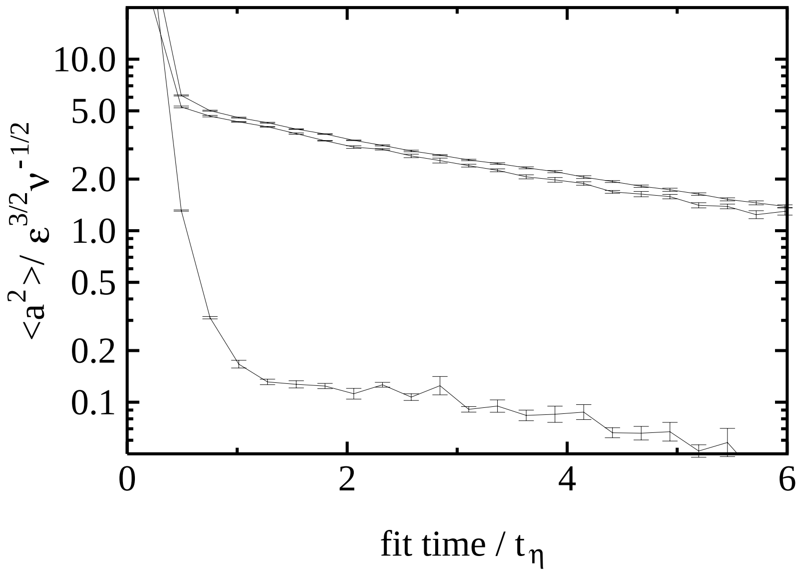

Figure 4.27: Normalized variance of the acceleration and difference in the measured acceleration between two different detectors as a function of the time span of the fit. Both detectors are measuring the y coordinate of the same trajectories. The disk frequency for this run is 3.5 Hz which is R_λ = 690.

4.9 Measurement Errors

4.9.1 Effect of position measurement errors

In interpreting the acceleration measurements from the strip detector, it has been essential to clarify what effect position measurement error has on the data in Fig. 4.9. The first check we performed was to decrease the frame rate. This resulted in the sharp turn up below 1 τ_η moving to the right but the rest of the curve remaining unchanged. This led us to believe that the position measurement error did not have significant contribution to the part of the curve above 1 τ_η.

When two detectors became available we made a more sensitive test by comparing the accelerations measured by different detectors on different optical axes. In this setup, both detectors measured the vertical coordinate of the trajectory. Figure 4.27 shows a plot of the acceleration variance versus the time span of the fit. The upper two curves show the acceleration variance from each of the two detectors. The lower curve shows the variance of the difference between the acceleration measured from different detectors. This confirms the interpretation that beyond 1 τ_η the measured variance is dominated by actual accelerations of the turbulence.

To estimate the signal to noise of the acceleration measurements, I assume that the measurement errors of the two detectors are identical, independent, and gaussian distributed. Then the rms measurement error of one detector is the rms of the difference divided by $\sqrt{2}$. At 1 τ_η the ratio of the standard deviation of the measured acceleration to the measurement error on one detector is 7.3.

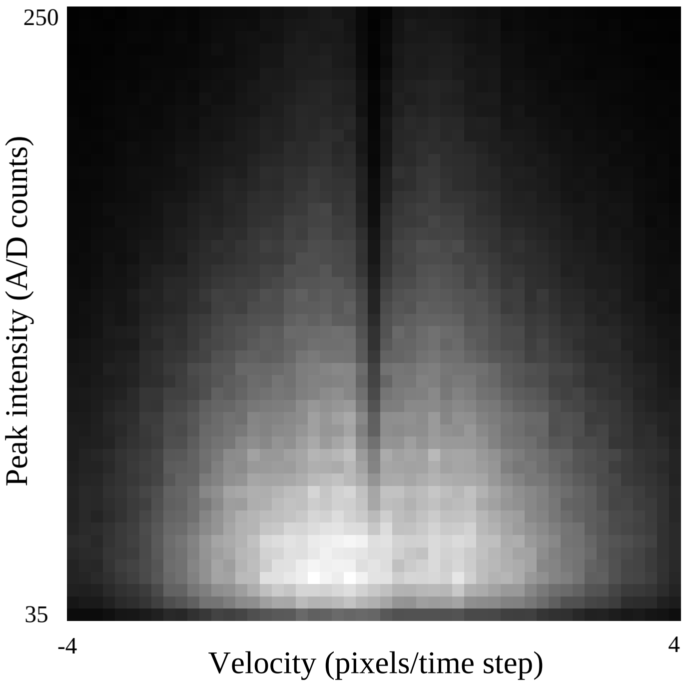

Figure 4.28: Joint probability distribution of the peak intensity of the trajectory and velocity. Greyscale is probability with white designating maximum probability. This is from the R_λ = 970 data set for y data from detector MH4.

4.9.2 Velocity sample bias

There are several ways in which velocity sample bias can occur in the strip detector data. If the detectors measure the velocity of all particles for the full time they are in the detection volume, then residence time weighting yields an unbiased velocity sample. Any trajectories whose velocities are not measured while they are in the detection volume can produce a sample bias unless the drop outs are uncorrelated with velocity.

The velocity distributions for large disk frequencies that are shown in Fig. 4.20 show a dip in the center that is unexpected. The primary cause of this has been identified as a sample bias caused by the ac coupling of the amplifiers connected to the strips of the strip detector. Evidence of this is seen in Fig. 4.28. This plot show the joint probability distribution of the intensity of the trajectory and its velocity. When a trajectory has nearly zero velocity, it remains on the same strip for many clock cycles. The ac coupling capacitor then slowly drifts to the mean of the signal. The measured intensity is then decreased by the difference between the mean and the instantaneous current from the detector. This causes zero velocity events to be less likely to be detected, and results in the dip in the probability distribution.

Another way in which the measured signal from the strip detector can depend on the velocity is if the particle moves significantly during the illumination pulse. At the large disk frequencies where this is a problem, the illumination pulse is on for 5.0 μs out of the 14.3 μs frame readout period. If the light spot is only allowed to move 2 pixels during

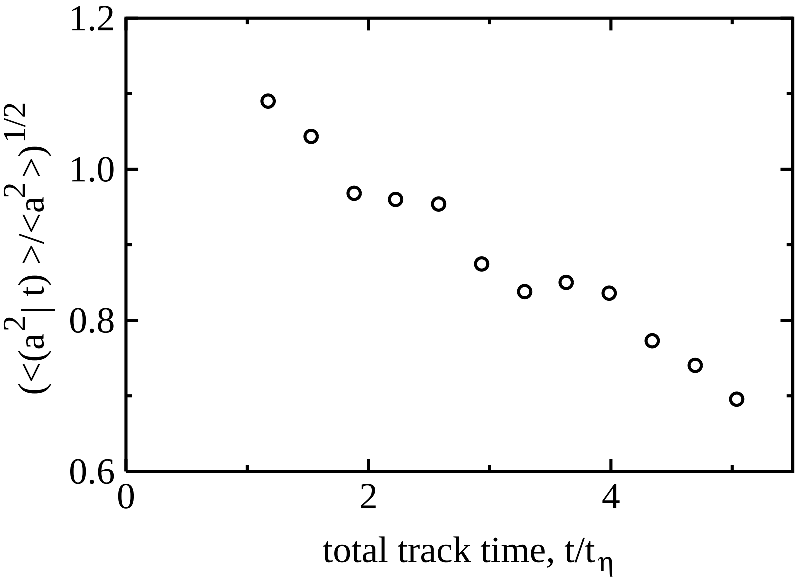

Figure 4.29: Standard deviation of the acceleration conditional on the total time the track was in view.

the illumination time, the velocity must be kept below 5.7 pixels per time step. The rms velocity in all the runs reported here was less than 2.3 pixels per time step, but in data set with highest rms velocity there were samples out to 6 pixels per time step. I have not found a way to unambiguously determine the importance of this effect, but it may be the reason the data set with the highest velocity in pixels per time step is slightly different than the others. (This is the y data at 7 Hz, $R_\lambda = 970$, taken with detector MH4).

Care must be taken in sampling trajectories that cross over dead pixels in order to avoid sample bias. Our first analysis approach was simply not using samples when the trajectory was on a dead pixel. This produced a significant bias, which was evident in holes on the sides of the velocity distributions. These resulted from the correlation between the time the trajectory took to cross a dead pixel and its velocity. This problem was mostly solved by interpolating the velocity to ensure sampling even when the trajectory disappeared on a dead pixel. The effect of dead pixels at the beginning and end of trajectories still can not be corrected, but this is a much smaller effect. There may also be a contribution to the dip at zero velocity from the fact that zero velocity tracks will not be as likely to be spliced back together when they cross dead pixels, and thus can not be interpolated.

4.9.3 Acceleration sample bias

This is a subject which our group is still working to understand, but I will present the clues we have at this point. The data shown in Figs. 4.10 and 4.11 suggests that there is a significant dependence of the residence time of a track on its acceleration, particularly for low Reynolds numbers. Figure 4.29 provides a confirmation of this dependence by showing the rms acceleration conditional on the total time of the track. In the ideal situ-

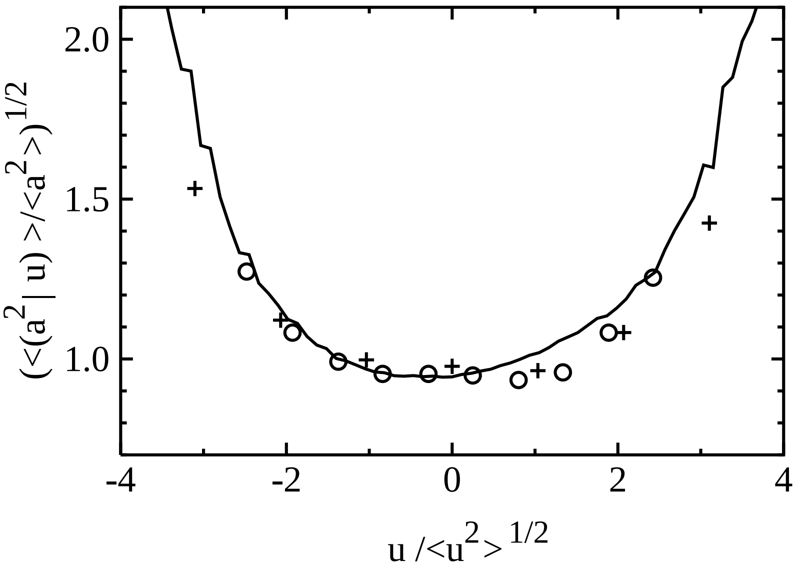

Figure 4.30: Standard deviation of the acceleration conditional on the velocity. Circles are $R_\lambda = 970$, Crosses are $R_\lambda = 200$, solid line is from numerical simulations by Yeung (2000) at $R_\lambda = 235$.

ation in which all particles are tracked for the full time they are in the detection volume, residence time weighted sampling will give an unbiased sample of any statistic defined at a single point in time (Buchave et al, 1979). This can be understood as follows. If the seeding is truly random then any particle is equally likely to be marked. If the flow is homogeneous across the detection volume and statistically stationary, then sampling each particle while it is in view is identical to sampling all particles all the time. On the other hand, statistics that depend on a time span along the track are not sampled correctly by residence time weighting. For example, some types of events may never stay in view over the time span of interest, and so can not be sampled. Thus the shape of the curves of acceleration variance versus fit time can have non-universal dependence on the large scale in the flow while they still extrapolate back to the correct acceleration variance at zero fit time. Great care is going to be required to accurately deal with this effect when measuring Lagrangian velocity structure functions.

Another even more interesting perspective on this issue is given by Fig. 4.30 which shows the rms acceleration conditioned on the measured velocity for the runs at $R_\lambda = 200$ and $R_\lambda = 970$, and also from DNS data by Yeung (Yeung, 2000). When normalized by the rms acceleration and velocity, the curves are nearly collapsed. They show clearly that the acceleration standard deviation is larger at large velocities. The notion of a fully developed turbulent cascade implies that small scale quantities like the acceleration are independent of large scale quantities like the velocity. But this plot shows a significant correlation between the acceleration and the velocity. Surprisingly, the correlation does not seem to be smaller at larger Reynolds numbers.

An analogous effect has been observed by Sreenivasan & Dhruva (1998) where a correlation between spatial velocity differences and the velocity is studied. This data is from atmospheric turbulence with Reynolds number up to $R_\lambda = 20,000$. Since numerical simulations and grid turbulence experiments do not show a similar correlation, it was concluded that the correlation is caused by the large scale shear in the atmospheric boundary layer.

For the acceleration-velocity correlation we find the situation to be quite different. The strong correlation of high acceleration with high velocity is seen even in isotropic simulations, so it can not be simply a shear effect. It may be a result of the kinematic coupling of the velocity and acceleration. If the acceleration follows the K41 prediction as we observe at large Reynolds numbers, then an rms acceleration produces a velocity change of $\sqrt{a_0}u_\eta$ in 1 τ_η:

$$\delta u = \langle a_\alpha^2 \rangle^{1/2} \tau_\eta = (a_0 \epsilon^{3/2} \nu^{-1/2})^{1/2} \tau_\eta = a_0^{1/2} u_\eta. \tag{4.9}$$

Since

$$\frac{u_\eta}{u} = \frac{15^{1/4}}{R_\lambda^{1/2}} \tag{4.10}$$

the fractional change in velocity is

$$\frac{\delta u}{u} = \frac{a_0^{1/2} 15^{1/4}}{R_\lambda^{1/2}}. \tag{4.11}$$

Even at $R_\lambda = 1000$ this implies that the fractional change in velocity due to an rms acceleration over 1 τ_η is 15% if $a_0 = 6$. Since the temporal acceleration autocorrelation function of an acceleration component falls to zero in about 2 τ_η (Yeung & Pope, 1989), 1 τ_η is an appropriate time to use in this context. The acceleration probability distribution shows contributions to the variance from accelerations out to 10 times the rms, so there are significant numbers of trajectories whose velocity changes by more than 1 rms velocity over 1 τ_η. This must result in a velocity-acceleration correlation. It is not yet clear why the correlation is unchanged when the Reynolds number is changed. This effect is dramatically demonstrated by the rare event in Fig. 4.6. A more careful exploration of the acceleration-velocity correlation could be a fruitful avenue for future exploration. It may be that this is part of the explanation for why larger Reynolds numbers are required for even approximate K41 scaling to be observed in Lagrangian and pressure statistics than in Eulerian spatial velocity differences.

The exploration of the correlation of the acceleration with the tracking time and the velocity highlights some issues of acceleration sampling bias that need to be kept in mind when interpreting particle tracking data. They should not directly affect the acceleration variance measurements since these correlations should cause not sample bias in the limit of zero fit time. They must be considered though because they allow any of the velocity sample biases from section 4.9.2 to indirectly affect the acceleration samples. They also have significant effect on any multi-time statistics such as the acceleration as a function of fit time.

Chapter 5

Conclusions

One of the major conclusions of this thesis is that precise experimental Lagrangian measurements are possible, even at Reynolds numbers up to $R_\lambda = 1000$. A first round of experiments measuring particle trajectories with a position sensitive photodiode demonstrated the feasibility of particle tracking acceleration measurements. The second generation system based on silicon strip detectors has obtained a factor of 25 higher light sensitivity and a factor of 10 smaller position measurement error than the position sensitive photodiode. In addition it has the ability to track up to about four particles at one time. Using this system we have obtained a position dynamic range of over 5000:1 at a frame rate of 70 kHz.

Many issues of experimental technique for particle tracking in turbulence have been addressed. An optical system with forward scattering geometry has been developed which allows measurement of all three position components. The 46 $\mu\mathrm{m}$ polystyrene DVB spheres we used were found to be sufficiently spherical and to have high enough surface quality to allow positioning accuracy of 1% of their diameter. We have found that spherical tracer particles with particle-fluid density difference less than 5% have an acceleration variance that is within 10% of the small particle limit when the particles are 2.5η in diameter. In the range of particle size and density studied, it is primarily the particle size rather than the density that is causing the particles to have different acceleration than a fluid element.

The strip detector system has allowed measurements of the fluid particle acceleration variance in a flow between counter-rotating disks with $140 < R_\lambda < 970$ with an accuracy of about 10%. It has been found that in this flow over this range of Reynolds number, the normalized acceleration variance, a_0, increases with Reynolds number up to about $R_\lambda = 400$ and then becomes nearly constant at the higher Reynolds numbers. The two different acceleration components have variances that differ by 15% even at the highest Reynolds numbers.

We conclude that a_0 turns over from the $R_\lambda^{1/2}$ scaling seen in DNS for $R_\lambda < 235$ (Vedula & Yeung, 1999) to a much weaker trend above $R_\lambda = 400$. There is still a possibility that this turn over is a feature of the flow between counter-rotating disks and not a universal feature of turbulence. Measurements in other flows will be necessary to check this possibility. The measurements are not accurate enough to determine whether weaker

Reynolds number trends exist, such as the $R_\lambda^{0.13}$ predicted by Borgas (1993) using a Lagrangian multifractal model.

The acceleration probability distribution is found to have very strong stretched exponential tails and a flatness above 50, which means it is significantly more intermittent than other small scale quantities. This may be connected to several of the other observations. It may partially explain the lack of isotropy since other small scale quantities with large flatness such as the passive scalar gradient show deviations from isotropy at these Reynolds numbers (Sreenivasan, 1991). It may also be connected to the relatively high Reynolds numbers at which the acceleration variance turns over toward approximate K41 scaling. The large intermittency of the acceleration may require a larger separation of length scales before an equilibrium cascade can exist. For comparison, $\epsilon \sim u^3/L$ is valid for $R_\lambda > 50$ (Mydlarski & Warhaft, 1996), while $\nu^{1/2} \left\langle a^2 \right\rangle \sim \left(u^3/L\right)^{3/2}$ requires $R_\lambda > 400$.

We have identified some of the sample bias and other systematic errors that affect particle tracking experiments. Of particular interest is the strong acceleration-velocity correlation even at the largest Reynolds number studied. Careful attention to these issues will be required when measuring multi-time quantities from particle tracking experiments.

It is my hope that this work will be seen as a demonstration that the measurements necessary to explore the high Reynolds number Lagrangian properties of turbulence are possible. Many more issues remain to be explored with particle tracking experiments. These include inertial time range scaling of Lagrangian velocity differences, two particle dispersion, and the time evolution of multi-particle velocity differences.

Appendix A

Our First Measurements of Lagrangian Accelerations

This appendix is primarily comprised of the first paper we published during my graduate studies. It is entitled ”Lagrangian acceleration measurements in high Reynolds number turbulence” and was published in *Physics of Fluids,* **10**:9, 1998, p. 2268–2280. The measurements in this paper were made with a position sensitive photodiode. At the end of this appendix is a discussion of the ways in which much the higher resolution data that has been recently obtained from the silicon strip detectors has led us to reinterpret some of this data.

A.1 Lagrangian acceleration measurements with a position sensitive photodiode

A.1.1 Abstract

We report experimental measurements of Lagrangian accelerations in a turbulent water flow between counter–rotating disks for Taylor Reynolds numbers $900 < R_\lambda < 2000$. Particle tracks were recorded by imaging tracer particles onto a position sensitive photodiode, and Lagrangian information was obtained from fits to the position versus time data. Several challenges associated with extracting Lagrangian statistical quantities from particle tracks are addressed. The acceleration variance is obtained as a function of Reynolds number and shows good agreement with Kolmogorov (’41) scaling. The Kolmogorov constant for the acceleration variance is found to be $a_0 = 7 \pm 3$.

A.1.2 Introduction

An understanding of Lagrangian statistics is of great importance in the ongoing effort to develop both fundamental and practical descriptions of turbulence. This was recognized already by G.I. Taylor Taylor (1921) in his seminal paper on turbulent diffusion, but almost no studies of Lagrangian turbulence quantities at large Reynolds numbers have been performed. The primary reason for this has been the lack of tools for measuring or calculating Lagrangian statistics at large Reynolds numbers.

From a fundamental point of view, high Reynolds number Lagrangian turbulence data is needed to provide a new perspective from which to judge Kolmogorov's 1941 theory. A host of practical applications follow from the connection to turbulent diffusion. Lagrangian stochastic models are widely used for simulating turbulent flows in which transport is of primary interest. Examples include turbulent combustion (Pope, 1985) and pollutant transport in the atmosphere (Weil et al, 1992). These models are often applied at Reynolds numbers much larger than existing data, and so model constants are unknown.

Determining particle accelerations in a turbulent flow has long been recognized as a difficult problem. At large Reynolds numbers, particles are typically moving at high speeds along erratic trajectories whose accelerations are only correlated over times on the order of the Kolmogorov timescale (Yeung & Pope, 1989). In this situation, accurate acceleration measurements require high resolution, extremely high speed imaging equipment. Previous work had typically relied on pixel based video photography, and this resulted in pessimism about ever being able to measure the small scale Lagrangian properties of high Reynolds number turbulence (Nelkin, 1994)

In this paper we present experimental particle tracking measurements in a flow between counter-rotating disks for Taylor Reynolds numbers $900 < R_\lambda < 2000$, an order of magnitude higher than previously possible. We recorded particle tracks by imaging tracer particles onto a position sensitive photodiode, and obtained data with sufficient spatial and temporal resolution to measure accelerations. We report data on the velocity and acceleration statistics and discuss challenges in the data analysis. Our results for the acceleration variance as a function of Reynolds number are in excellent agreement with Kolmogorov's ('41) scaling predictions and as such provide the first evidence that at sufficiently large Reynolds numbers, Lagrangian acceleration statistics can be described by Kolmogorov scaling.

Lagrangian Kolmogorov scaling

The Kolmogorov (1941b) hypotheses yield predictions for the scaling of several Lagrangian statistics that have never been tested. Following the notation of Monin & Yaglom (1975) the second order Lagrangian velocity structure function is defined as

$$D_{ij}^{L(2)}(\tau) = \langle (u_i(t+\tau) - u_i(t))(u_j(t+\tau) - u_j(t)) \rangle, \tag{A.1}$$

where u_i and u_j are components of the velocity vector of a fluid particle and τ is a time difference. If the flow is statistically stationary and $\tau << T_L$, where T_L is the Lagrangian velocity correlation time scale, Kolmogorov's hypotheses predict that at sufficiently high Reynolds number

$$D_{ij}^{L(2)}(\tau) = (\epsilon\nu)^{1/2} \beta\left(\tau/\tau_\eta\right) \delta_{ij}, \tag{A.2}$$

where ϵ is the mean dissipation per unit mass, ν is the kinematic viscosity, $\tau_\eta \equiv (\nu/\epsilon)^{1/2}$ is the Kolmogorov timescale, and $\beta(\tau/\tau_\eta)$ is a universal function. Furthermore, in the inertial time range where $\tau >> \tau_\eta$, this result must be independent of ν and one obtains

$$D_{ij}^{L(2)}(\tau) = C_0 \epsilon \tau \delta_{ij}, \tag{A.3}$$

where C_0 is a universal constant. Similarly, for the higher order structure functions in the inertial time range

$$D^{L(p)}(\tau) \sim (\epsilon \tau)^{p/2}. \tag{A.4}$$

(For odd orders, $D^{L(p)}$ is zero by symmetry unless the absolute value of the velocity difference is used.)

Predictions for the moments of the fluid particle acceleration probability density function (PDF) can be obtained by assuming that $u_i(t)$ is differentiable and taking the limit $\tau \to 0$ of the Lagrangian velocity structure functions. In particular, the second order structure function scales as τ^2 for small τ yielding the prediction for the acceleration variance

$$\langle a_i a_j \rangle = a_0 \epsilon^{3/2} \nu^{-1/2} \delta_{ij}, \tag{A.5}$$

where a_0 is another universal constant. The analysis that led to Eq. (A.5) can also be extended to the higher moments of the acceleration distribution, and it is found that Kolmogorov's 1941 hypotheses predict that the normalized acceleration moments should be constants

$$\frac{\langle a^p \rangle}{\langle a^2 \rangle^{p/2}} = a_p. \tag{A.6}$$

Note that the acceleration variance is the Lagrangian counterpart to the mean dissipation in the Eulerian perspective. Equation (A.5) can be viewed as predicting that the Lagrangian quantity, $\nu^{1/2}\langle a_i a_i \rangle$, is similar to the mean dissipation. It is characteristic of the small scales yet its magnitude is determined by the large scales, and hence it is independent of viscosity. In some ways, this is a natural quantity to use for Lagrangian Kolmogorov scaling in place of the dissipation. The measurements presented in this paper support the idea that the two scales are indeed related as predicted in Eq. (A.5).

Continuing the analogy with Eulerian results, it is expected that intermittency will cause deviations from the predictions for the higher acceleration moments and the higher order structure functions. Measurements of these quantities could lead to an important new perspective from which to study intermittency.

Prior work

Experimental Lagrangian measurements have been of three distinct types. The first measurements used the theory of turbulent dispersion by Taylor (1921) to determine the Lagrangian velocity correlation function from the scalar dispersion. Shlien & Corrsin (1974) provided a summary of measurements using this technique before themselves offering a set of measurements.

The second technique was optically tracking tracer particles that approximated Lagrangian motion. Snyder & Lumley (1971) provided the first systematic set of particle tracking velocity measurements from wind tunnel grid turbulence. Sato and Yamamoto Sato & Yamamoto (1987) have reported similar measurements in water tunnel grid turbulence. Virant and DracosVirant & Dracos (1997) have developed a stereoscopic system for measuring many particle tracks at once in three dimensions and report measurements in a turbulent boundary layer. Each of these studies has been helpful in illuminating the large scale Lagrangian properties of turbulence, but resolution limits and low Reynolds numbers have precluded comparison of small scale statistics with Kolmogorov's ideas.

The third technique has been to use the relations between the fourth order velocity structure functions and pressure structure functions Obukhov & Yaglom (1951); Batchelor (1951); Hill & Wilczak (1995) to calculate pressure gradient statistics from hot wire velocity measurements. This allows measurement of particle accelerations since the acceleration of fluid particles is dominated by the pressure gradient contribution for all but the smallest Reynolds numbers. This was originally suggested by YaglomObukhov & Yaglom (1951) and BatchelorBatchelor (1951), and has recently been convincingly demonstrated in DNS by Yeung.Vedula & Yeung (1999) Hill and Thoroddsen Hill & Thoroddsen (1997) have used this technique to study spatial acceleration correlations at $R_\lambda = 208.$ Spatial resolution limitations kept them from reporting one point acceleration statistics.

The only available high Reynolds number data came from balloon tracking in the atmospheric boundary layer.Hanna (1981) This data roughly supports the linear scaling of the Lagrangian velocity structure function in the inertial range (Eq. A.3) and the value of C_0 is 4.0 ± 2.0. Unfortunately, the small sample size and variable flow conditions limited the conclusions that could be drawn.

In addition to experiments, there have been several direct numerical simulations (DNS) of Lagrangian statistics of turbulence. Much as in the Eulerian case, DNS has provided unparalleled accuracy but has been limited to $R_\lambda < 200$. Yeung and Pope Yeung & Pope (1989) provided a comprehensive study of Lagrangian statistics in artificially forced isotropic homogeneous turbulence. Squires and EatonSquires & Eaton (1991) calculated statistics of homogeneous shear flows. More recently Yeung has studied two particle Lagrangian statistics Yeung (1994, 1997) and has extended the one-particle results to $R_\lambda = 200.$Vedula & Yeung (1999) A clear conclusion of these studies is that the acceleration variance is not scaling as predicted in Eq. (A.5) for $R_\lambda < 200.$

A.1.3 Experimental Setup and Methods

In this work we are reporting results on particle velocities and accelerations obtained by optically tracking tracer particles. The method is conceptually straight forward. The flow is seeded with small neutrally buoyant tracer particles and a portion of the flow is illumined by a light source. The illumined region is imaged onto a device to record tracer particle position as a function of time. In this way a two dimensional projection of the trajectory is obtained. As long as the tracer particles are sufficiently small to approximate fluid elements, Lagrangian velocities and accelerations can be calculated as derivatives of the particle positions.

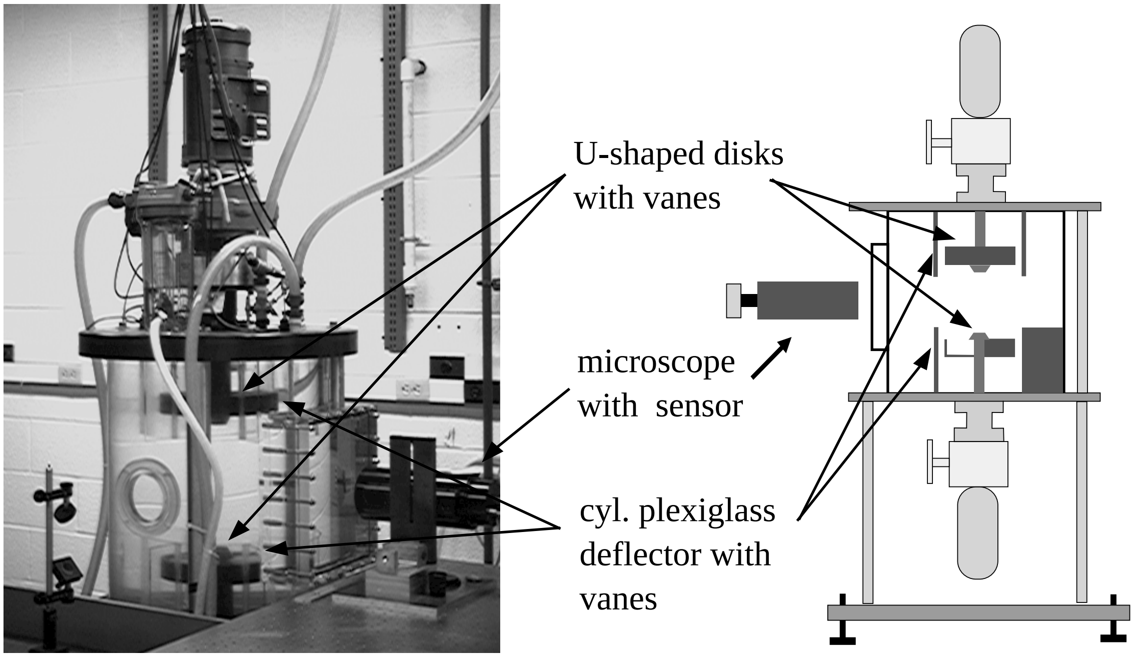

Figure A.1: Photograph and schematic of the experimental apparatus. In the schematic the lower part shows a cut through the u-shaped disc and the deflection cylinder. At the right the vanes can be seen.

The flow between counter-rotating disks

The flow we used was water driven between two counter-rotating disks in a closed cylindrical container of moderate volume $(110\ \ell)$. This flow has recently attracted much attention because it allows very high Reynolds numbers in a confined environment. Douady et al (1991); Maurer et al (1994); Belin et al (1996); Cadot et al (1995); Fauve et al (1993) The effects of the recirculating inhomogeneous flow are potentially a concern for large scale statistics, but for the dissipation scales at the Reynolds numbers attained it seems reasonable to expect that this will not be a problem.

A picture and schematic of the apparatus are shown in Fig. A.1. It consisted of a cylindrical container made of plexiglass (PMMA) with hard anodized aluminum top and bottom plates. The setup could be temperature controlled by water running through channels in the plates. The transparent cylindrical shell had a diameter of $48.3\ \mathrm{cm}$ and a height of $60.5\ \mathrm{cm}$. A large plane window was mounted on the side to allow undistorted visualization, and a smaller circular, plane window was mounted at 90° for illumination. The two circular disks of $20.3\ \mathrm{cm}$ diameter had u-shaped cross sections with height of $4.3\ \mathrm{cm}$ and were mounted to $5\ \mathrm{cm}$ diameter shafts that were connected to the external drive. Twelve equally spaced vanes were mounted in each disk to provide efficient stirring. The disks were spaced $33\ \mathrm{cm}$ apart. Both the disks and the shafts were machined from aluminum and hard anodized for corrosion resistance. The disks were surrounded by a stationary, cylindrical, plexiglass deflector shield of $25.4\ \mathrm{cm}$ diameter which extended $5\ \mathrm{cm}$ beyond the disks. These deflectors confined the turbulence to the central region of the apparatus. They also had vanes that extended to the edge of the apparatus which damped out any large scale rotation caused by slight mismatch in the disk speeds. The disks were driven by two electronically controlled $0.9\ \mathrm{kW}$ DC motors, which were geared down by a variable speed reducer. The disk rotation frequency was measured optically by an LED/photodiode pair and was feedback controlled to 0.1% long term stability with the fluctuations due to the turbulence being less than 1%. The apparatus was vacuum tight and allowed a thorough degassing of the fluid to eliminate bubbles. The fluid was filtered to particle sizes $< 0.3\ \mu\mathrm{m}$, and the relatively small volume made it possible to maintain excellent chemical purity.

Detection system

For illumination of the detection region, a $5\mathrm{W}$ continuous wave Argon ion laser beam was used which produced a cylindrical illumination volume that passed horizontally (along the *x* axis) through the center of the cell. The laser beam had a Gaussian profile with a width of $1\ \mathrm{mm}$, and was polarized in the *y* direction. A $1.5\ \mathrm{mm}$ section of the beam was viewed from 90° (along the *z* axis) at a distance of $30\ \mathrm{cm}$ by a long working distance microscope. The image was focused onto a position sensitive photodetector. This is shown schematically in Fig. A.2A.

The detector was essentially a large square photodiode ($1.0\ \mathrm{cm}$ on a side) which allowed an analog two-dimensional measurement of the position of a single light spot. It works by measuring the fraction of the photo-current that migrates to the top vs. bottom of the front plane, and to the right vs. left of the back plane. Each of the four leads was connected to a charge sensitive amplifier and signals from two opposing sides were added and subtracted in analog. The resulting signals were digitized and stored by a 4 channel digital oscilloscope. The waveforms were acquired at a $250\ \mathrm{MHz}$ digitization rate. Positions were only needed at typically $100\ \mathrm{kHz}$, so 2500 samples were averaged at each point to reduce the noise. The resulting waveforms were transferred via the GPIB bus to a Pentium computer where they were stored. Positions were calculated later by a division of the corresponding difference and sum waveforms. The time interval between recorded tracks was limited to $0.5\ \mathrm{s}$ by the data transfer rate through the GPIB bus. The detector was carefully checked for linearity of its position output by scanning a fiber optic over its surface. It was linear to better than 1% over the central 70% of its length in both the horizontal (*x*) and vertical (*y*) directions. To minimize position measurement error, only positions which were within this central region were used in the data analysis.

After an experiment, the position scale of the detection system was calibrated by moving the unchanged system (microscope and detector) from the turbulence chamber to an aquarium of the same optical geometry. The end of a multimode optical fiber attached to a micrometer and was positioned within the water in the focus of the microscope. The positions of the light spot were recorded as the fiber optic was moved. With this technique we obtained a calibration of the position scale within $\pm 2\%$.

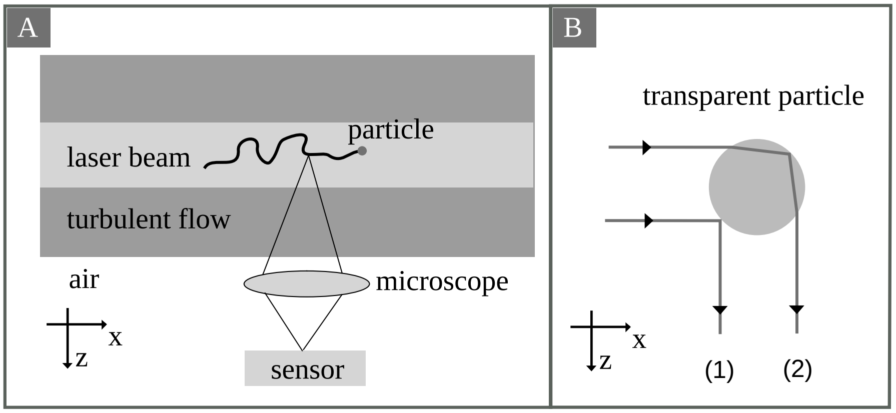

Figure A.2: (A) Schematic of the optical setup and (B) of the primary (1) and secondary (2) reflections from the transparent spheres.

Particles

For tracer particles, we used transparent polystyrene spheres with density $1.06\ \mathrm{g/cm^3}$. The concentration of particles was kept low and was chosen to give one particle track every 1 to $2\ \mathrm{sec}$. For the particles to follow the flow passively one would like to minimize their size. In our experiment the minimal size was dictated by the need to gather enough light for the detector to give sufficiently accurate position measurements. We used two different diameter particles. One batch had mean diameter of $250\ \mu\mathrm{m}$ taken from a $150\ \mu\mathrm{m}$ to $350\ \mu\mathrm{m}$ sieve cut. The other had a mean diameter $460\ \mu\mathrm{m}$ with standard deviation of $8\ \mu\mathrm{m}$.

We also tried to use higher reflectivity, silver coated, hollow glass spheres. These spheres would have had the advantage that smaller particles could have been used. However, experiments showed that the reflective surface of the particles was very inhomogeneous. As the particles rotated, the inhomogeneous reflectivity of the particles' surface led to rapid fluctuation in the reflected light intensity. Due to the relatively slow response time of the position sensitive photodiode ($2\ \mu\mathrm{s}$), these rapid fluctuations could not be resolved and resulted in inaccurate position measurements. In an attempt to overcome this problem we also used a position sensitive photomultiplier tube. Although this sensor had high light sensitivity and an ultrafast response time of $1\ \mathrm{ns}$, its spatial resolution was not sufficient.

Particle tracks

Figure A.3 contains two example particle tracks. The majority of the tracks recorded were almost straight like the one shown in Figs. A.3A and A.3B, but a few displayed large curvature such as the one shown in Figs. A.3C and A.3D. These sharply curved tracks suggest the expected intermittency of Lagrangian accelerations, and may be connected to the coherent structures which have recently attracted much interest. Belin et al (1996); Cadot et al (1995); Jimenez et al (1993)

In the data analysis, random and systematic errors of the measured particle position

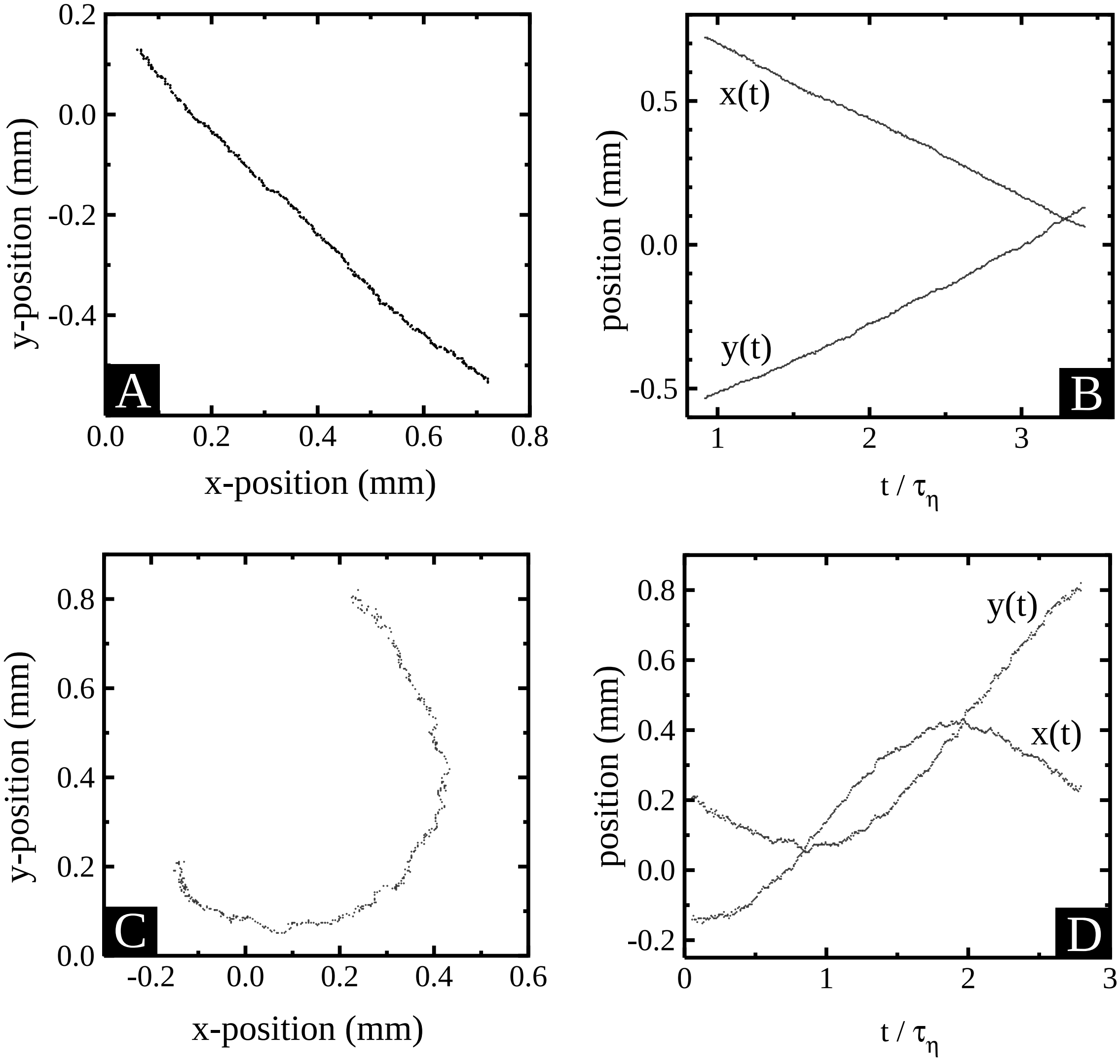

Figure A.3: Two examples particle tracks for run 9 with $\tau_\eta = 0.59$ ms and $\eta = 23\ \mu$m. The upper trajectory represents a typical acceleration (at the center, $a_y = 90\ \mathrm{m/s^2}$, half the rms acceleration) while the lower track represents a rare event (at the center, $a_y = 1490\ \mathrm{m/s^2}$, 8 times the rms). Both the particle trajectories (A & C) and the positions versus time (B & D) are shown.

data had to be considered. The accuracy of the position measurements was sensitively dependent on the intensity of the light gathered onto the detector. Due to the Gaussian intensity profile of the laser beam, a trajectory typically spanned a range of intensities and correspondingly a range of measurement uncertainties. To obtain an estimate of the magnitude of the random measurement error as a function of intensity, we fitted a polynomial to each trajectory assuming constant error. For each data point, the residual was calculated and registered with the point's light intensity. Repeating the same procedure for all trajectories, we obtained the rms residual as a function of intensity; and this was used as the position measurement error. The order of the fit polynomial was chosen to be $1 + t_\ell/\tau_\eta$, truncated to an integer, where t_ℓ it the total time the particle was tracked, and τ_η is determined in Section *A.1.6*. This form was determined by studying the mean square deviation of fits as a function of track length for tracks generated by the Lagrangian stochastic model described in Section *A.1.6*.

In addition to random position errors, we identified at least two types of systematic errors in the data. One occurred when multiple particles came into view at the same time. This resulted in sudden variations in the particle position, as the detector provided only the "center of mass" position of the light hitting it. We observed these tracks only rarely, since the time between detections was a factor of 500 longer than the time it took a particle to pass through the observation volume. Most of these tracks could be rejected on the basis of the nearly discontinuous position and velocity. Along the laser beam direction (the *x* axis), the transparent particles led to two reflections. This is shown schematically in Fig. A.2B. The larger horizontal size of the light spot increased the random uncertainty in the measured *x* position. It also had a systematic effect when one of the reflections was shadowed by another particle that passed through the laser beam outside of the observation volume. This shadowing effect led to trajectories where the particle suddenly appeared to have moved. Fortunately, this did not appear in the *y* data and it was simple to estimate its effect.

Another possible source of error was the nonuniformity of the polystyrene particles. Scratches and dents in the surface, deviations from a spherical shape, and index of refraction variations within the sphere would lead to changes in the position of the light spot produced by rotating particles, and thus to an error in the particle position measurements. While viewing the particles under a microscope, it did not appear that these effect should be large. However, this might contribute to the correlated errors discussed in Section *A.1.6*.

A.1.4 Data

The data sets presented in this paper were all recorded with the detection region at the zero mean velocity point at the center of the flow. We adjusted the detection system to the point that gave zero mean velocity, since we were able to measure the mean velocities with better spatial resolution than we could determine the geometric center of the flow. Position in the unmeasured *z* direction was set to our best determination of the geometric center of the flow—which should be the zero mean velocity location to within about 5 mm.

Table A.1: Parameters for all data runs taken with the position sensitive photodiode.

f	$\tilde{u}$	R_λ	ν	ϵ	τ_η	η	t_m/τ_η	N_{tr}
(Hz)	(m/s)		10^{-6} m^2/s	m^2/sec^3	ms	μm		
250 μm Particles								
1.50	0.168	723	1.01 ± 0.02	0.023	6.69	82	1.5	4148
2.50	0.281	985	0.91 ± 0.01	0.106	2.93	52	1.7	15211
2.50	0.281	921	1.04 ± 0.02	0.106	3.14	57	1.6	11910
3.75	0.419	1180	0.95 ± 0.05	0.351	1.64	39	3.0	22000
3.75	0.419	1147	1.00 ± 0.02	0.351	1.69	41	3.0	26870
5.00	0.546	1338	0.96 ± 0.03	0.777	1.11	33	4.5	8499
5.00	0.571	1340	1.00 ± 0.02	0.887	1.06	33	1.9	8318
6.25	0.689	1499	0.97 ± 0.02	1.586	0.78	27	2.6	18764
6.25	0.693	1503	0.97 ± 0.02	1.559	0.79	28	6.3	15077
7.50	0.834	1668	0.94 ± 0.02	2.762	0.59	23	3.4	28790
9.50	1.063	1981	0.85 ± 0.02	5.720	0.39	18	5.3	8132
9.50	1.060	2004	0.83 ± 0.02	5.671	0.38	18	5.3	12579
460 μm Particles								
2.50	0.280	1011	0.86 ± 0.01	0.104	2.88	50	1.7	3962
3.75	0.419	1236	0.86 ± 0.01	0.351	1.57	37	3.18	6134
5.00	0.559	1410	0.88 ± 0.01	0.832	1.03	30	4.9	7995
5.00	0.559	1410	0.88 ± 0.01	0.832	1.03	30	9.7	13056
6.25	0.693	1595	0.86 ± 0.02	1.571	0.74	25	2.7	13994
7.50	0.834	1777	0.84 ± 0.01	2.802	0.55	21	3.7	13965
9.50	1.060	2021	0.82 ± 0.01	5.688	0.38	18	5.3	13156

Each data set consists of a large number of tracks with 500 position measurements per track. Because particles remained in the detection region for varying time periods, the valid part of each track was some fraction of the total 500 points. Data was acquired at about 5000 tracks per hour.

The maximum Reynolds number studied was limited by the power available from the motors. The minimum Reynolds number was limited by the necessity of keeping enough particles suspended in the flow. For small fluctuating velocities, the particles settled out of the inactive regions in the flow; and thus sufficient statistics could not be collected at lower Reynolds numbers.

Parameters for all data sets are given in Table A.1. Each run is identified by a number. The rotation frequency of the disks is f. The typical velocity used for scaling is $\tilde{u} = (\langle u_i u_i \rangle /3)^{1/2}$ where the unmeasured velocity component (u_z) is assumed to have the same statistics as the measured horizontal component (u_x) due to the cylindrical symmetry. For the $460\ \mu$m particles, the error in the *x* position measurements were too large to determine accurate *x* velocities. The *y* velocities were very similar to the values for the smaller particles, so we set $\tilde{u}$ for the larger particles equal to the average of the velocities of the smaller particles at the same frequency.

We determined the dissipation by

$$\epsilon = \frac{\tilde{u}^3}{L}. \tag{A.7}$$

where $L = 0.21\ \mathrm{m}$ includes the normal constant coefficient in this equation and is determined from the form of the acceleration autocorrelation function in section *A.1.6*. For the Taylor microscale Reynolds number, we used the usual isotropic definitions

$$R_\lambda = \frac{\tilde{u}\lambda}{\nu} = \left(\frac{15\tilde{u}L}{\nu}\right)^{1/2}, \tag{A.8}$$

since

$$\lambda = \left(\frac{15\nu\tilde{u}^2}{\epsilon}\right)^{1/2}. \tag{A.9}$$

The kinematic viscosities given are for the mean temperature of each run, with the uncertainty reflecting temperature drift. Values were obtained from Ref. 31. The Kolmogorov scales of time and length are $\tau_\eta = (\nu/\epsilon)^{1/2}$ and $\eta = (\nu^3/\epsilon)^{1/4}$ respectively; t_m is the maximum tracking time, which is determined by the time base setting on the oscilloscope; N_{tr} is the number of tracks with more than 25 positions recorded.

A.1.5 Measuring Velocity Statistics

Measurements of the mean velocity and rms velocity fluctuations are essential in describing the turbulent flow. As with almost all known fluid measurement techniques, it is non-trivial to extract these statistical quantities from the raw data. Just as in burst Laser Doppler Anemometry (LDA), the probability of a particle being observed depends on its velocity; thus the naive velocity moments calculated by sums over observed particle velocities are incorrect. Buchave, George, and Lumley Buchave et al (1979) provided an analysis of the basic issues and a method of calculating the corrected velocity moments using particle transit (residence) times.

We have developed a different but equivalent method based on the form of the velocity probability density function (PDF). The motivation for this was twofold:

(i) The data acquisition procedure applied here and described above did not allow the measurement of residence times for all tracks, *i.e.*, some slow particles stayed in the detection region longer than the digitization time. This made it impossible to use the method discussed by Buchave et al. Buchave et al (1979)

(ii) The PDF method opens the door to Monte Carlo modeling of the detection process. By using Lagrangian stochastic models one can simulate tracks from which one can calculate the PDF for detecting a particle conditional on its velocity vector. As shown below this conditional PDF can be used to calculate the true PDF of the velocity. It should be possible to apply this method to other situations where the residence time method is not easily applicable. Examples would be where the detection region is large or oddly shaped, or multiple particles are tracked at once. For the purposes of this paper the use of Monte Carlo modeling was not necessary.

Correction of measurement biases in the velocity PDF

Let us define the correct 3-dimensional joint velocity PDF to be $F_u(\vec{u})$. The measured PDF is given by the correct distribution conditional on a valid particle track being detected: $F_{u|D}(\vec{u}|D)$, where D can be thought of as a binomial random variable representing whether a particle is detected or not. The problem is to model the detection process so that a relationship between F_u and $F_{u|D}$ can be found. Our solution is to develop a model for $F_{D|u}(D|\vec{u})$ and then use Bayes' theorem to invert this to the desired form.

$$F_{u|D}(\vec{u}|D) = \frac{F_{D|u}(D|\vec{u})F_u(\vec{u})}{\int F_{D|u}(D|\vec{u}')F_u(\vec{u}')d^3\vec{u}'}. \tag{A.10}$$

There is a rich history of philosophical debate surrounding the application of this theorem to decision theory, but its use here as a means of inverting conditional probabilities is well accepted. Lindsey (1996)

In order to develop a model for $F_{D|u}(D|\vec{u})$, we assume:

(i) The detection region is small enough that velocity PDFs do not vary across it.

(ii) The velocity of a particle does not change significantly between entering the detection volume and the point where the velocity is measured.

(iii) The detection region is isotropic, so that its cross sectional area does not depend on the velocity direction.

(iv) Particles are uniformly distributed in space with low enough density that the probability of multiple particles being detected is negligible.

(v) All particles that enter the detection region produce valid tracks.

This model corresponds well to the situation in our flow. Assumption (i) was clearly valid across the $1\ \mathrm{mm}^3$ detection region. Assumption (ii) was fairly good since measurements given later showed that changes in velocity were typically less than 15%, and they were this large only for the largest Reynolds numbers. By changing the point along the track at which the velocity was sampled, we determined that this effect was not significant. Assumption (iii) was probably the weakest since the detection region was a cylinder. However, the geometry used in the experiment was still reasonably approximated by a sphere. With our enclosed turbulent flow and maximum data rates of two measurements per second (iv) was satisfied. Assumption (v) is difficult to quantify. Some particles will pass through the corners of the region and their tracks will not have enough points to fit a velocity. This could lead to a bias against large velocities, but should not be a large effect.

With these assumptions, the rate of particles passing through a spherical detection region of cross sectional area ΔS is

$$R = |\vec{u}|n\Delta S, \tag{A.11}$$

where n is the number of particles per unit volume. In this situation, the PDF of the number of particles detected in a time interval Δt, conditional on the velocity, is a Poisson distribution. With small particle densities and short particle transit times, only the probability of one particle is significant, and it simplifies to

$$F_{D|u}(D|\vec{u}) = R\Delta t = |\vec{u}|n\Delta S\Delta t. \tag{A.12}$$

Inserting this into Bayes' theorem gives

$$F_{u|D}(\vec{u}|D) = \frac{|\vec{u}|n\Delta S\Delta t F_u(\vec{u})}{\int |\vec{u}'|n\Delta S\Delta t F_u(\vec{u}')d^3\vec{u}'}, \tag{A.13}$$

and thus the measured distribution is related to the correct one by

$$F_{u|D}(\vec{u}|D) = K|\vec{u}|F_u(\vec{u}). \tag{A.14}$$

where K is a normalization constant. With Eq. (A.14) the correct PDF can be calculated from the full 3-dimensional measured distribution.

The method described above is equivalent to the method of residence time weighting described by Buchave et al. Buchave et al (1979) We show this for the mean velocity, since the higher moments of the velocity distribution can be shown to agree in the same way. They obtain the mean velocity by a residence time weighted average of the sampled velocities

$$\overline{u_i} = \frac{\sum_k u_i^{(k)}\Delta t^{(k)}}{\sum_k \Delta t^{(k)}}, \tag{A.15}$$

where $u_i^{(k)}$ is the k^{th} measurement of the velocity component i, and $\Delta t^{(k)}$ is the time over which the k^{th} particle traverses the observation volume. In PDF notation, the equivalent quantity is

$$\overline{u_i} = \frac{\int u_i \Delta t\ F_{u|D}(\vec{u}|D)d^3\vec{u}}{\int \Delta t\ F_{u|D}(\vec{u}|D)d^3\vec{u}}. \tag{A.16}$$

Now substitute $F_{u|D}(\vec{u}|D)$ from Eq. (A.14) and recognize that Δt is just $\ell/|\vec{u}|$ where ℓ is the distance the track travels. Since ℓ is independent of the velocity, we find

$$\overline{u_i} = \int u_i F_u(\vec{u})d^3\vec{u}. \tag{A.17}$$

Thus we see that residence time weighting of samples from the PDF in Eq. (A.14) produces the correct velocity moments.

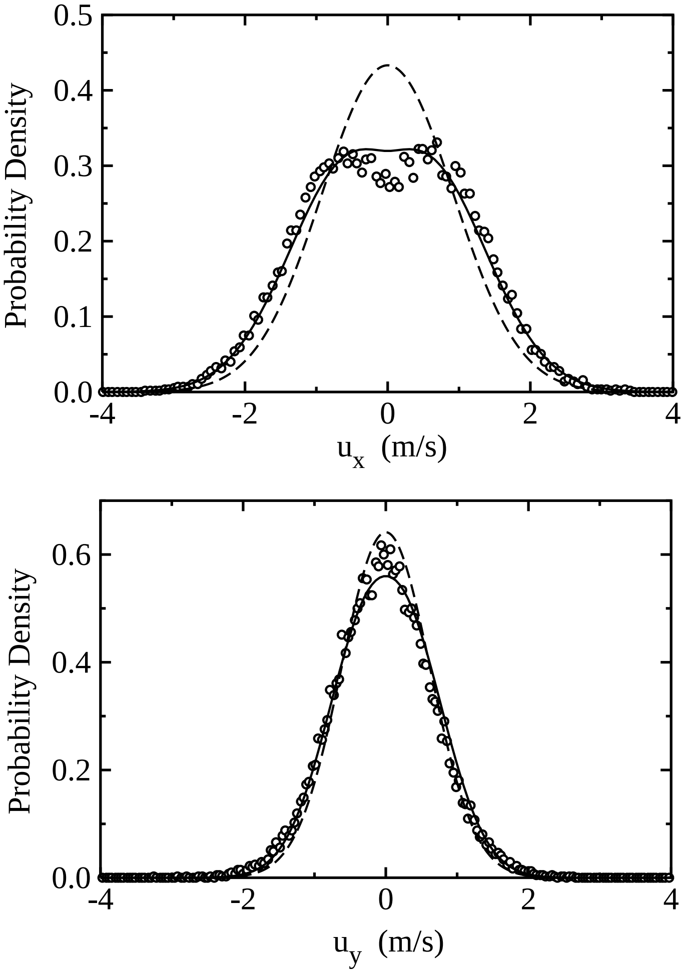

Figure A.4: PDF of the *x* and *y* component of the measured velocities, computed from linear fits to particle tracks for run 9. Also shown is the fit using Eq. (A.18) (solid) and the true velocity PDF after bias correction (dashed).

Velocity data analysis and results

Our primary measurements are made in the zero mean velocity region at the center of the cylindrically symmetric flow. The statistics of the unmeasured *z* velocity component should be the same as for the measured *x* component because of the cylindrical symmetry. In addition, the Reynolds stresses should be zero at this location due to symmetry.

We measured the statistics of the *x* and *y* components of the particle velocities from linear fits to the center 25 points of each recorded track. The *x* and *y* projections of the measured joint velocity PDF for run 9 is shown in Fig. A.4. The Reynolds stress between the *x* and *y* velocity components was zero to within the measurement resolution.

To correct for the biases discussed above, we were not able to apply Eq. (A.14) directly because we did not have measurements of the *z* velocity component. We circumvented this problem by assuming that the correct velocity PDF was a joint Gaussian. Far from the walls of high Reynolds number flows, velocity PDFs are know to be very nearly

Gaussian with deviations which should not be perceptible in the second order moments which we need to determine.Noullez et al (1997) With this information, Eq. (A.14) can be integrated over the unmeasured *z* direction to obtain the form of the joint PDF of the measured *x* and *y* velocities,

$$F^*_{u|D}(u_x, u_y|D) = K \int_{-\infty}^{\infty} |\vec{u}| \exp(-\frac{u_x^2}{2\sigma_x^2} - \frac{u_y^2}{2\sigma_y^2} - \frac{u_z^2}{2\sigma_x^2}) du_z, \qquad \text{(A.18)}$$

where only σ_x and σ_y are fit parameters.

To determine these two unknown velocity standard deviations, we integrated Eq. (A.18) numerically and used a nonlinear least squares fitting routine to fit the model to the measured 2-dimensional joint PDF.

Projections of the model fit to the measured PDF are shown in Fig. A.4. The fitted values are $\sigma_x = 0.921$ m/s and $\sigma_y = 0.622$ m/s. The ratio of the rms velocity components is 1.48 which is typical of the values observed in homogeneous shear flows. Garg & Warhaft (1998) The model captured the measurement bias quite well, except that the fit slightly overestimated the probability for *x* velocities near zero. As a result, it appears that the model slightly underestimated the rms *x* velocity. With the ad hoc assumption that the *x* and *z* velocity variances are different in Eq. (A.18), the model produces a considerably better fit to the central region of the *x* velocity PDF. Although this allowed a better fit, it only led to a 3% change in the fitted rms *x* velocity. Since it is likely that other approximations in the model and not lack of symmetry is causing the deviation, we fitted only for σ_x and σ_y and recognize a 3% uncertainty in the bias corrections.

The issue of measurement uncertainty in the measured velocity PDF should be addressed. The error contribution can be determined from plots of the standard deviation of the measured PDF versus the number of points used in the fit to estimate the velocity. These show that for the linear fits over 25 points, there was a 1% standard deviation contribution due to velocity measurement error, and a 1% bias due to the faster tracks being less likely to stay in the detection region long enough to be included in the sample. These effects are individually small, and together they tend to cancel.

The typical velocity used for scaling of the results presented in this paper is $\tilde{u} = (\langle u_i u_i \rangle /3)^{1/2}$. Figure A.5 shows that $\tilde{u}$, σ_x, and σ_y all scale linearly with the disk frequency. For each disk frequency, other than $f = 7.5$, two independent measurements are plotted. The data points with the largest deviation from the linear scaling at $f = 5$ have lower statistics than most of the runs (see Table A.1), and appear again as the largest deviations from Kolmogorov scaling in Fig. A.12. The linear scaling is important in establishing that there were no changes in the large scale structure of the flow over the Reynolds numbers studied.

A.1.6 Particle Acceleration Measurements

The most challenging part of measuring particle accelerations in high Reynolds number turbulence is to obtain high enough spatial and temporal resolution on particle position measurements. With the analog positioning system described above, we obtained position resolution of typically 5 μm and temporal resolution up to 4 μs. In our flow, this was

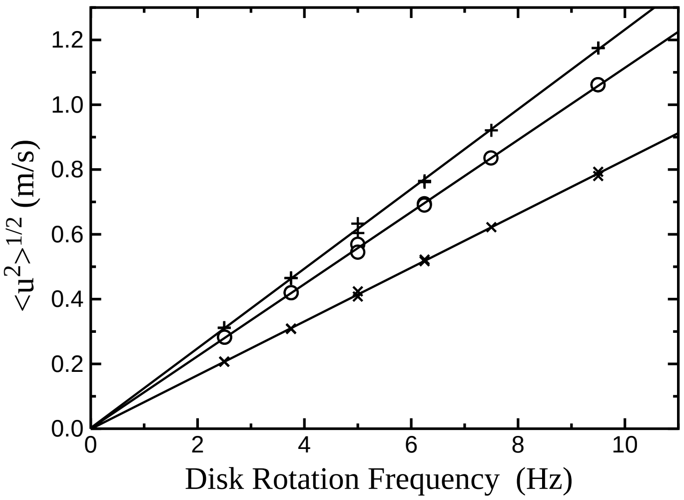

Figure A.5: Fluctuating velocities for runs 1 to 11. ○, $\tilde{u}$; $+$, σ_x; $\times$, σ_y. Solid lines are linear fits. The linear scaling demonstrates that there were no significant changes in the large scale structure of the flow.

sufficient to allow accurate determination of the acceleration variance and the extraction of the general form of the acceleration autocorrelation function. To distinguish between the true accelerations and the measurement errors, a rather involved data analysis was required which can be subdivided into three parts. In Section *A.1.6* we describe the technique used to extrapolate the measured acceleration variance to eliminate the contribution from measurement errors. Section *A.1.6* describes a method for correcting the systematic error introduced by fitting a second order polynomial to the trajectory. In Section *A.1.6* we present a method for determining the dissipation ϵ from the acceleration correlation function. At several points, the data analysis required knowledge of a quantity that was determined in a later section. It was found that iterating the entire analysis twice was sufficient to provide self-consistency.

Extracting accelerations from particle tracks

The first step in extracting accelerations from particle trajectories was to eliminate the tracks that had large position measurement errors. This was done by fitting a polynomial to the entire track and eliminating tracks with large reduced χ^2 for the fit,Taylor (1997) *i.e.* tracks with large rms deviation from the fit. Figure A.6 shows the distribution of measured reduced χ^2 values. Particle tracks with a reduced $\chi^2 > 6$ were not considered for the data analysis. This cutoff resulted in about 4% of the *y* tracks and 7% of the *x* tracks being eliminated. Adjusting the cutoff down to 3 and up to 12 made only a 2% change in acceleration variance measurements, even though the measurement error contribution discussed later changed significantly. The order of the fit polynomial was chosen to be $1 + t_\ell/\tau_\eta$, just as in Section *A.1.3*. This procedure eliminates almost all the multiple particle and most of the shadowing effects discussed in Section *A.1.3*.

After elimination of the spurious trajectories, a polynomial was fitted to a certain

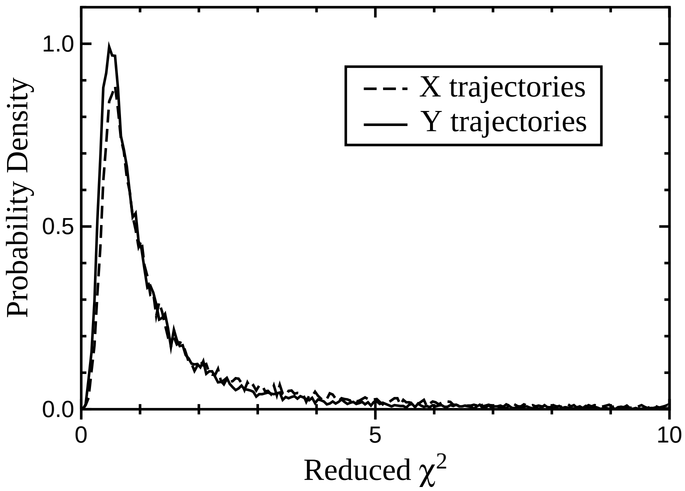

Figure A.6: Probability distributions of reduced χ^2 values of fits to position data from run 9. The slightly poorer fits of the *x* data may be attributed to the increased error due to double reflections as described in Section *A.1.3*.

length of the track with the second time derivative giving the acceleration. As polynomial fitting is a linear operation, the acceleration obtained from the fit can be thought of as the acceleration of a fit to the true trajectory added to the acceleration of a fit to the measurement errors. The ideal situation would be to fit over a section of each track that was long enough that the acceleration due to the measurement errors would be negligible while still short enough that the polynomial was able to reproduce the trajectory. For our data the measurement errors were too large for this direct approach.

The technique we used to measure the acceleration was to fit second order polynomials to trajectory segments of size Δt centered around the midpoint of the trajectory—with Δt ranging from just a few points up to the entire tracking time. We repeated this procedure for all tracks in a run and thus obtained the acceleration variance as a function of trajectory time segment used in the fit. For very short trajectory segments the measured acceleration variance was dominated by noise; while for increased segment length the noise contribution decreased. Very few particles were tracked for the longest segments, and consequently measurement uncertainty increased and eventually no variance could be measured. An example of this is shown in Fig. A.7 for the *y* trajectories from run 9. The *x* trajectories were very similar except for a slightly larger noise contribution as described earlier in Section *A.1.3*. The error bars were calculated by dividing the sample into 8 sets, processing each set, and taking the standard deviation of the results from each set divided by the square root of the number of sets.

If the measurement errors were Gaussian and uncorrelated, the contribution to the acceleration variance from position measurement errors would be proportional to Δt^{-5}, where Δt is the time interval spanned by the evenly spaced points used in the fit.Wand & Jones (1995) In our case the errors were correlated and Δt^{-5} was not the correct form. However, the data for the square root of the measured acceleration variance was very nearly a constant added to a power law. This is equivalent to the variance having two

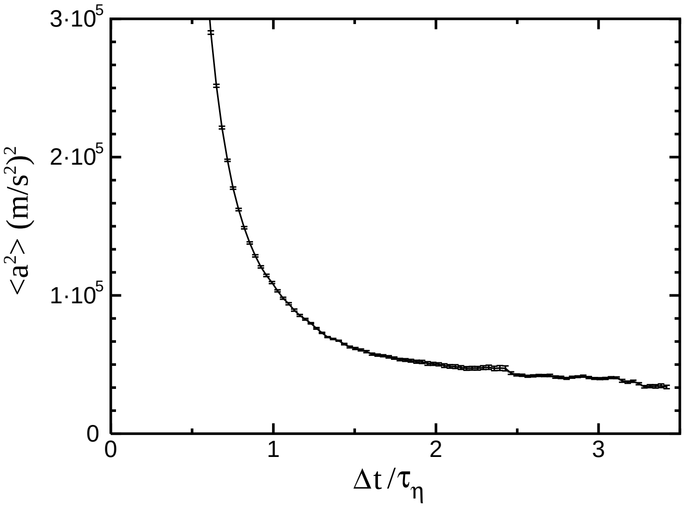

Figure A.7: Measured acceleration variance versus the trajectory time segment used in the fit. Data is for the *y* trajectories from run 9.

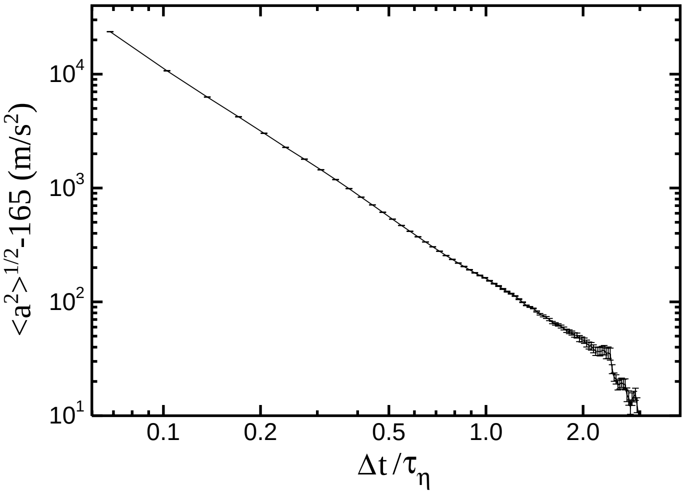

Figure A.8: Log-log plot of the square root of the acceleration variance with the fitted constant $A = 165 \text{ m}/\text{sec}^2$ subtracted. The data is the same as for Fig A.7.

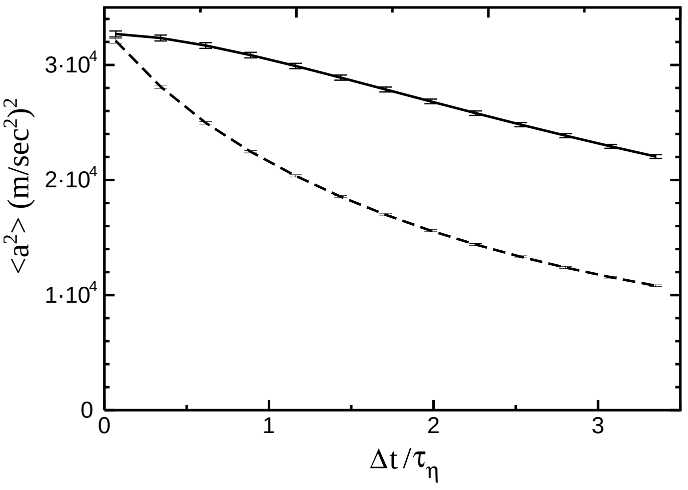

Figure A.9: Model calculation of the error in the acceleration variance due to under-resolved trajectories. The dashed line is from direct application of Sawford's model. The solid line is from a modified model with differentiable particle accelerations.

error correlation lengths balanced such that

$$\langle a^2 \rangle = A^2 + 2AB\Delta t^{-c/2} + B^2 \Delta t^{-c}. \tag{A.19}$$

We used this power law to extrapolate to the true acceleration variance A^2.

It is very hard to determine the exact correlations in the measurement errors, so we can not justify this form rigorously; but Eq. (A.19) provided excellent fits to the decay of the measured acceleration variances with increased length of fitted trajectories. Fitted values of the exponent c were usually between 3 and 3.4. The log-log plot of the square root of the data in Fig. A.8 with the fitted constant of $A = 165\ \mathrm{m/s^2}$ subtracted, clearly shows that the noise contribution had power law behavior.

Acceleration measurement bias

A concern with the technique described above was that fitting a second order polynomial over several Kolmogorov timescales (see Table A.1) may not have captured the true accelerations, *i.e.* the quadratic polynomials might not have fully resolved the true trajectory structure and thus might have underestimated the acceleration variance. To quantify this effect, we developed a model to produce simulated stochastic particle tracks, and analyzed these tracks using the same code as in the data analysis of the experimental runs. Then we used the acceleration variances obtained from the model tracks to calculate the magnitude of the errors introduced by not fully resolving the experimental trajectories. These errors were later used in Section *A.1.7* to correct for this effect.

The best model previously available for this is a second order Lagrangian stochastic model developed by Sawford. Sawford (1991); Pope (1994) This model uses a continuous but nondifferentiable process to model the Lagrangian acceleration, and calculates velocities and positions from integrals of the accelerations. The dashed line in Fig. A.9 shows the measured acceleration variance as a function of trajectory segment length when tracks from Sawford's model were analyzed. The extrapolation $t \to 0$ gives the true acceleration variance, which was an input parameter to the model. Figure A.9 shows that our fitting procedure underestimated the acceleration variance, and that the error increased rapidly with increasing trajectory time segment. Yet from the fact that the error due to under-resolved trajectories goes linearly and not asymptotically to 0 for $t \to 0$, we concluded that the model was insufficient.

To improve on this, we modified Sawford's model. We applied it to the third time derivative of the position rather than to the acceleration. This new model produced trajectories with continuous, differentiable accelerations, and thus better captured the known form of the acceleration autocorrelation function. The new form of the model is

$$\begin{aligned} d\dot{a}_i(t) &= -\left\{1+\frac{\tau}{T_\infty}\right\}\dot{a}_i(t)\frac{dt}{\tau} - \frac{a_i(t)}{T_\infty}\frac{dt}{\tau} \\ &\quad + \left\{2\langle \dot{a}_i^2\rangle\left(1+\frac{\tau}{T_\infty}\right)\right\}^{1/2}\frac{dW}{\tau^{1/2}}. \end{aligned} \tag{A.20}$$

where $\dot{a}_i(t)$ is the first time derivative of an acceleration component at time t. The rest of the notation is from the review by Pope. Pope (1994) The model constants, $\tau = 0.5\tau_\eta$ and $T_\infty = 0.7\tau_\eta$, were determined by fitting the acceleration autocorrelation function produced by the model to the Lagrangian DNS acceleration autocorrelation function from Yeung and Pope. Yeung & Pope (1989) As explained in the next section, it is expected that the DNS results remain unchanged at higher Reynolds numbers. The input parameter, $\langle \dot{a}_i^2\rangle$, is determined by the curvature of the acceleration autocorrelation function at the origin to be

$$\langle \dot{a}_i^2\rangle = \frac{\langle a_i^2\rangle}{T_\infty \tau}, \tag{A.21}$$

where no summation is implied. For $\langle a_i^2\rangle$ we use the Kolmogorov prediction, Eq. (A.5), with $a_0 = 7$ as determined in Section *A.1.7*.

This model produced better acceleration time series than Sawford's original model, but has non-stationary velocity statistics. For large scale properties this model is of little use, but it is a good approximation to the very short time behavior of a turbulent flow. Processing tracks from this model yielded the solid curve shown in Fig. A.9.

The deviation between the solid line in Fig. A.9 and the value for $t \to 0$ represents the bias introduced by fitting a second order polynomial over that trajectory time segment. In the final data analysis of the measured trajectories, we corrected for this bias by adding the modeled deviation onto the measured acceleration for that length of trajectory segment (Fig. A.7). Results both with and without this correction are given in Section *A.1.7*.

Determining the dissipation from the acceleration autocorrelation function.

The prevalence of turbulence research on flows with large mean velocities where Taylor's hypothesis may be applied can lead to the misconception that ϵ is always fairly simple to

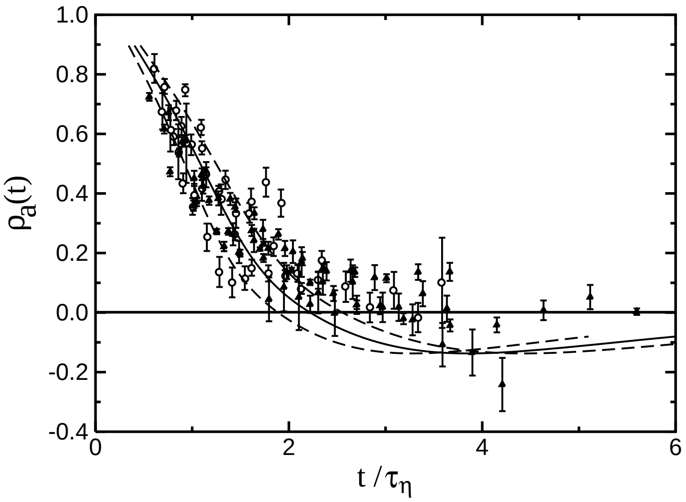

Figure A.10: Acceleration autocorrelation function for $250\ \mu\mathrm{m}$ particles (circles); $460\ \mu\mathrm{m}$ particles (triangles); DNS data Yeung & Pope (1989) (solid line); and estimated errors (dashed lines).

determine. In flows with zero mean velocity, which makes them attractive for Lagrangian studies, this is not the case.

We determine the mean dissipation from $\epsilon = \tilde{u}^3/L$, where $\tilde{u}$ is measured, and L is assumed to be determined by the geometry of the flow and independent of Reynolds number. To determine the value of L, we used a method Pope (1997) that relies on the autocorrelation function of an acceleration component, defined for the *y* compontent as

$$\rho_a(t) = \frac{\langle a_y(t_0) a_y(t_0 + t) \rangle}{\langle a_y^2 \rangle}. \tag{A.22}$$

Yeung and Pope Yeung & Pope (1989) found from direct numerical simulations that, up to $R_\lambda = 93$, $\rho_a(t)$ passed through zero at $t = 2.2\tau_\eta$. For times smaller than this, the curves were essentially independent of Reynolds number when scaled by the Kolmogorov timescale. Yeung has recently found agreement with this at $R_\lambda = 140.$ Yeung (1997) By measuring $\rho_a(t)$ for our data and scaling time so that it fell onto the known curve from Yeung and Pope, Yeung & Pope (1989) we were able to determine the Kolmogorov timescale, τ_η, and from this, ϵ and L.

Figure A.10 shows the acceleration autocorrelation function measured for the *y* compontent of all data sets with more than 10,000 tracks. The solid line is from Yeung and Pope Yeung & Pope (1989) at $R_\lambda = 93$. For each experimental run, $\rho_a(t)$ was determined by fitting second order polynomials to sections of each track separated by time t, multiplying the fitted accelerations and averaging over all tracks. Each autocorrelation function was normalized by the corrected acceleration variances given in Section *A.1.7.* The time span used for the quadratic fits was chosen to be the time when the measured acceleration variance reached twice the extrapolated value for the sets with $460\ \mu\mathrm{m}$ particles and three times the extrapolated value for the sets with $250\ \mu\mathrm{m}$ particles (see Fig. A.7). The results were surprisingly insensitive to the exact choice of time span, suggesting that the acceleration measurement errors were sufficiently uncorrelated. The error bars were determined as before by dividing each data set into segments and calculating the standard deviation between the segments divided by the square root of the number of segments. This made the incorrect assumption of Gaussian errors, so the errors were somewhat underestimated.

The observed collapse of the experimental data was obtained with the assumption that there was one constant length scale L in the flow. By using an arbitrary value for L, the dissipation can be determined from $\epsilon = \tilde{u}^3/L$ and thus τ_η. The ratios between the τ_η's for various data sets obtained in this manner were correct even though the overall magnitude of τ_η was arbitrary. Scaling the time axis for each data set by τ_η collapsed the data of all runs including both particle sizes, as shown in Fig. A.10.

To determine the actual value of L, the time axis for all data sets together was scaled again to provide the best fit to the DNS results. This was done by a least squares fit to the data for $\tau_\eta < 2$. The value of L obtained from this least squares fit was $(0.21 \pm 0.06)\ \mathrm{m}$. This value is very reasonable, as it is close to the diameter of the disks $(0.203\ \mathrm{m})$. We estimated the error in L by choosing limits that seemed visually reasonable. The dashed lines in Fig. A.10 reflect the error estimates in L. They were found by scaling the simulation results by the amount corresponding to the error in L. The deviation between our data and the simulations for $\tau_\eta > 2$ is expected. As the Reynolds numbers of the simulations increased, the negative excursion above $2.2\tau_\eta$ was continuously decreasing. Yeung & Pope (1989) For the high Reynolds numbers in this experiment, the negative excursion should be very small and should extend to much longer times.

A.1.7 Results

Figure A.11(A) shows $\nu^{1/2}\langle a_i^2\rangle$, where $\langle a_i^2\rangle$ is the variance of a single acceleration component, as a function of velocity scale for all of the data sets without applying the correction for under-resolved trajectories (Section *A.1.6*). The data clearly shows a power law. The prediction for the variance of fluid particle acceleration components from Kolmogorov's hypothesis is

$$\langle a_i^2\rangle = a_0 \epsilon^{3/2} \nu^{-1/2}. \tag{A.23}$$

Using $\epsilon = \tilde{u}^3/L$, this can be rewritten

$$\nu^{1/2}\langle a_i^2\rangle = a_0 L^{-3/2} \tilde{u}^{9/2}. \tag{A.24}$$

The scaling exponent of the data shown in Fig. A.11(A) is in good agreement with the Kolmogorov prediction of $\tilde{u}^{9/2}$ shown by the solid line.

Figure A.11(B) shows the same data with the under-resolved trajectory correction applied. The correction raised the measured acceleration variance by amounts ranging from 3% up to 22%, depending on the typical number of Kolmogorov timescales over which the particles were tracked. The agreement with Kolmogorov scaling is significantly improved. Over three orders of magnitude the scaling of the data with the smallest errors (the *y* data) is nearly indistinguishable from the predicted scaling. We emphasize that the agreement with Kolmogorov scaling requires only the assumption of a constant

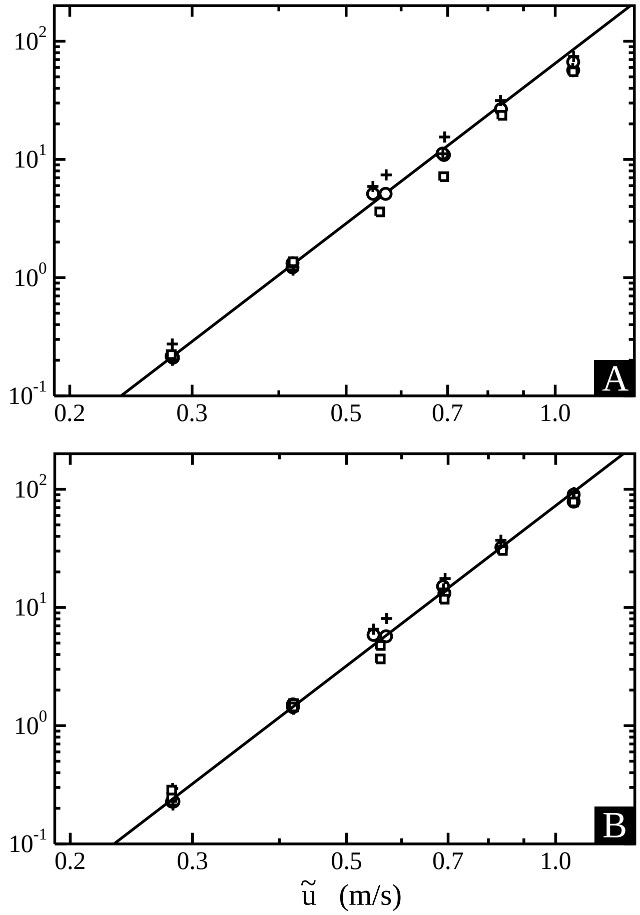

Figure A.11: Acceleration variance scaling; (A) raw data and (B) corrected for underestimation of accelerations. *y* trajectories (250μm (◯) and 450 μm (□)) and *x* trajectories (250 μm (+)). The solid line is the Kolmogorov $\tilde{u}^{9/2}$ prediction.

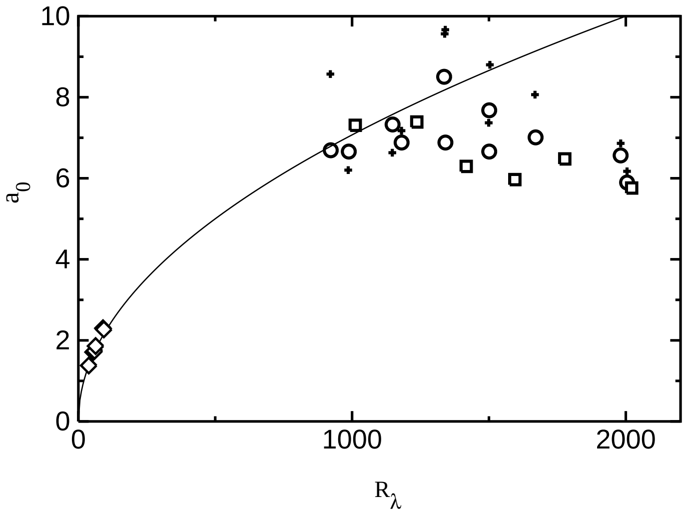

Figure A.12: Compensated acceleration scaling. *y* trajectories ($250\ \mu\mathrm{m}$ (◯) and $450\ \mu\mathrm{m}$ (□)) and *x* trajectories ($250\ \mu\mathrm{m}$ (+)). DNS data from Yeung and PopeYeung & Pope (1989) (◇).

length scale, L, and is not affected by the large uncertainty in the value of L determined in Section *A.1.6*. It is interesting to note that at the highest Reynolds number the rms acceleration is about $300\ \mathrm{m/s^2}$, or more than 30 times the acceleration of gravity.

Figure A.12 shows a_0 calculated from Eq. (A.24) for the data in Fig. A.11B. Also shown is the direct numerical simulation data from Yeung and PopeYeung & Pope (1989) and the extrapolation of the $R_\lambda^{1/2}$ scaling they observed. Yeung's recent simulations continue to follow the $R_\lambda^{1/2}$ trend up to $R_\lambda = 200$ where $a_0 = 3$.Vedula & Yeung (1999) Particle settling problems prevented us from studying lower Reynolds numbers and directly comparing with the simulation results.

The central feature of Fig. A.12 is that the measured value of a_0 is approximately independent of Reynolds number, particularly for the lower noise *y* data for both particle sizes. From this we conclude that for $R_\lambda \gtrsim 1000$, a_0 has turned over from the $R_\lambda^{1/2}$ scaling previously observed in DNS to showing relatively good agreement with the Kolmogorov ('41) prediction that a_0 is constant. Modest deviations from the Kolmogorov ('41) scaling could lie within the scatter of the data. Further measurements, particularly of the higher moments of the acceleration distribution will be necessary to gain insight into what effects intermittency may have on Lagrangian acceleration statistics.

When interpreting Fig. A.12, it is important to recognize that there is a significant uncertainty in the overall scaling of the vertical axis for the measured data which results from the uncertainty in the mean dissipation, or equivalently from the uncertainty in L. This does not affect the conclusion that a_0 is independent of Reynolds number, but it does affect attempts to interpolate between our data and the DNS data. No clear anisotropy between the *x* and *y* measurements can be identified, although the larger measurement errors in the *x* data make this difficult to determine.

The value of the Kolmogorov constant, a_0, is read from Fig. A.12 to be 7.0 ± 1.0,

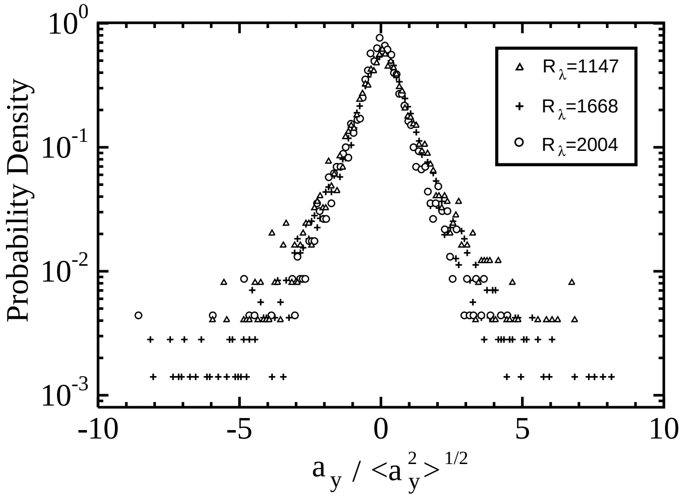

Figure A.13: Probability density function for the *y* acceleration normalized by the rms acceleration (from Fig. A.11B).

where this uncertainty reflects fluctuations between data sets. In addition there is the larger uncertainty in the value $L = 0.21 \pm 0.06$ m which entered into the calculation of each a_0. When added in quadrature these together produce an uncertainty of $\pm 45\%$. Thus the final value of a_0 was found to be 7 ± 3.

Surprisingly, we observed very little difference between the data for the $250\ \mu\mathrm{m}$ particles and the $460\ \mu\mathrm{m}$ particles. This observation supports the hypothesis that the particles, with diameters ranging from 5 up to 25 times the Kolmogorov microscale, were acting like fluid particles to within the accuracy of the measurements. The slight decrease of the data at the highest Reynolds number might be a particle size effect, but this is unclear. The insensitivity to particle size may be related to the fact that the pressure term in the Navier-Stokes equation is dominant in determining the fluid particle acceleration at large Reynolds numbers.

Figure A.13 shows the PDF of the measured *y* acceleration normalized by the rms acceleration from Fig. A.11B for runs 4, 9, and 11. Tracks are included in the PDF if their tracking time is more than 60% of the maximum tracking time. The logarithmic plot shows exponential tails, suggesting intermittency. No clear deviation between the different Reynolds numbers is observed, particularly when one recognizes the uncertainties in the rms values used for normalization. Although values of the flatness and higher order moments are not reported due to limited statistics and sensitivity to the identification of spurious tracks, the flatness is clearly larger than the Gaussian value of 3. The rare events, with accelerations up to 8 times the rms were not spurious. For example, the track shown in Fig. A.3 is at $R_\lambda = 1668$ and has $a_y / \langle a_y^2 \rangle^{1/2} = 8.2$ which is far in the tail of the plotted PDF.

A.1.8 Conclusions

In this paper we presented experimental particle tracking measurements in a flow between counter-rotating disks for Taylor Reynolds numbers $900 < R_\lambda < 2000$, an order of magnitude higher than previously possible. We recorded particle tracks by imaging tracer particles onto a position sensitive photodiode, and obtained data with sufficient spatial and temporal resolution to measure accelerations. A primary conclusion is that experimental measurements of Lagrangian quantities at these Reynolds numbers are possible. We have developed a model for correcting particle tracking velocity measurements when residence times are unavailable. We reported results for the acceleration variance which are in good agreement with Kolmogorov's ('41) scaling predictions. This data represents the first validation of the expectation that at large Reynolds numbers Lagrangian accelerations can be described by Kolmogorov ('41) scaling. The scatter in the data does not allow conclusions about possible intermittency corrections to the Kolmogorov ('41) scaling. The value of the Kolmogorov constant for the acceleration variance was found to be 7 ± 3.

A.2 New interpretations

The measurements presented in this paper represent a new measurement technique. As a result, the interpretation of the data had several steps which were justified primarily by plausibility and internal consistency rather than having the external justification that usually develops as a technique matures. Our recent measurements with silicon strip detectors have yielded significantly higher resolution data that has led us to a new interpretation of some of these results.

There are two primary sources of the problems in the interpretation that was made of this data. The first lies in the justification of the extrapolation procedure using a stochastic model in section A.1.6. Larger data sets of more precise data demonstrate that the non-gaussian acceleration distribution that is already visible in Fig. A.13 is dramatically different from the gaussian acceleration distribution assumed by the stochastic model. In an intermittent cascade, the rare events in the tails of the acceleration distribution have short time scales, and as a result the stochastic model significantly underestimates the magnitude of the correction. The issues are made clear in Fig. A.14 which contains four plots of the measured acceleration variance as a function of fit length. The top two are from the position sensitive photodiode data, and the other two are from the silicon strip detector data with two different tracer particle sizes. As shown in section 4.8, the $46\ \mu\mathrm{m}$ particle data is not significantly different from true Lagrangian trajectories, so for times greater than $0.5\tau_\eta$ this can be considered the “true” curve. With this information we can determine that the correction due to averaging over particle trajectories is much larger than is shown in Fig. A.9.

The second source of problems that compounds the issues above is that the method used to estimate the energy dissipation in section A.1.6 has a larger error than originally estimated. The reason for this will be discussed below, but the effect is that the Kolmogorov time scale used in Fig. A.9 was too large and this compounds the stochastic model underestimate of the error due to fits averaging over the trajectory. The normaliza-

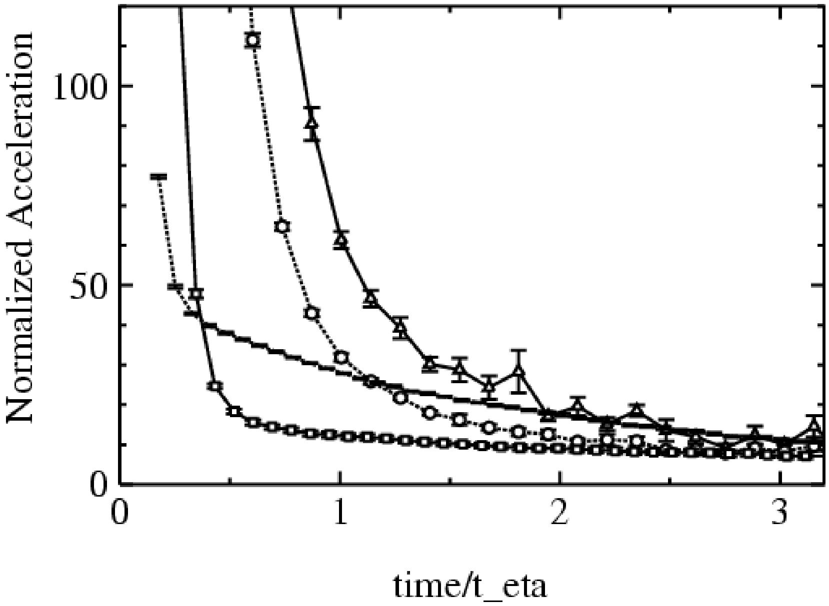

Figure A.14: Comparison of the acceleration variance as a function of fit length for the position sensitive photodiode and silicon strip detector data. The top two data sets are from the position sensitive photodiode data for 250 $\mu\mathrm{m}$ particles: all the data (triangles), and with a cut of reduced $\chi^2 < 10$ (circles). The other two are from the silicon strip detector data. The upper one is for 46 $\mu\mathrm{m}$ particles, and the lower one (squares) is for 467 $\mu\mathrm{m}$ particles. The Kolmogorov time used in this plot is the one determined with the position sensitive photodiode data. The position sensitive photodiode data is at 7.5 Hz disk frequency and the silicon strip detector data is at 7.0 Hz, but it is found that the shape of these curves changes very little with disk frequency in this range of Reynolds number.

tions used in Fig. A.14 use the energy dissipation from this appendix which are known not to be correct, but this allows direct comparison with the plots in this appendix.

The result of these two problems is that the extrapolations to determine the value of the acceleration variance described in section A.1.6 do not provide an adequate measurement. The beautiful power law in Fig. A.8 is created by an unfortunate combination of measurement error and actual particle trajectories. The value of the χ^2 cutoff used in section A.1.6 to eliminate the effect of multiple particles was chosen to minimize the "contribution from measurement error" which we now know contained some actual accelerations. The χ^2 cutoff being too stringent was part of the cause of the acceleration autocorrelation function giving too large a value for the Kolmogorov time scale and hence the dissipation. We have found that we are not yet able to adequately resolve the acceleration autocorrelation function even with the silicon strip detector data, and so the attempt to measure the dissipation from it was misguided.

Although the actual value of the acceleration variance we found was incorrect, it turns out that this does not affect the primary conclusion of the paper–that the acceleration variance is well described by the Kolmogorov scaling in this range of Reynolds number. The reason for this is that while the reported variance excludes part of the true accelerations, it excludes a constant fraction. This can be seen from Fig. 4.10 where we see that the actual acceleration variance versus fit length for the large Reynolds numbers are nearly universal curves when scaled by Kolmogorov variables. The method used in this paper consistently used the value of this curve at about $6\tau_\eta$ ($3\tau_\eta$ in Fig. A.14) as the true acceleration variance. Across the range of Reynolds numbers reported in the paper, this value scales almost exactly as the true acceleration variance does. A fortunate combination of factors also resulted in the reported value for the Kolmogorov acceleration constant being in the correct range. The errors in the energy dissipation and the acceleration variance cancelled each other so that the value of $a_0 = 7 \pm 3$ agrees with more recent measurements within the error estimate.

In the paper, we found it surprising that the values of the acceleration variance for the $250\ \mu\mathrm{m}$ and $450\ \mu\mathrm{m}$ particles were nearly the same, and it turns out that the strip detector finds them to be significantly different. This error occurred because the extrapolation to large fit times is not very sensitive to the difference between the two particle sizes. As seen in Fig. A.14, an extrapolation of the curves for two particle sizes can easily give the same result when the true values at zero fit time are very different.

In conclusion, more precise measurements have revealed that the self-consistent data analysis used in this paper had some flaws. These have their roots in the error in the measurement of the dissipation and in the erroneous assumption of gaussian accelerations in the Monte-Carlo model. The data was not of sufficient quality to convincingly support all of the conclusions that were drawn; however, it turns out that except for the particle size dependence, the conclusions are still correct.

Appendix B

Digital Detector Controller

This appendix describes the controller board which produces the signal sequences necessary to read out the Viking chips. This board contains the master clock with which all the data acquisition equipment is synchronized. The board is housed in a gray box, and is easily identified by ribbon cables connecting it to the master computer and the repeater cards. A photograph of the detector controller is shown in Fig. B.1.

B.1 Components

The central component of the board is an Altera Programmable Logic Array (PAL), part number EPM7160ELC84-10. The pinout for this chip is shown if Fig. B.3. The rest of the board consists only of a clock, a delay line, line drivers, a set of dip switches, and connectors:

- One crystal oscillator–20 MHz. Pinouts are in the Digikey catalog. When viewed from the bottom they are: (clockwise) 1 NC, 7 Gnd, 8 Output, 14 +V.
- One delay line, Dallas Semiconductor part number DS1010, which is used to adjust the phase of the clock sent to the A/D boards to that the A/D converters sample in the correct phase with serial data stream from the detectors.
- Five differential line drivers, part number DS26C31TN from National Semiconductor, which turn the signals on the board into the low voltage differential signals expected by the repeater card.
- One set of inverting line drivers which drive the BNC output lines. We originally tried a Texas Instruments part number SN74AS1034AN, but it could not drive the 50Ω terminated lines. The solution was to piggyback a set of bipolar transistors and resistors onto the line driver to provide sufficient current.

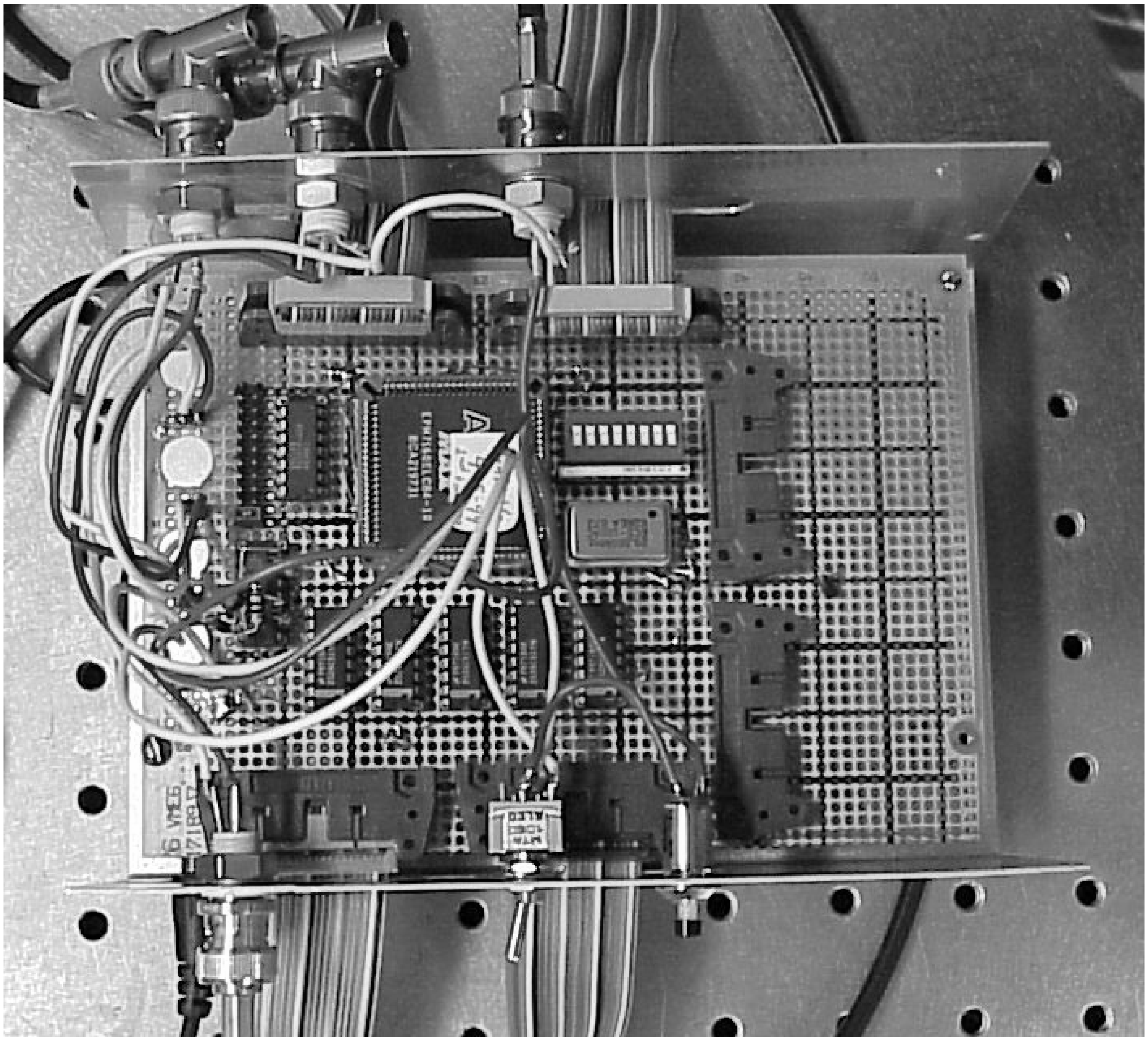

Figure B.1: Photograph of the detector controller

B.2 Functionality

At the heart of the circuit is a counter which controls the readout of each frame (a frame is one complete readout of all channels of the detector). At specified values of this counter, the various signals are initiated that control the Viking multiplexer and acousto-optic modulator (AOM) that pulses the illumination laser. There are three additional functions the circuit fulfills. It contains elements that read parameters sent by the master computer. It has logic that controls triggering of the detection system. It also counts the number of triggers so that the desired number of frames are read out. Below is a brief description of each function.

All of the details are available by looking at the Max+plus II files that are used to program the Altera PAL chip. These are available in my home directory on the LNS Windows NT network under `z:\gav3\control6`. The main module is `control6.gdf`. They are also on a floppy disk in the magnetic media drawer in B16. The graphical program code and examples of the timing of input and output signals in shown in Figs. B.4–B.12. If you need to modify the PAL programming, you will need to use the Altera programmer which is in the computer room on the second floor of Wilson lab. We have an old version of Max+plus II (8.3) and the software guard for it. An updated version of Max+plus II can now be downloaded from http://www.altera.com. The person in LNS who knows all about such things is Chris Bebek.

B.2.1 Viking control signals

The signals required to control the Viking (VA1) are documented on the IDE AS web pages and in the Viking controller and hybrid documentation books. The primary signals to keep track of are the shift_in, hold, and clk. When hold goes high, the sample and hold amplifiers on the Viking are latched. A pulse on shift_in initiates readout of the multiplexer. The values of each channel are then read out on rising edges of the clk. The clk is only active during the readout of the 128 channels.

B.2.2 Setting controller registers

The master computer sets the various parameters needed by the detector controller through the computer's digital I/0 board (PCL-726). The information is passed over the computer digital output to the card. The pinouts are given in the inputs section below. Of the 16 computer digital output lines, the top 4 are dedicated control lines. The lower 12 lines are a bus to set the registers on the controller. The lower 8 lines (1-8) contain an eight bit word. The next 4 lines (9-12) contain the address of the register to be set. When pin 13 is high the addressed register is set to the input word. When pin 13 is brought low, the value is stored. The register values are:

- Address 0: period, low 8 bits. True readout period is (period+3) clock cycles
- Address 1: period, high 3 bits

- Address 2: frame, low 8 bits. Sets the number of number of triggers sent to the A/D boards and hence the number of frames acquired
- Address 3: frame, high 8 bits
- Address 4: aom_on, low 8 bits. Sets the clock cycle when the aom turns on
- Address 5: aom_on, high 3 bits
- Address 6: aom_off, low 8 bits. Sets the clock cycle when the aom turns off
- Address 7: aom_off, high 3 bits

An example of the signals that set the controller registers is in Fig B.10. The number of bits used in each of these parameters is set by the size of the counter it is compared to. The original design was for a smaller chip (EPM7128ELC84-7) and so the counters and registers were made as small as possible to fit on the chip. Now there is more space on the EPM7160ELC84-10, but I have left the program the same since other aspects are more likely to need to be expanded.

B.2.3 Trigger logic

The controller was originally intended to trigger when a photodetector recorded that a particle was in view. This part of the system has been changed, so that the detector is continuously triggered with a signal generator. In case it is to be revived in the future, here is a brief outline of the trigger logic. As with most computer logic, the best documentation is the actual code. The trig_in signal comes either from a trigger photodiode or from a pulse generator. If this is high just before readout, and it was not high just before the last readout, then this is the beginning of an event and triggers should be sent to the A/D converters to readout the desired number of frames. After the trigger counter returns that enough triggers have been sent to the A/D cards, the hold_trigger signal is set high and sending triggers is disabled. This signals the master computer that acquisition is complete. When the master computer is ready for the next sequence, it sets the computer_busy line high and then low again. This allows the master to be sure that no more triggers are sent until the slave computers are rearmed to accept triggers. After the computer_busy line goes low, readout is initiated again the next time the trig_in goes high.

B.2.4 Trigger counter

The trigger counter is a 16 bit counter that counts the number of triggers that have been sent to the A/D converters and sets a flag when the correct number have been sent.

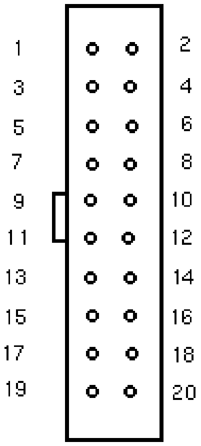

Figure B.2: Pin numbers for the 20 pin connector used for inputs and outputs from the detector controller. This view is of the male connectors on the controller board.

B.3 Connectors

B.3.1 Inputs

There are two input connectors: the BNC trigger input and the 20 pin ribbon cable connector from the master computer digital out. The 20 pin cable connector as seen from the top of the board is shown in Fig. B.2, and its pinout is

- Pins 1-8 = Data lines
- Pins 9-12 = Address lines
- Pin 13 = Address enable
- Pin 14 = Fake trigger
- Pin 15 = Clear
- Pin 16 = Computer Busy
- Pins 17-18 = Gnd
- Pins 19-20 = Not connected to controller card(Computer +5, +12 V).

B.3.2 Outputs

The outputs from the controller board are

- 20 pin connector to the computer digital input
- Four 20 pin connectors carrying differential signals to the repeater cards

- Trigger signal to the A/D boards (BNC)
- Clock signal to the A/D boards (BNC)
- AOM signal to AOM amplifier (BNC)

The connector to the master computer digital input is a 20 pin ribbon cable connector even though it only carries one signal. (Fig. B.2). Its pinout is

- Pins 1-15 = NC
- Pins 16 = hold_trigger
- Pins 17-18 = Ground
- Pins 19-20 = Not connected to controller card(Computer +5, +12 V)

The connectors to the repeater cards are also 20 pin ribbon cable connectors. Currently there are 4 of these connectors on the board enabling control of 4 detectors. More could be added by installing more line drivers and connectors. These connectors are also shown in Fig B.2, and their pinout is

- Pin 1 = areset*
- Pin 2 = areset
- Pin 3 = dreset
- Pin 4 = dreset*
- Pin 5 = hold*
- Pin 6 = hold
- Pin 7 = clkout
- Pin 8 = clkout*
- Pin 9 = shift_in*
- Pin 10 = shift_in
- Pins 11-16 = NC
- Pins 17,18,20 = Ground
- Pin 19 = Vcal (Not Used)

B.3.3 Dip switch and jumper settings

The jumper just below the PAL chip is used to set the delay on the clock output line. This allows the phase of the A/D sampling to be adjusted relative to the Viking readout. The jumper sets the delay in units of 10 ns. The pin at the right, next to G0, is no delay. H1 is 10 ns and so on until H0 is 100 ns. The dip switches at the top of the PAL were used on a previous version of the controller. Currently they are not connected.

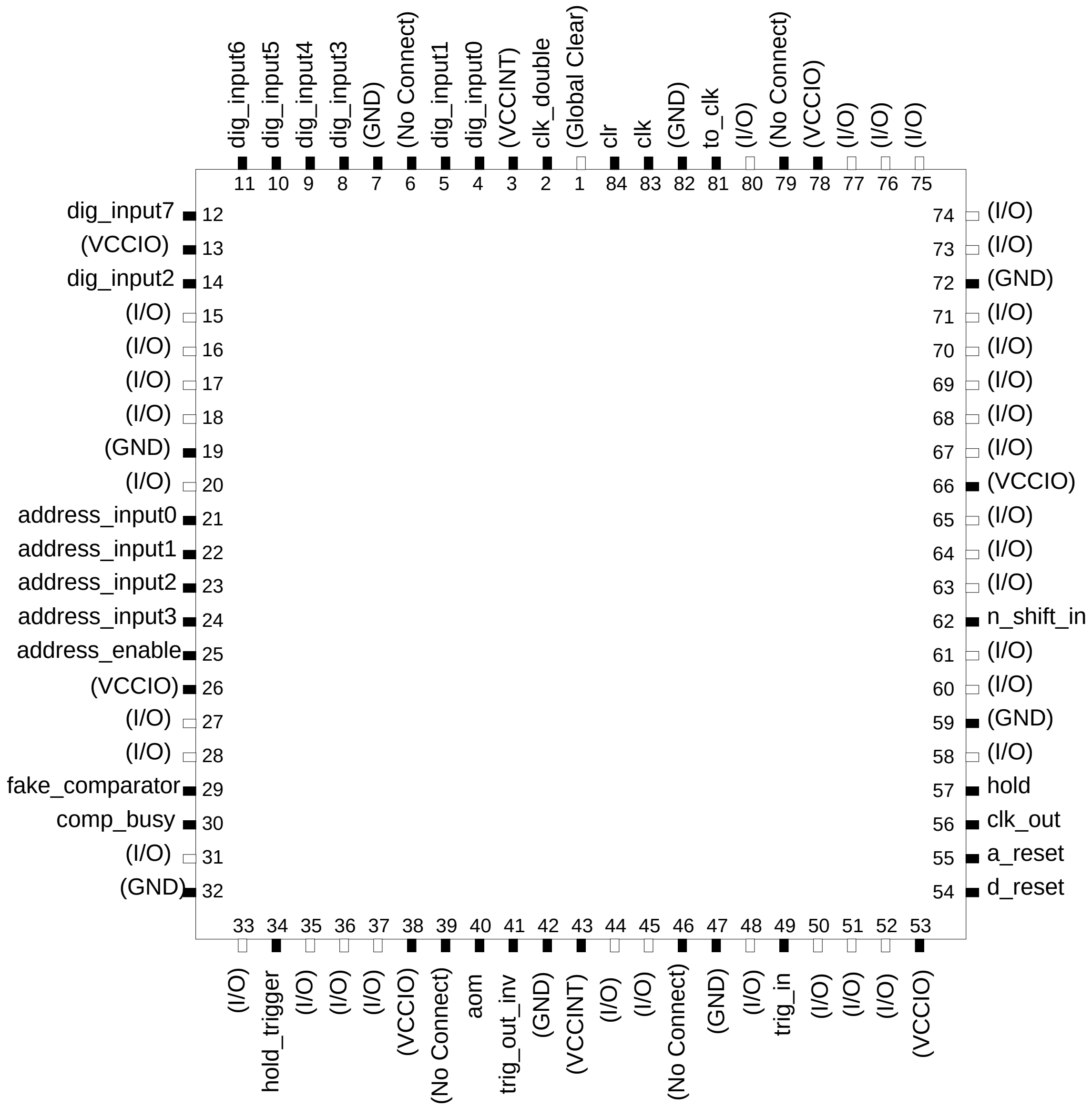

Figure B.3: Pinout of the Altera EPM7160ELC84 chip.

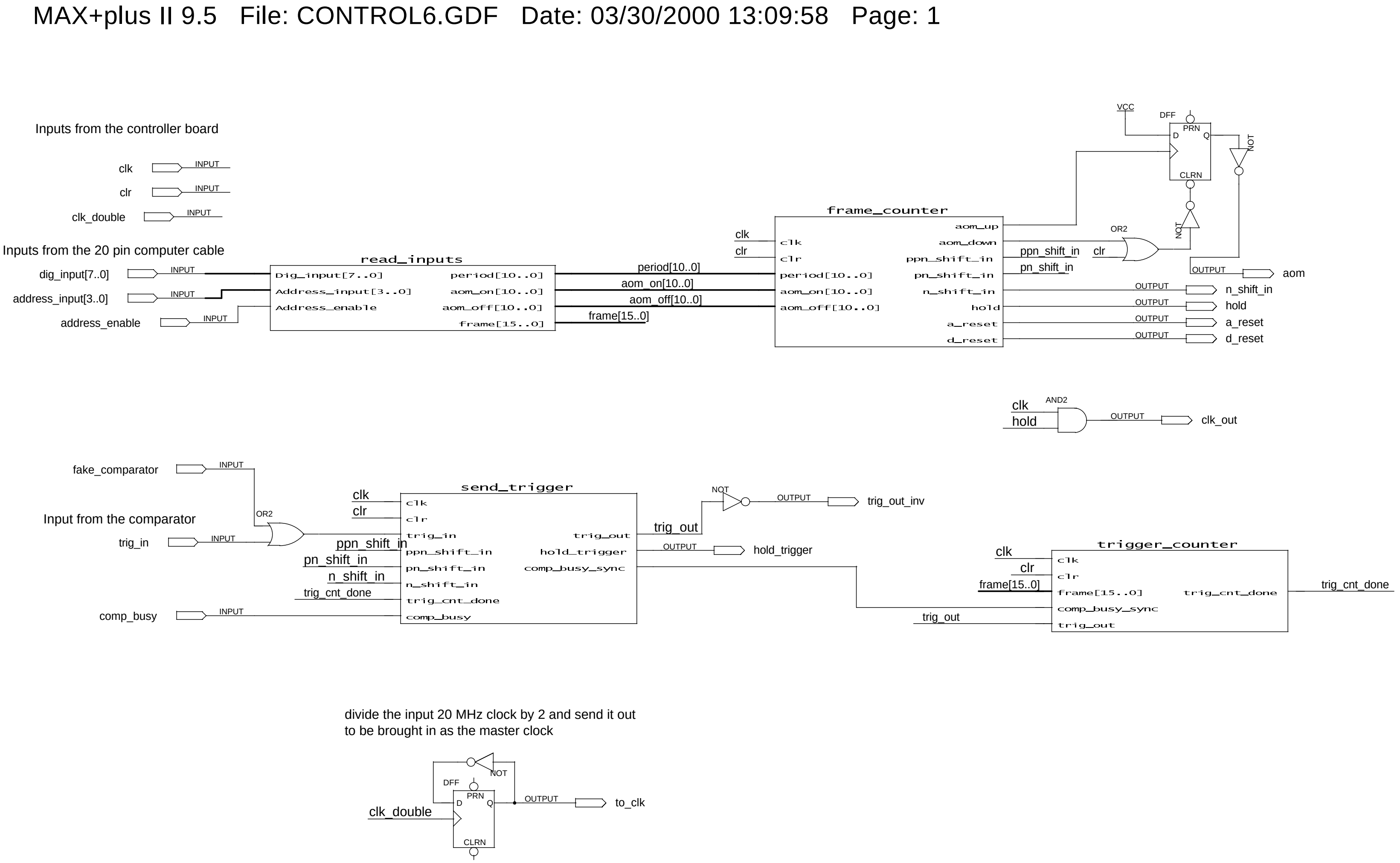

Figure B.4: Altera graphical design file (.gdf) for the main module of the detector controller.

MAX+plus II 9.5   File: READ_INPUTS.GDF   Date: 03/30/2000 13:17:12   Page: 1

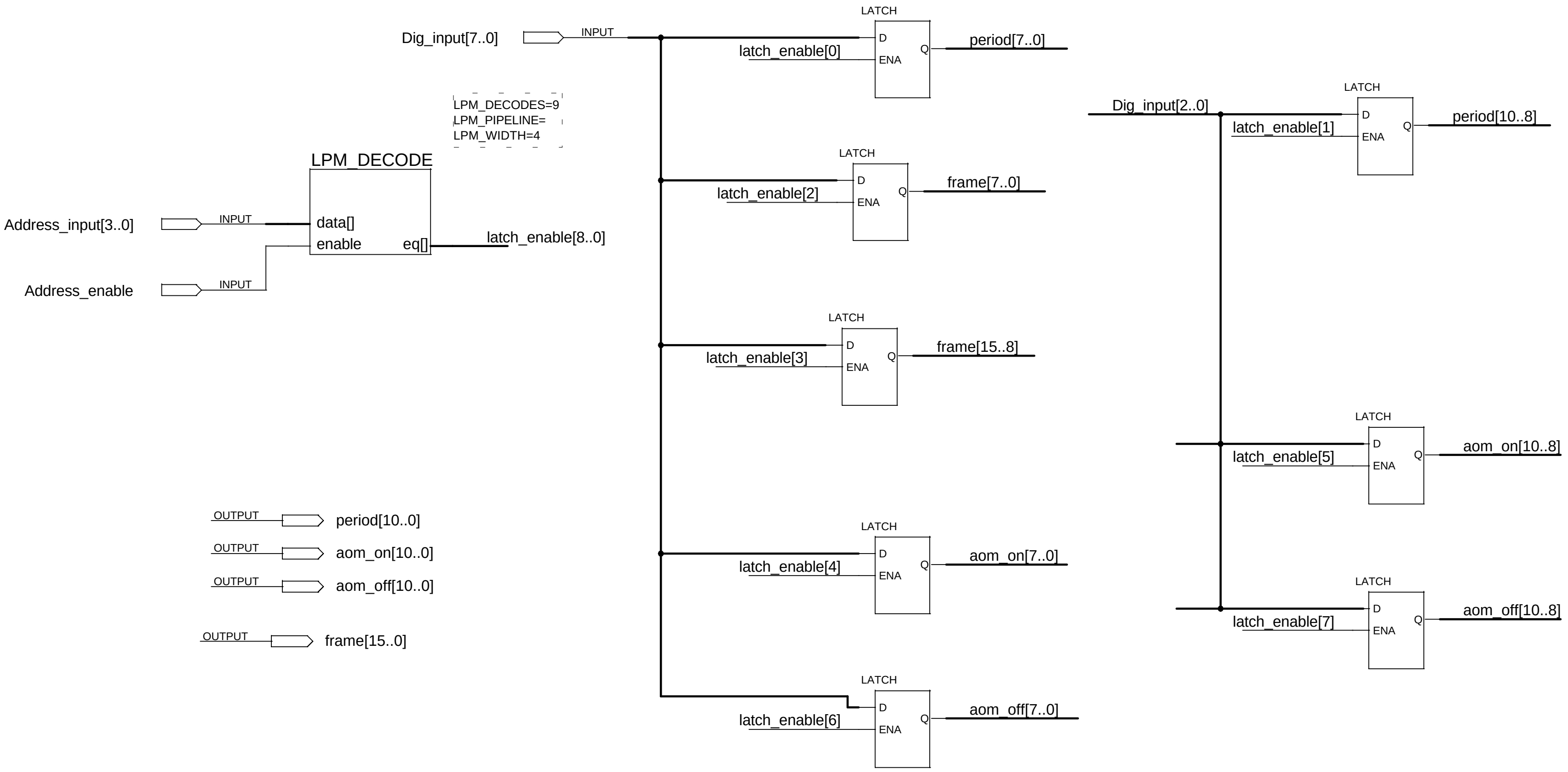

Figure B.5: Altera graphical design file (.gdf) for the module that reads inputs from the master computer digital output.

MAX+plus II 9.5 File: FRAME_COUNTER.GDF Date: 03/30/2000 13:20:13 Page: 1

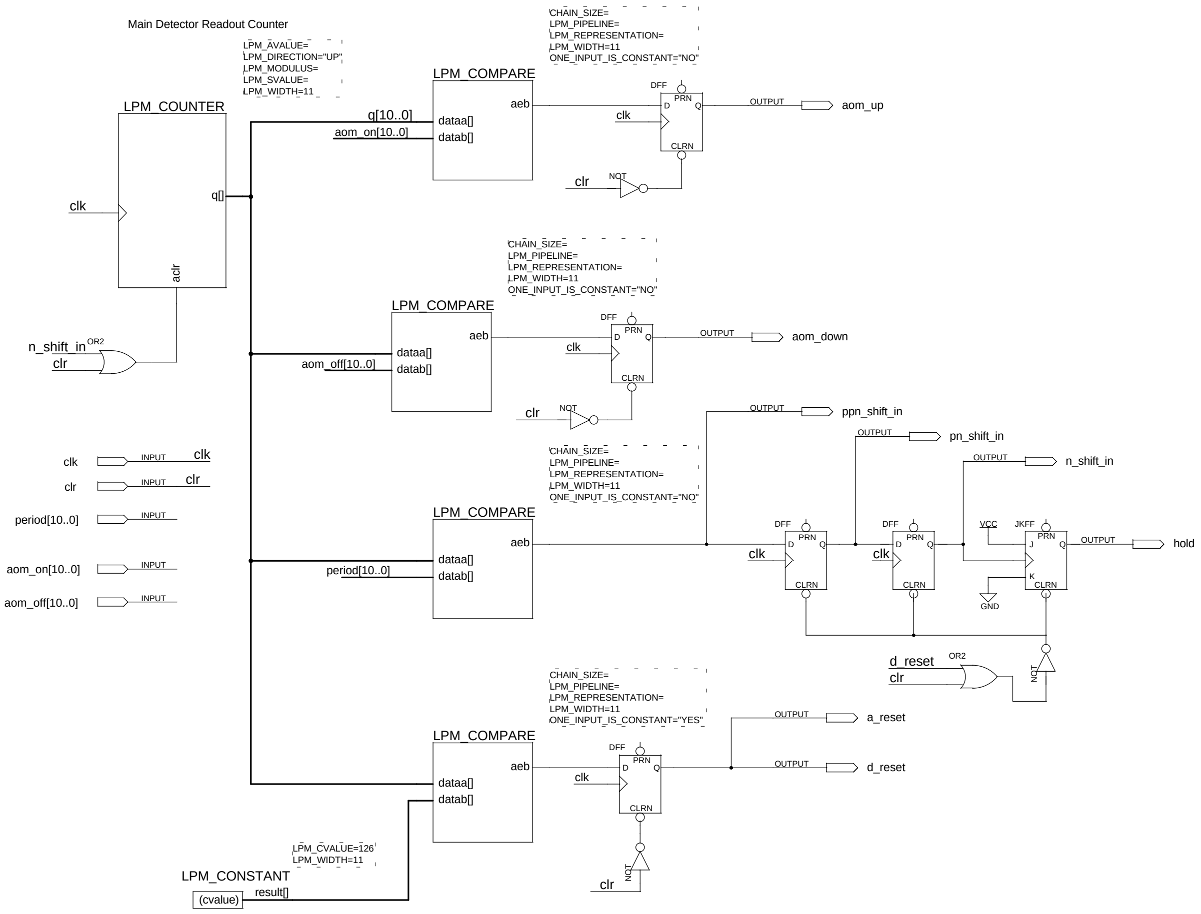

Figure B.6: Altera graphical design file (.gdf) for the module that contains the primary counter that sequences the signals to control the Vikings.

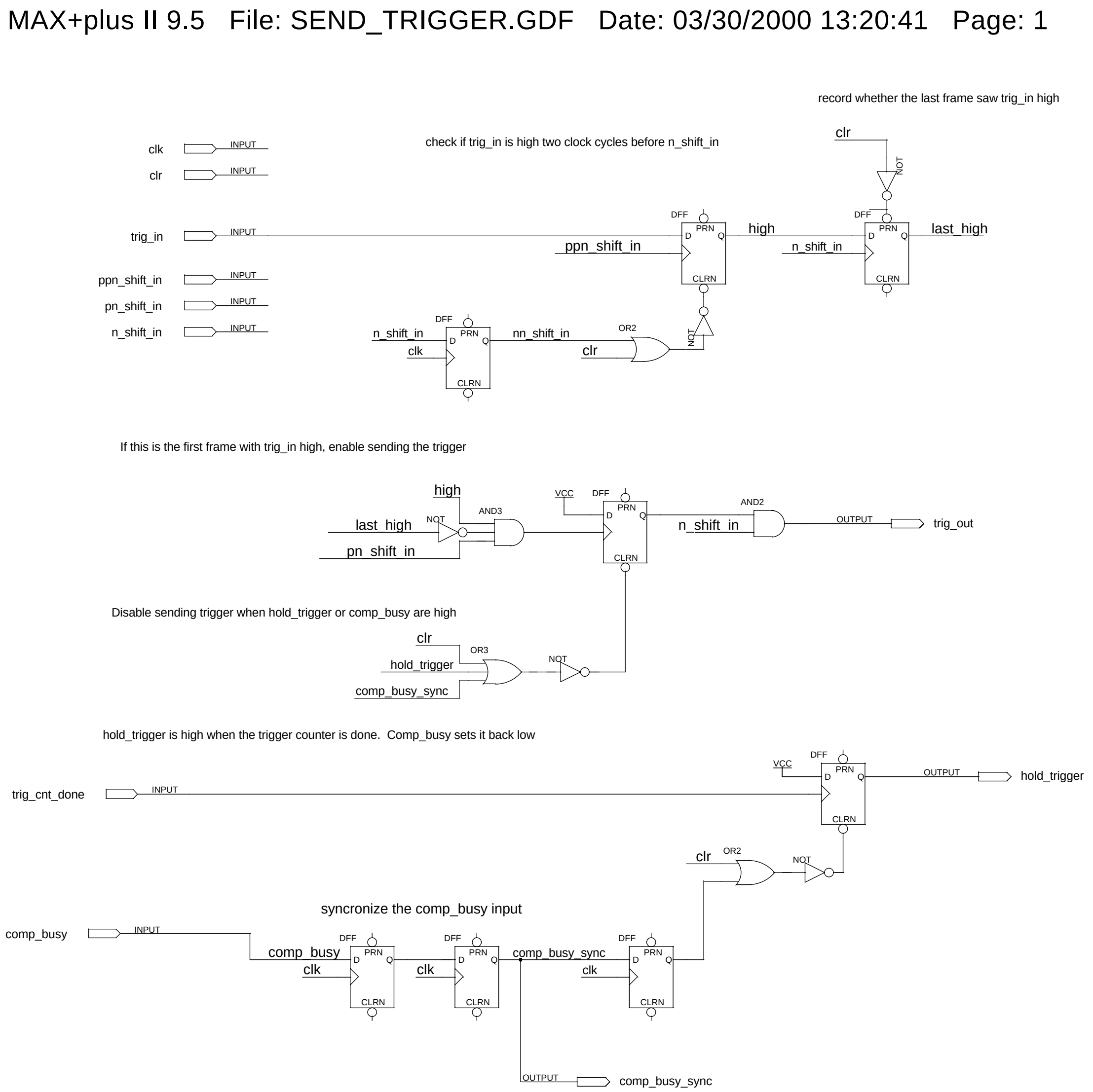

Figure B.7: Altera graphical design file (.gdf) for the module that controls sending of triggers to the A/D cards.

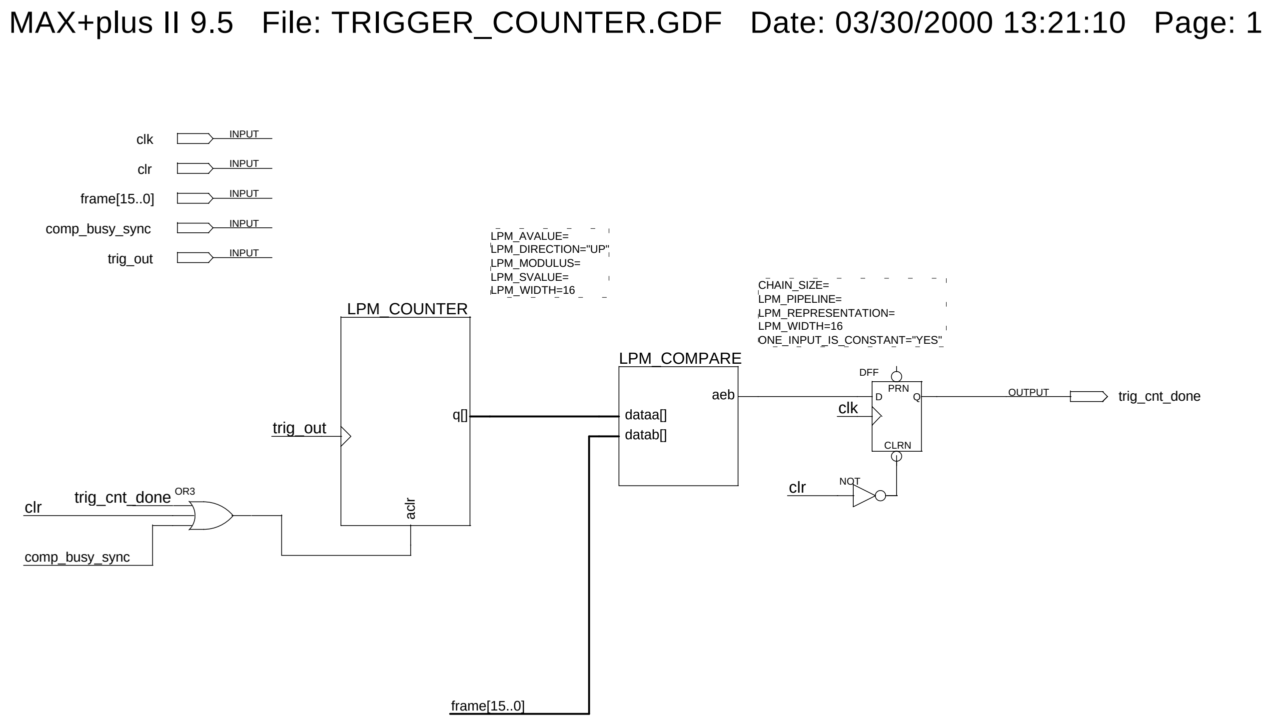

MAX+plus II 9.5 File: TRIGGER_COUNTER.GDF Date: 03/30/2000 13:21:10 Page: 1

Figure B.8: Altera graphical design file (.gdf) for the module that counts the number of triggers sent to the A/D cards.

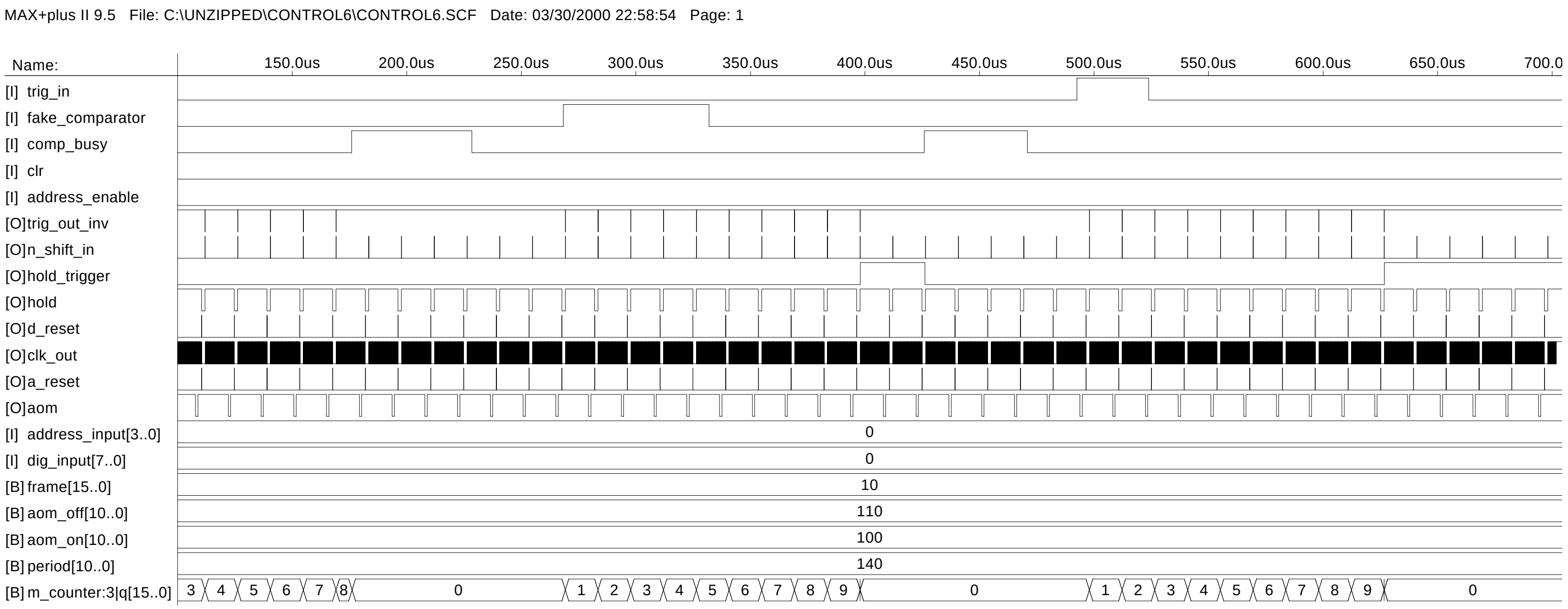

Figure B.9: Altera simulator channel file (.scf) for the detector controller which shows the time traces of all signals used by the controller. In particular, this shows how the trig_in, comp_busy, hold_trigger and trig_out_inv are used.

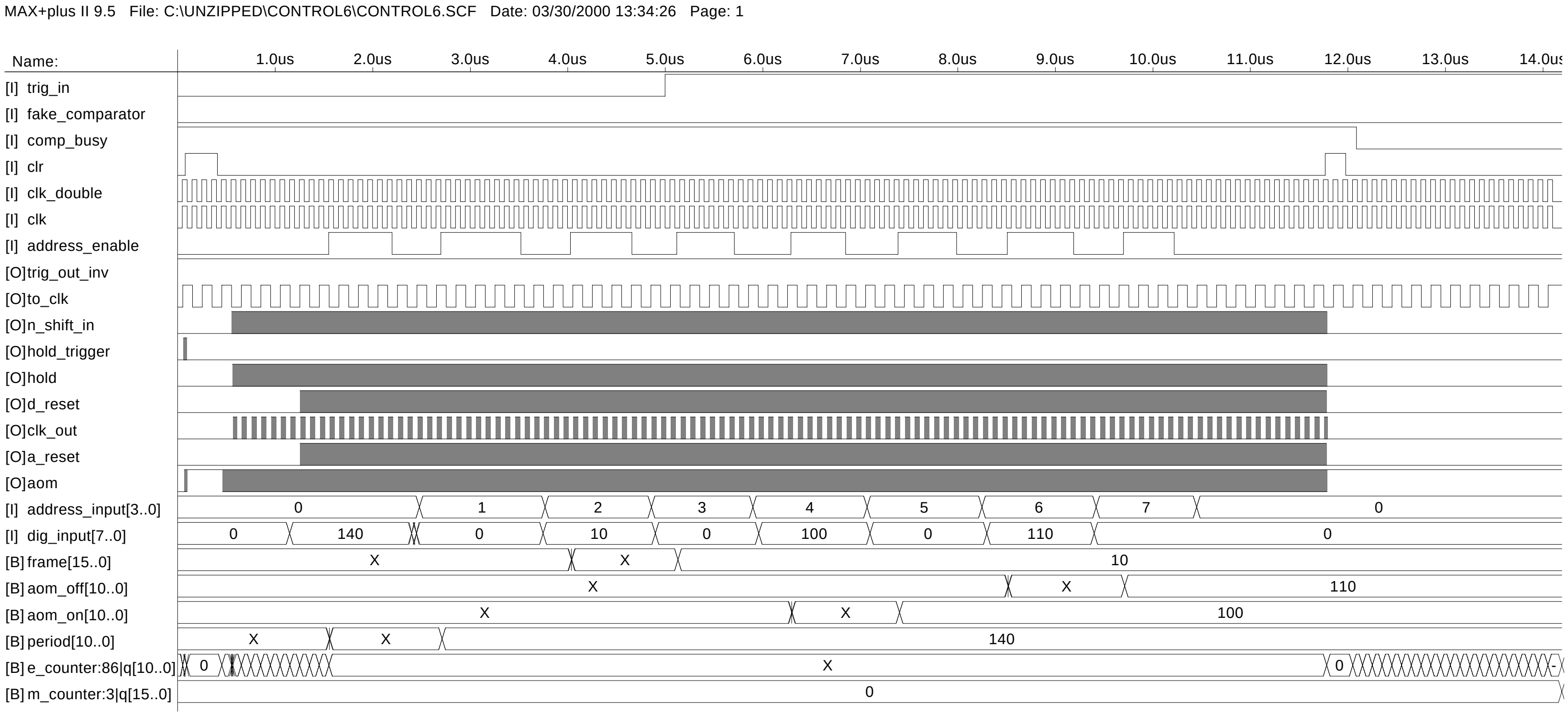

Figure B.10: This is part of the Altera simulator channel file (.scf) for the detector controller. It shows the signals that initialize the registers that set readout parameters.

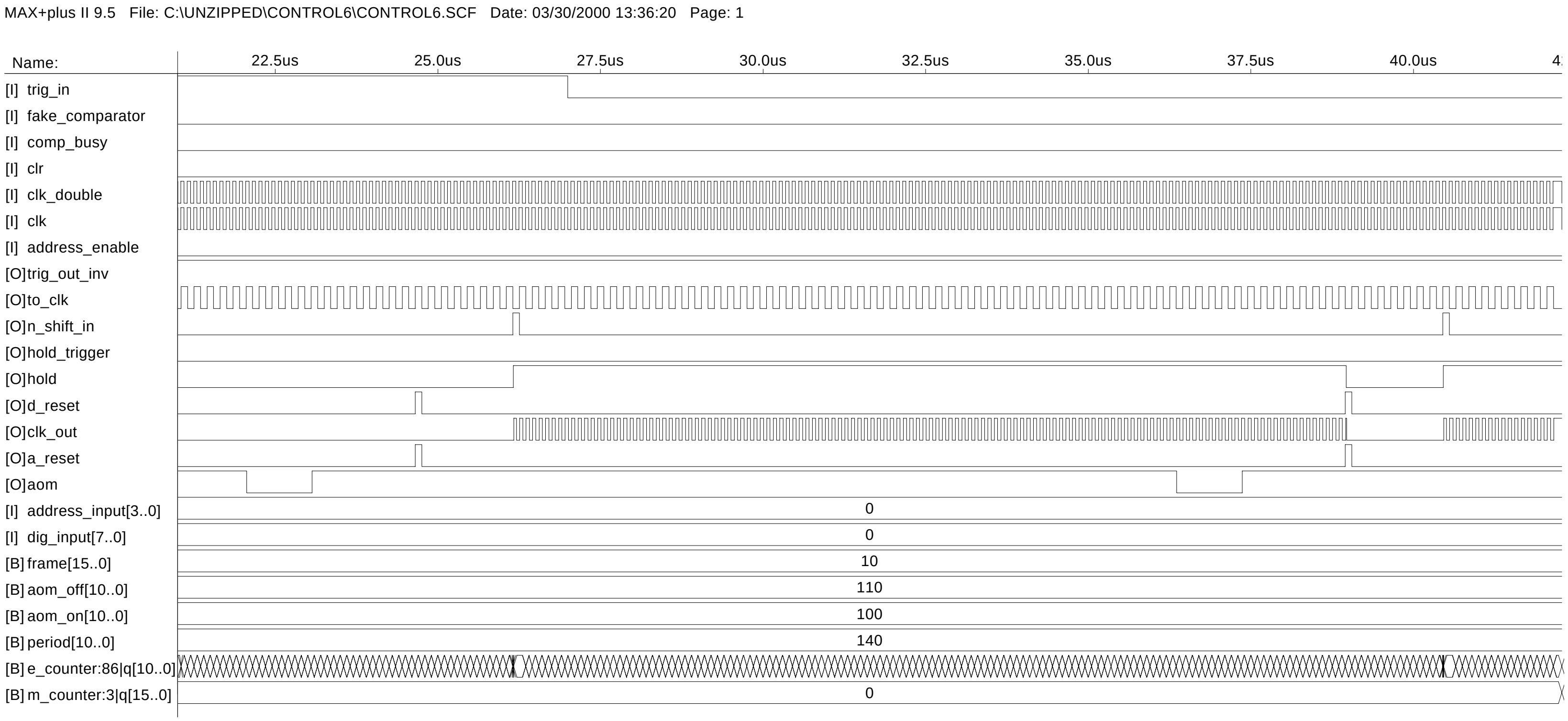

Figure B.11: This is part of the Altera simulator channel file (.scf) for the detector controller. It shows the sequence of signals that read out a single frame.

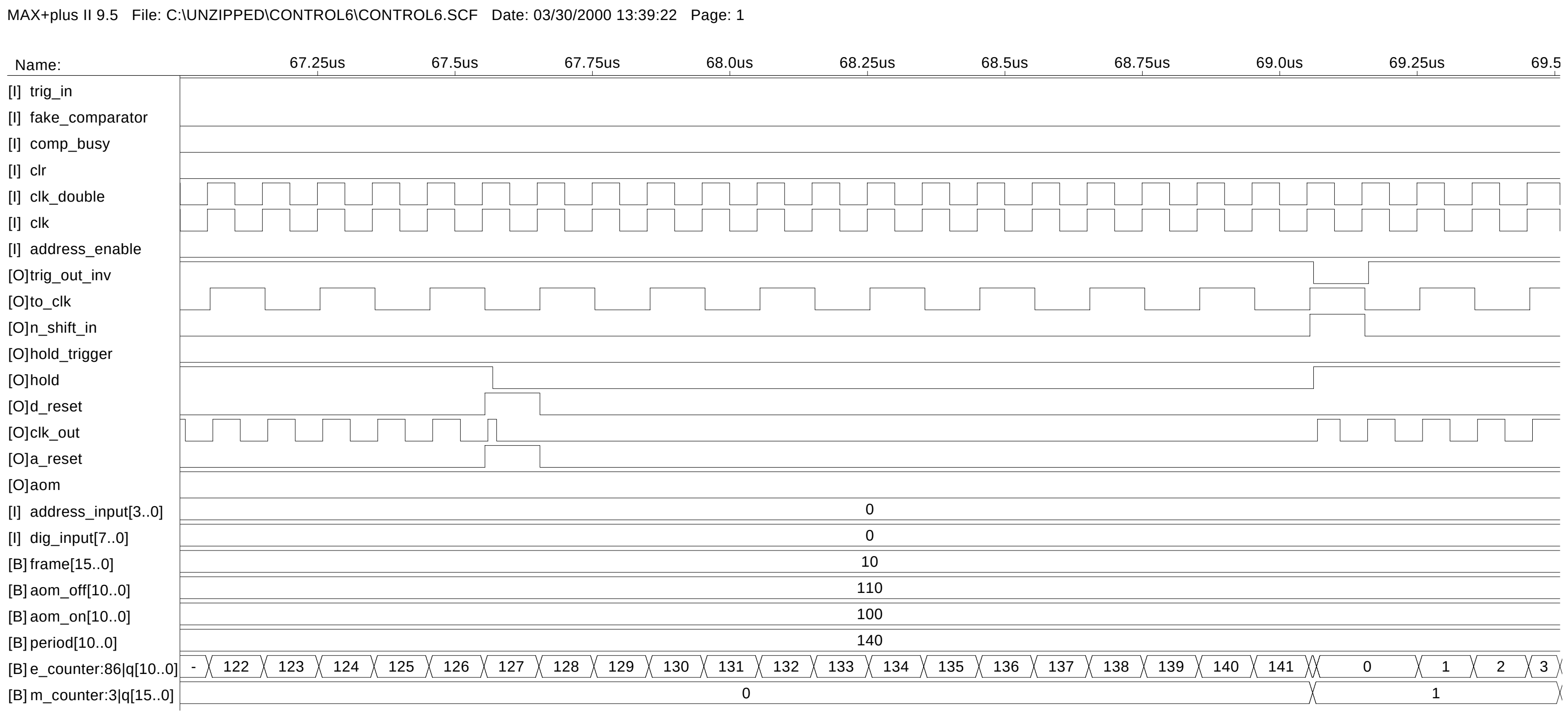

Figure B.12: This is part of the Altera simulator channel file (.scf) for the detector controller. It shows a closeup of the signals that terminate and initiate a frame readout.

Appendix C

Convergence of Moments of PDFs

A crucial consideration when presenting measurements of the moments of probability distributions is whether sufficient samples are used so that the moments are converged. This appendix describes a study I made to understand the convergence problem and to estimate the number of samples required to resolve the moments of the fluid particle acceleration distribution.

Historically one of the great challenges in turbulence measurement has been to develop techniques that allow enough samples to be taken. When measurements are made in atmospheric flows where it is possible to achieve very large Reynolds numbers, the flow conditions fluctuate in time and this places a limit on the number of samples that can be taken. In well controlled laboratory flows using hot wire anemometry, it is possible to obtain huge number of samples.

Turbulence measurement techniques relying on imaging particle positions have greater problems with convergence. For standard particle image velocimetry, two high resolution images must be acquired and processed for each velocity field measurement. Although available computational resources are able to handle 10^3 or 10^4 velocity fields, I do not know of any high Reyolds number statistical results obtained in this way. (Of course there are other limitations as well, but here we are concerned with statistical convergence.) Particle tracking measurements face an even bigger challenge. Hundreds of images of each trajectory are required in order to obtain particle positions as a function of time. Approaches such as 3D particle tracking velocimetry (Maas et al, 1993) deal with this by tracking hundreds of particles simultaneously so that it works out to order 1 trajectory per image. With our strip detector measurements we can only track a few particles at once, but because each image is only 512 strips rather than $512^2 = 262144$ pixels, we are able to obtain many more images. In 1 day of data taking we can acquire 60000 sequences of 4000 images each which when compressed is typically about 4 Gigabytes of data.

Now we consider the convergence requirements for the moments of the acceleration distribution. This requires only a straight forward statistical analysis, but the terminology can get complicated. Assume that we have measured a set of N independent samples, x_i, from a stationary probability distribution $P(x)$. We wish to estimate the moments of the distribution

$$m_n = \int_{-\infty}^{\infty} x^n P(x) dx \tag{C.1}$$

and we have been trained to expect that the statistics to use to estimate these are the moments of the measured samples

$$\tilde{m}_n = \frac{1}{N} \sum_i x_i^n . \tag{C.2}$$

Note that m_n is a number determined by the distribution $P(x)$ while $\tilde{m}_n$ is a random variable which is different for different sample sets. So in determining the error in our estimate of a moment we have to answer two questions. First, is the estimate unbiased, *i.e.* is $\langle \tilde{m} \rangle = m_n$? Second, what is the variance of the estimate around its mean value?

By commuting the average and the sum in Eq. C.2 it is simple to see that the moments are unbiased estimates. But that is not nearly the entire story on unbiasedness. For example, instead of the raw moments, consider the normalized moments.

$$\tilde{M}_n = \frac{\frac{1}{N}\sum_i x_i^n}{\left(\frac{1}{N}\sum_i x_i^2\right)^{n/2}} . \tag{C.3}$$

Now the average and the sums do not commute and it turns out that $\langle \tilde{M}_n \rangle \neq \frac{m_n}{m_2^{n/2}}$.

To gain a better understanding of this effect and to estimate the number of samples necessary to accurately estimate moments, I wrote a Monte Carlo which chooses random samples from a known distribution. I have studied both gaussian distributed samples and samples from a stretched exponential distribution,

$$P(a) = C \exp\left(\frac{-a^2}{\left(1 + |a\beta/\sigma|^\gamma\right)\sigma^2}\right) . \tag{C.4}$$

As discussed in section 4.3, a fit of this function provides an excellent parameterization of the acceleration distribution. This study was made with $C = 0.8124$, $\beta = 0.481$, $\gamma = 1.464$, $\sigma = 0.29825$. These are different from the values in section 4.3 because they were obtained from a fit to a much smaller data set. The *Numerical Recipes* (Press et al, 1992) chapter on random numbers is a very helpful introduction to generating samples from a distribution. I wrote a version of their rejection method that uses this stretched exponential distribution.

The code chooses N samples and calculates the desired statistics from them. This is then repeated many times to obtain the distribution of the measured statistics. Figure C.1 shows the distributions of measured second moments for samples from the acceleration distribution with N ranging from 100 to 50,000. Figure C.2 is similar except it shows the distributions of the measured fourth moments. The true 4th moment in this parameterization of the acceleration distribution is equal to 21.6. Both of these are unbiased estimates, but the fourth moment is unbiased in a problematic way. For small N the most probable value of the measurement is far below the mean value since there is an extremely

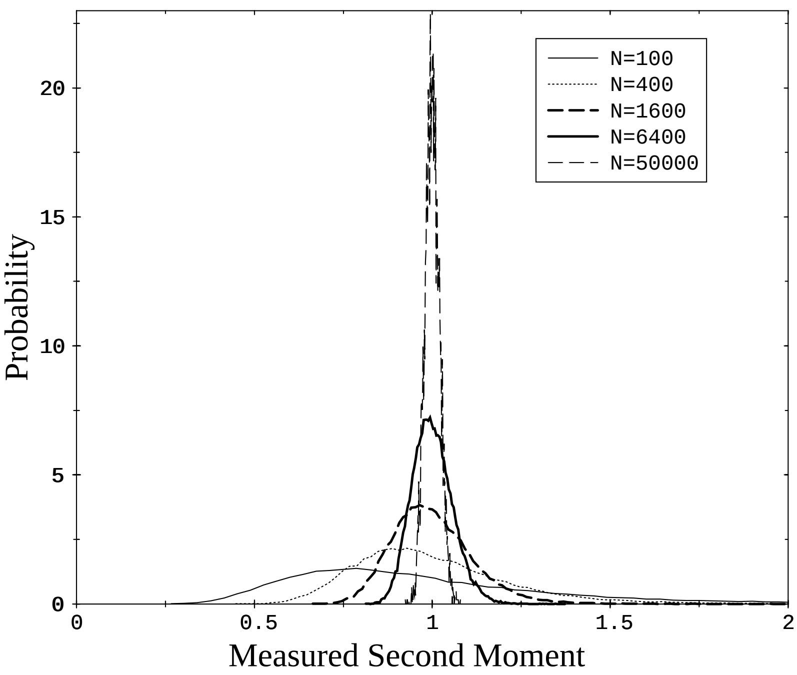

Figure C.1: Distribution of variances measured from samples from the distribution in Eq C.4.

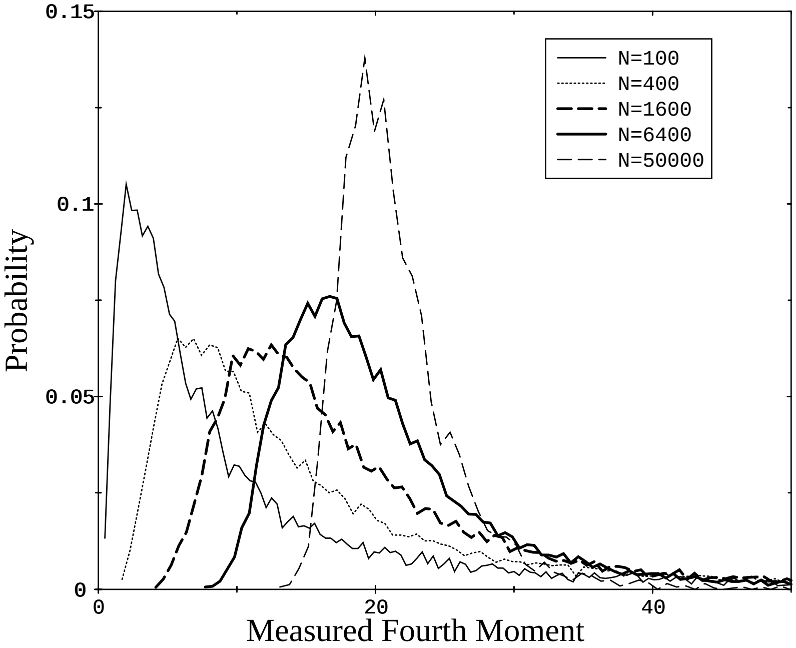

Figure C.2: Distribution of fourth moments measured from samples from the distribution in Eq C.4.

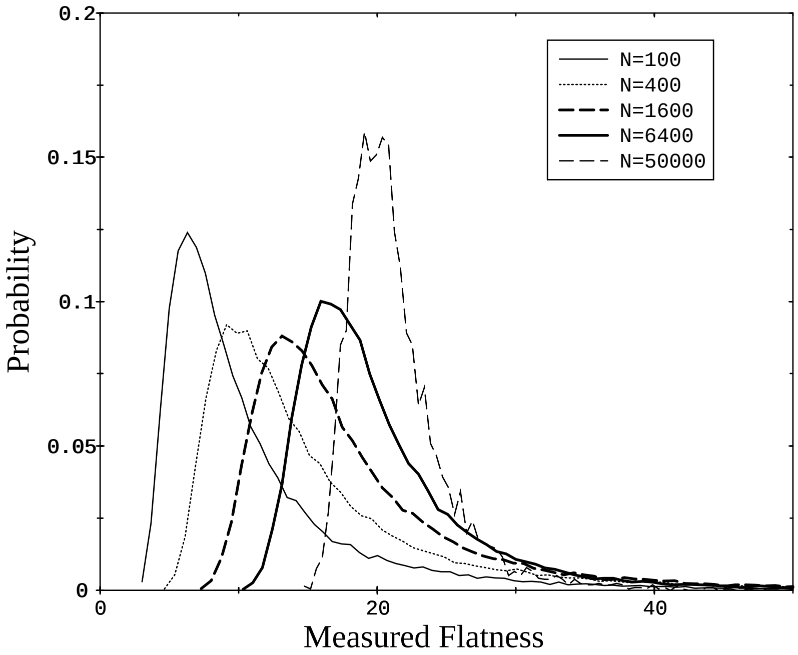

Figure C.3: Distribution of flatness factors measured from samples from the distribution in Eq C.4.

long positive tail. It is sometimes this effect that is referred to when researchers question whether the scatter between data sets is an accurate measure of the degree of statistical convergence. Measured moments can all be clustered around the wrong value if the number of samples is too small.

Figure C.3 contains the distributions of the measured flatness. It appears similar to the fourth moment, but it is not unbiased. Figure C.4 shows the mean value for each of the previous 3 figures normalized by the value obtained by integrating the pdf. The 2nd moment and the 4th moment show no bias while the flatness shows a significant bias that disappears in the limit $N \to \infty$. This bias is almost never significant, since the variance of the measurement is usually larger than the bias. However, it has been helpful for me to see it to understand the issue precisely.

The second question concerning the variance of a statistical estimate around its mean is the one that matters most in considering convergence. If the underlying distribution is a gaussian, the variance of at least the low order moments is known analytically. The second moment measured from N gaussian distributed random variables with unit variance has a χ^2_N distribution with variance $2/N$. Thus the rms error in a measurement of a second moment of this gaussian distribution is $\sqrt{2}N^{-1/2}$. The fractional rms errors for measurements of second and fourth moments of the acceleration distribution are shown in Fig C.5. They both scale as $N^{-1/2}$, but the proportionality constants are much larger than for a gaussian. The second moment scales as $4.5N^{-1/2}$ and the fourth as $48N^{-1/2}$. Thus it takes about 2000 samples to achieve a 10% measurement of the variance and 230,000 samples for the same accuracy on the fourth moment. A 1% measurement then takes 100 times this many samples.

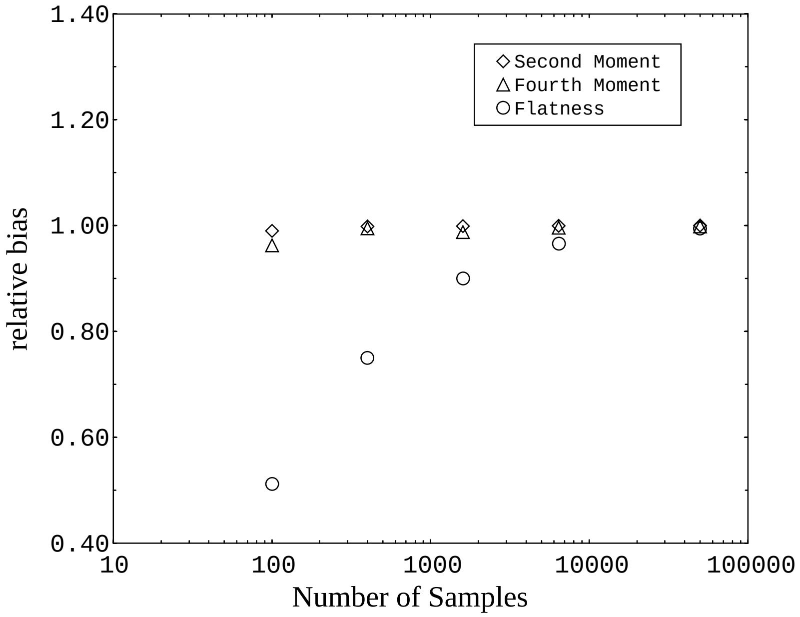

Figure C.4: Relative bias of the variance, fourth moment, and flatness estimators as a function of the number of samples used. For each sample set, the bias is the mean value of the estimator divided by the true value of the parameter it is to estimate.

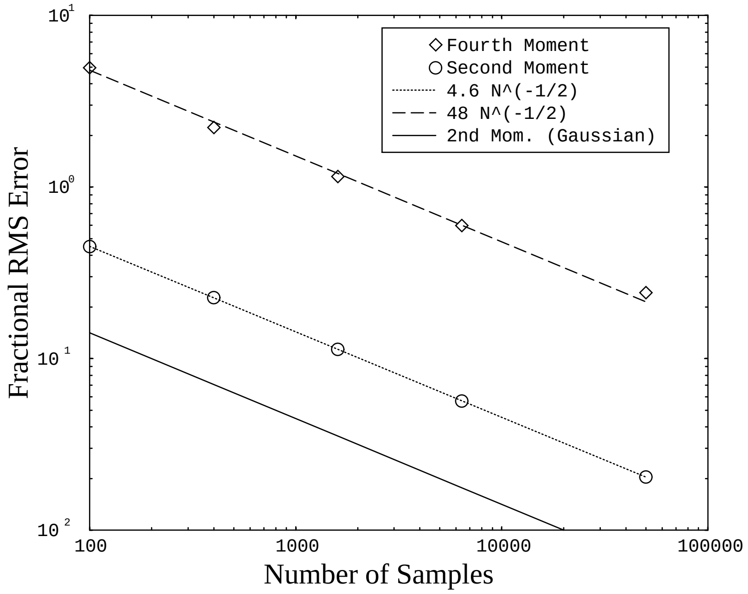

Figure C.5: Measured variance

It is not easy to directly use these numbers to estimate statistical measurement errors though. First, samples are often not independent. In our data, we sample many times along a single trajectory. This can give the appearance of convergence by making pdfs nice and smooth while still not being converged. Second, the convergence of the 4th moment in particular depends strongly on the parameters of the distribution. Some of our data sets appear to have flatnesses above 50, and this means that many more than 230,000 samples are needed for a 10% estimate. The approach we have actually used to estimate uncertainties is to divide the the data sets into subsets and estimate uncertainties from differences between the subsets. If the measurements from different subsets are gaussian distributed, the the error is the standard deviation of the measurements from subsets divided by the square root of the number of sets. We use this as the best estimate, recognizing that if the number of samples are small, then this gaussian assumption breaks down as shown in Fig. C.2.

Bibliography

Anselmet F, Gagne Y, Hopfinger EJ, Antonia RA. 1984. High-order velocity structure functions in turbulent shear flows. *J. Fluid Mech.* 140: 63–89

Arad I, Dhruva B, Kurien S, L'vov VS, et al. 1998. Extraction of anisotropic contributions in turbulent flows. *Phys. Rev. Lett.* 81(24): 5330–5333

Basset AB. 1888. On the motion of a sphere in a viscous liquid. *Phil. Trans. R. Soc. London A* 179: 43–63

Batchelor GK. 1951. Pressure fluctuations in isotropic turbulence. *Proceedings of the Cambridge Philosophical Society* 47: 359–374

Belin F, Maurer J, Tabeling P, Willaime H. 1996. Observation of intense filaments in fully developed turbulence. *J. Phys II* 6(4): 573–584

Belin F, Maurer J, Tabeling P, Willaime H. 1997. Velocity gradient distributions in fully developed turbulence: an experimental study. *Phys. Fluids* 9(12): 3843–3850

Borgas MS. 1993. The multifractal Lagrangian nature of turbulence. *Phil. Trans. R. Soc. Lond. A* 342(1665): 379–411

Boussinesq J. 1903. *Theorie Analytique de la Chaleur*. Paris: L'Ecole Polytechnique

Buchave P, George WK, Lumley JL. 1979. The measurement of turbulence with the laser-doppler anemometer. *Ann. Rev. Fluid Mech.* 11: 443–503

Cadot O, Douady S, Couder Y. 1995. Characterization of the low-pressure filaments in a three- dimensional turbulent shear flow. *J. Phys.* 7(3): 630–646

Chen S, Sreenivasan KR, Nelkin M, Cao N. 1997. Refined similarity hypothesis for transverse structure functions in fluid turbulence. *Physical Review Letters* 79(12): 2253–2256

Coimbra CFM, Rangel RH. 1998. General solution of the particle momentum equation in unsteady stokes flows. *J. Fluid Mech.* 370: 53–72

Corrsin S, Lumley J. 1956. On the equation of motion for a particle in turbulent fluid. *Appl. Sci. Res.* 6: 114–116

Douady S, Couder Y, Brachet ME. 1991. Direct observation of the intermittency of intense vorticity filaments in turbulence. *Physical Review Letters* 67(8): 983–986

Dracos T. 1996. *Three-Dimensional Velocity and Vorticity Measuring and Image Analysis Techniques*. Dordrecht, Netherlands: Kluwer

Fast J, Alam MS, Alexander J, Anastassov A, et al. 1999. Design, performance and status of the CLEO III silicon detector. *Nucl. Instrum. Methods Phys. Res. A and Methods in Physics Research* 435(1-2): 9–15

Fauve S, Laroche C, Castaing B. 1993. Pressure fluctuations in swirling turbulent flows. *J. Phys. II* 3(3): 271–278

Garg S, Warhaft Z. 1998. On the small scale structure of simple shear flow. *Phys. Fluids* 10(3): 662–673

Gotoh T, Rogallo RS. 1999. Intermittency and scaling of pressure at small scales in forced isotropic turbulence. *J. Fluid Mech.* 396: 257–285

Grant H, Steward R, Moilliet A. 1962. Turbulence spectra from a tidal channel. *J. Fluid Mech.* 12: 241–268

Hanna SR. 1981. Lagrangian and Eulerian time-scale relations in the daytime boundary layer. *J. Appl. Meteor.* 20(3): 242–249

Hill RJ, Thoroddsen ST. 1997. Experimental evaluation of acceleration correlations for locally isotropic turbulence. *Physical Review E* 55(2): 1600–1606

Hill RJ, Wilczak JM. 1995. Pressure structure functions and spectra for locally isotropic turbulence. *J. Fluid Mechanics* 296: 247–269

Holzer M, Siggia ED. 1993. Skewed, exponential pressure distributions from gaussian velocities. *Physics of Fluids* 5: 2525–2532

Jimenez J, Wray A, Saffman P, Rogallo R. 1993. The structure of intense vorticity in isotropic turbulence. *J. Fluid Mech.* 255: 65–90

Kaneda Y. 1993. Lagrangian and Eulerian time correlations in turbulence. *Phys. Fluids A* 5(11): 2835–2845

Kim I, Elghobashi S, Sirignano WA. 1998. On the equation for spherical-particle motion: effect of Reynolds and acceleration numbers. *J. Fluid Mech.* 367: 221–253

Kolmogorov AN. 1941a. Dissipation of energy in locally isotropic turbulence. *Dokl. Akad. Nauk SSSR* 31: 538–540

Kolmogorov AN. 1941b. The local structure of turbulence in incompressible viscous fluid for very large Reynolds numbers. *Dokl. Akad. Nauk SSSR* 30: 301–305

Kolmogorov AN. 1962. A refinement of previous hypotheses concerning the local structure of turbulence in a viscous incompressible fluid at high Reynolds number. *J. Fluid Mech.* 13: 82–85

Lindsey JK. 1996. *Parametric Statistical Inference*. Oxford: Clarendon Press

L'vov VS, Podivilov E, Procaccia I. 1997. Temporal multiscaling in hydrodynamic turbulence. *Phys. Rev. E* 55(6): 7030–7035

Maas HG, Gruen A, Papantoniou D. 1993. Particle tracking velocimetry in three-dimensional flows. 1. photogrammetric determination of particle coordinates. *Experiments in Fluids* 15(2): 133–146

Mann J, Ott S, Andersen JS. 1999. Experimental study of relative turbulent diffusion, RISO internal report R-1036(EN), Roskilde, Denmark

Maurer J, Tabeling P, Zocchi G. 1994. Statistics of turbulence between two counterrotating disks in low-temperature helium gas. *Europhys. Lett.* 26(1): 31–36

Maxey MR, Riley JJ. 1983. Equation of motion for a small rigid sphere in a nonuniform flow. *Phys. Fluids* 26(4): 883–889

Mei R, Lawrence CJ, Adrian RJ. 1991. Unsteady drag on a sphere at finite reynolds number with small fluctuations in the free-stream velocity. *J. Fluid Mech.* 233: 613–631

Meneveau C, Sreenivasan KR. 1987. Simple multifractal cascade model for fully developed turbulence. *Phys. Rev. Lett.* 59(13): 1424–1427

Meneveau C, Sreenivasan KR. 1991. The multifractal nature of turbulent energy dissipation. *J. Fluid Mech.* 224: 429–484

Monin AS, Yaglom AM. 1975. *Statistical Fluid Mechanics*, vol. 2 (Ed. J. L. Lumley). Cambridge, Mass.: MIT Press

Mydlarski L, Warhaft Z. 1996. On the onset of high-Reynolds-number grid-generated wind tunnel turbulence. *J. Fluid Mech.* 320: 331–368

Nelkin M. 1990. Multifractal scaling of velocity derivatives in turbulence. *Physical Review A* 42(12): 7226–7229

Nelkin M. 1994. Universality and scaling in fully developed turbulence. *Advances in Physics* 43(2): 143–181

Nelkin M. 2000. Resource letter TF-1: Turbulence in fluids. *Am. J. Phys.* 68(4): 310–318

Nelkin M, Chen S. 1999. Intermittency corrections to the mean square particle acceleration in high Reynolds number turbulence, submitted to Physics of Fluids

Noullez A, G. W, W. L, Miles RB, et al. 1997. Transverse velocity increments in turbulent flow using the RELIEF technique. *J. Fluid Mech.* 339: 287–304

Obukhov AM. 1949. Pressure fluctuations in a turbulent flow. *Dokl. Akad. Nauk. SSSR* 66: 17–20

Obukhov AM, Yaglom AM. 1951. The microstructure of turbulent flow. *Frikl. Mat. Mekh.* 15(3), translated in National Advisory Committee for Aeronautics (NACA), TM 1350, Washington, DC (1953)

Oseen CW. 1927. *Hydrodynamik*. Leipzig: Akademische Verlagsgesellschaft

Pope SB. 1985. PDF methods for turbulent reactive flows. *Prog. Energy Combust. Sci* 11: 119–192

Pope SB. 1994. Lagrangian PDF methods for turbulent flows. *Annu. Rev. Fluid Mech.* 26: 23–63

Pope SB. 1997. Private communication

Pope SB. 1999. Private communication

Press W, Teukolsky S, Vetterling W, Flannery B. 1992. *Numerical Recipes in C*. Cambridge: Cambridge University Press

Richardson LF. 1922. *Weather Prediction by Numerical Process*. England: Cambridge University Press

Richardson LF. 1926. Atmospheric diffusion shown on a distance-neighbour graph. *Proc. R. Soc. London Ser. A* 110: 709–737

Robert C. Weast E. 1997. *Handbook of Chemistry and Physics*, vol. 55. Clevland: CRC Press

Sato Y, Yamamoto K. 1987. Lagrangian measurement of fluid-particle motion in an isotropic turbulent field. *J. Fluid Mech.* 175: 183–199

Sawford BL. 1991. Reynolds number effects in Lagrangian stochastic models of turbulent dispersion. *Phys. Fluids A* 3: 1577–1586

Shen X, Warhaft Z. 2000. The anisotropy of the small scale structure in high Reynolds number ($R_\lambda = 1000$) turbulent shear flow, submitted to Physics of Fluids

Shlien DJ, Corrsin S. 1974. A measurement of Lagrangian velocity autocorrelation in approximately isotropic turbulence. *J. Fluid Mech.* 62: 255–271

Snyder WH, Lumley JL. 1971. Some measurements of particle velocity autocorrelation functions in a turbulent flow. *J. Fluid Mech.* 48: 41–71

Squires KD, Eaton JK. 1991. Lagrangian and Eulerian statistics obtained from direct numerical simulations of homogeneous turbulence. *Phys. Fluids A* 3(1): 130–143

Sreenivasan KR. 1991. On local isotropy of passive scalars in turbulent shear flows. *Proceedings of the Royal Society of London* 434(1890): 165–182 + 1

Sreenivasan KR. 1995. On the universality of the Kolmogorov constant. *Phys. Fluids* 7(11): 2778–2784

Sreenivasan KR. 1999. Fluid turbulence. *Reviews of Modern Physics* 71(2): S383–395

Sreenivasan KR, Antonia RA. 1997. The phenomenology of small-scale turbulence. *Annu. Rev. Fluid Mech.* 29: 435–472

Sreenivasan KR, Dhruva B. 1998. Is there scaling in high-Reynolds-number turbulence? *Prog. Theor. Phys. Suppl.* (130): 103–120

Sreenivasan KR, Kailasnath P. 1993. An update on the intermittency exponent in turbulence. *Phys. Fluids A* 5(2): 512–514

Stolovitzky G, Kailasnath P, Sreenivasan KR. 1995. Refined similarity hypotheses for passive scalars mixed by turbulence. *J. Fluid Mech.* 297: 275–291

Taylor GI. 1921. Diffusion by continuous movements. *Proc. Lond. Math Soc.* 20: 196–212

Taylor JR. 1997. *An Introduction to Error Analysis*. Sausalito, CA: University Science Books, 2nd ed.

Tchen CM. 1947. Mean value and correlation problems connected with the motion of small particles suspended in a turbulent fluid, Ph.D. Thesis, Delft University

Tennekes H. 1975. Eulerian and Lagrangian time microscales in isotropic turbulence. *J. Fluid Mech.* 67: 561–567

Van Atta CW, Antonia RA. 1980. Reynolds number dependence of skewness and flatness factors of turbulent velocity derivatives. *Phys. Fluids* 32(2): 252–257

Vedula P, Yeung PK. 1999. Similarity scaling of acceleration and pressure statistics in numerical simulations of isotropic turbulence. *Physics of Fluids* 11(5): 1208–1220

Virant M, Dracos T. 1997. 3D PTV and its applications on Lagrangian motion. *Meas. Sci. Technol.* 8: 1539–1552

Voth GA, Satyanarayan K, Bodenschatz E. 1998. Lagrangian acceleration measurements at large Reynolds numbers. *Phys. Fluids* 10(9): 2268–2280

Wand MP, Jones MC. 1995. *Kernel Smoothing*. London: Chapman and Hall

Warhaft Z. 2000. Passive scalars in turbulent flows. *Annu. Rev. Fluid Mech.* 32: 203–240

Weil JC, Sykes RI, Venkatram A. 1992. Evaluating air-quality models: review and outlook. *J. Appl. Meteor.* 31(10): 1121–1145

Yeung PK. 1994. Direct numerical simulation of two-particle relative diffusion in isotropic turbulence. *Phys. Fluids* 6(10): 3416–3428

Yeung PK. 1997. One- and two-particle Lagrangian acceleration correlations in numerically simulated homogeneous turbulence. *Phys. Fluids* 9(10): 2981–2990

Yeung PK. 2000. Private communication

Yeung PK, Pope SB. 1989. Lagrangian statistics from direct numerical simulations of isotropic turbulence. *J. Fluid Mech.* 207: 531–586